UNIVERSITÀ DEGLI STUDI DI UDINE
Dipartimento Politecnico di Ingegneria e Architettura

PHD THESIS

Advanced Control for Interior Permanent Magnet Synchronous Motor (IPMSM) and Synchronous Reluctance Motor (SynRM)

PhD Candidate:
Amir SHAHDADI

Supervisor:
Roberto PETRELLA

Co-supervisor:
Sandro CALLIGARO

PHD CYCLE XXXV
2022

This thesis is dedicated to my mother, Mah Sotoon Shahdadi

Abstract

Synchronous motors are now widely used in various applications, such as household appliances and automotive applications, as the technology to control these kinds of machines has become more affordable. The controlling of these motor play important role to improve the performance of them. Thus, it is important to research effective control methods, particularly for automotive applications where the improvement of the range of electric vehicles is a current issue for all automotive producers. There are different magnetic structures of synchronous machines, but the Internal Permanent Magnet Synchronous Machines (IPMSMs) and Synchronous Reluctance Machines (SynRMs) are the two most popular kinds. In Synchronous Reluctance Machines since torque is only produced by the variable reluctance, while Internal Permanent Magnet Synchronous Machines typically have higher torque density, since they produce torque with contributions from both the permanent magnets (electrodynamical principle) and variable reluctance. According to the application, the motors can be selected based on the topology. The behavior of flux linkages for both of these machines is substantially nonlinear due to their magnetic structure, which means that the value of the parameters depends on the operating point. It is usual practice to use Maximum Torque per Ampere (MTPA) to optimize the copper losses, i.e. the stator Joule-effect losses. By applying MTPA, based on the motor parameters, the correct angle that ensures the maximum torque output is chosen for a specific magnitude of current vector. The correct angle must be determined and adjusted according to the desired torque and in different operating speed ranges, i.e., below and above base speed. Real Signal Injection (RSI) and Virtual Signal Injection (VSI) are two MTPA tracking methods that are examined and assessed on IPMSM and SynRM in the first part of the thesis. In order to balance the dynamics of the tracking loop as a function of the torque operating point, a gain compensation is used for the Virtual Signal Injection. The two algorithms are applied to the controller of IPMSM. An analytical model is used instead of non-linear model of a Synchronous Reluctance Machine (SynRM) in order to assess accuracy and performance. By doing this, potential measuring mistakes in the real machine flux maps can be eliminated. It is suggested a novel method to correct steady-state MTPA tracking errors by non-linear flux maps, enhancing the VSI's accuracy even when the machine flux maps are known with only raw quantization. The proposed contributions are validated after implementing the algorithm in a microcontroller and their performances are assessed on an IPMSM and SynRM motor drive.
Furthermore, the operation of IPMSM machine is studied in wide range speed. In this case there are MTPA, flux-weakening and MTPV regions. The obtained equation to control the torque is a quartic equation that make it difficult to find the roots. However, the analytical solutions that are used for minimizing stator current are complex and the computation time is higher than other methods, but they are more accurate. In this thesis, a novel analytical solution is presented based on Minimum Vector solution (MVS) to obtain the $d-$ and $q-$ reference currents to minimize the stator current. The proposed method is uncomplicated to implement in a microcontroller. In addition, its implementation requires a lower number of

cubic root calculations with respect to other analytical solutions, which results in a shorter computation time. In the MTPA region and the flux-weakening region, the approach is used on an IPMSM. Also, Maximum Torque per Voltage (MTPV) region is applied to the controller and tested in high range of speed. The proposed approach, however, is focused in the MTPA and the flux-weakening region. The results are investigated in the thesis by simulation and experimentally. As the results, the computation time is decreased in comparison with other analytical models and the operating trajectory is tracked by proposed method accurately.

In order to obtain optimal performance and efficiency, the knowledge of non-linear flux vs. current behavior (typically represented in the form of maps) is required both off-line (i.e. during the control parameters design) and online (during control operation). Different methods have been proposed for this purpose, such as the use of Look-Up Tables (LUT), which main drawback is the memory usage. To solve this problem, approximation approaches (e.g. using polynomial functions) have been introduced, which typically suffer from lower accuracy. In this Thesis, the Group Method of Data Handling (GMDH) is used to as a novel approach to find an optimal approximation of the flux linkage maps of IPMSM. Due to the multi-layer structure of this method and the coefficient selection process, the accuracy of the approximated flux functions is significantly improved with respect to the previous approaches. Moreover, this method can be used online, with relatively small memory footprint and computational cost.

To enhance the performance of the drive system of the motor, the other parts such as inverter controller plays an important role. Non-linearity effects in voltage source inverters are mainly due to presence/need of dead times, voltage drops and parasitic/intrinsic capacitive effects of power devices and electric machine. Accurate compensation of these effects is of paramount importance in many drives applications, as resulting output voltage distortion has strong effects on the performance of current control loop, especially at low speed, where the operating voltage of the machine is comparable to the level of distortion introduced by the non-linearity components. In this thesis, some studies and a novel approach about the dead-time compensation for the inverter are presented. In this thesis, the advanced control of Interior Permanent Magnet Synchronous Motor and Synchronous Reluctance Motor is studied.

The thesis is started by an introduction in Chapter. 1. In this chapter a literature review is presented for IPM and SynR machines, their main features, advantages, main applications. The magnetic structure of IPM and SynR motors are examined in Chapter. 2. Based on advantages and disadvantages of these motors they have been compared. Following this evaluation of the PMSM analytical model, mechanical and electrical equations are obtained. Furthermore,the behaviour of the motor in MTPA and flux-weakening regions is presented in this chapter.

The maximum torque per ampere control has been examined in Chapter. 3 for IPMSM and SynRM. The functioning, advantages, and disadvantages of the Real Signal Injection and Virtual Signal Injection algorithms were comprehensively reviewed. The stability anal-

ysis of MTPA tracking algorithms has been studied and a gain adaption strategy for both techniques has been proposed. A novel method is suggested to correct steady-state MTPA tracking errors by non-linear flux maps, enhancing the VSI's accuracy even when the machine flux maps are known with only raw quantization.
In Chapter. 4, a new analytical solution is studied to control the torque in IPMSM for MTPA and flux-weakening region. The proposed method is uncomplicated to implement in a microcontroller. In addition, its implementation requires a lower number of cubic root calculations with respect to other analytical solutions, which results in a shorter computation time.
In Chapter. 5, GMDH method is presented as a novel approach to approximate the flux-linkages maps of an IPMSM. The method is compared with a polynomial method. The results show that the accuracy of GMDH is higher than polynomial method, according to the error percentage.
In Chapter. 6, a recent approach for dead-time compensation adopting an analytical model of the physical behavior of the inverter non-linearities has been considered. Model parameters are derived from a self commissioning procedure, based on proper voltage injection and processing, both affecting the accuracy of achievable compensation. One of the crucial aspects of this approach is the autonomous selection of the threshold current of the measured voltage to current characteristics, a value whose reliable knowledge is mandatory for the accurate identification of the non-linearity model. The simulation and experimental results are presented to investigate the contribution of the novel approach to the motor controller.

Keywords: AC Machines, Interior Permanent Magnet Synchronous Motor (IPMSM), Synchronous Reluctance Motor (SynRM), Maximum Torque Per Ampere (MTPA), Flux-weakening, Maximum Torque Pwe Voltage (MTPV), Real Signal Injection (RSI), Virtual Signal Injection (VSI).

Contents

List of Figures

List of Tables

Nomenclature

β Angle of stator current and $q-$axis current [rad]

β_{MTPA} β value in MTPA trajectory [rad]

δ_x Duty cycle of phase x (A or B or C) [s]

δ_γ High sinusoidal frequency signal

ϵ_f Low pass filter output

γ_{MTPA} Current vector angle in MTPA point [red]

$\Lambda_a, \Lambda_b, \Lambda_c$ Permanent magnet contribution three phase [Wb]

$\lambda_a, \lambda_b, \lambda_c$ Flux-linkages of three phase [Wb]

λ_d, λ_q $d-$ and $q-$ axis flux-linkages [Wb]

Λ_{mg} Permanent magnet contribution [A]

ω_e Electrical angular speed [rad/s]

ω_r Mechanical angular speed [rpm]

$\Omega_{loop}(s)$ Closed-loop speed response transfer function

A Amplitude of injection signal

B_m Coefficient of friction

BW_{MTPA} Band-with of Speed controller

$C(s)$ Speed controller

C_{out} Inverter phase output capacitance [F]

f_i Frequency of δ_γ [Hz]

i_a, i_b, i_c Currents of three phase [A]

i_d, i_q $d-$ and $q-$ axis currents [A]

i_d^h, i_q^h $d-$ and $q-$ axis currents with high frequency term [A]

I_s The amplitude of stator current [A]

I_x Phase current [A]

$i_{d_{FW}}, i_{q_{FW}}$ $d-$ and $q-$ axis currents of flux-weakening region [A]

$i_{d_{MTPA}}, i_{q_{MTPA}}$ $d-$ and $q-$ axis currents of MTPA trajectory [A]

$i_{d_{ref}}, i_{q_{ref}}$ refrerence $d-$ and $q-$ axis currents [A]

I_{max} Maximum amplitude of stator current [A]

I_{thr} "low" to "high" current threshold [A]

L_d, L_q Inductances of the machine in $d-$ and $q-$ axis [H]

L_m Anisotropy component's amplitude [H]

L_{aa}, L_{bb}, L_{cc} Self inductances [H]

L_{ab}, L_{bc}, L_{ac} Mutual inductances [H]

L_{ms0} Magnetization inductance's constant [H]

M_s Mutual induction coefficient among the stator winding's phases [H]

$P(s)$ Mechanical load plant transfer function

P_m Output electromechanical powr [W]

p_p polr pairs

P_{cu} Joule losses in stator windings [W]

PF Power factor

R_s Stator Resistance [Ohm]

T_e Electromagnetic torque [Nm]

T_e^h Perturbed torque by high frequency signal [Nm]

T_L Load torque [Nm]

$T_{delay,\ H\rightarrow L}$ Turn-off switching delay [s]

$T_{delay,\ L\rightarrow H}$ Turn-on switching delay [s]

T_{DT} Dead-time duration [s]

T_{ref} Reference torque [Nm]

T_{SW} Switching period [s]

u_a, u_b, u_c Voltages of three phase [V]

U_s Stator voltage [V]

V_{diode} Diode conduction voltage drop [V]

V_{IGBT} IGBT conduction voltage drop [V]

V_{SW} Average switch voltage drop [V]

$V_{x0_{cap}}$ Inverter leg distortion voltage, capacitive effect [V]

V_{x0} Inverter leg voltage (referred to inverter negative terminal) [V]

$V_{xn_{DT}}$ Motor phase distortion voltage [V]

V_{xn} Motor phase voltage [V]

$V_{x0_{DT}}$ inverter leg distortion voltage [V]

Acronyms

BPF Band Pass Filter

CPSR Constant Power Speed Range

DFVC Direct Flux Vector Control

DTC Direct Torque Control

EMF Electro Motive Force

ESC Extremum Seeking Control

FOC Field Oriented Control

FW Flux-Weakening

GMDH Group Method of Data Handling

HPF High Pass Filter

IM Induction Machine

IPMSM Interior Permanent Magnet Synchronous Machine

LPF Low Pass Filter

LUT Look Up Table

MMF Magneto Motive Force

MTPA Maximum Torque Per Ampere

MTPV Maximum Torque Per Voltage

PI Proportional Integral

PM-SynRM Permanent Magnet Assisted Synchronous Reluctance Machine

PMSM Permanent Magnet Synchronous Machine

RI-PMSM Radially Internal Permanent Magnet Synchronous Machine

RSI Real Signal Injection

SPMSM Surface Permanent Magnet Synchronous Machine

SynRM Synchronous Reluctance Machine

VA Voltage-Ampere

VI-PMSM V-Shaped Internal Permanent Magnet Synchronous Machine

VSI Virtual Signal Injection

Chapter 1

Introduction

It is well know that industrial development has played and still has an important role on climate change and global warming. At the same time, strong demand of resources leads the industry to manufacture more effective systems and devices. The importance of electrical motors in global industrial and civil applications can be understood considering that they represent the single largest end-use of electrical energy, accounting for more than 40% of the global electricity consumption, which corresponds to about 6000 metric tons of CO2 emissions and roughly 500-600 billion USD per year of end-user expense [1].

For these reasons, companies and institutions continue to put considerable effort in the research and development on electrical machines and drive systems, with the aim of reducing energy consumption and improving performance, both at the system- and at the component-level.

In the last decades, the improvements of electrical machines and drives, in terms of efficiency, cost reduction and performance, have been remarkable, thanks to the constant investment by industry and academia. Starting from the 1980s, the availability of strong magnet materials and low-cost electronic controllers led to the development of Permanent Magnet Synchronous Machine (PMSM), soon followed by SynRM and Permanent Magnet Assisted Synchronous Reluctance Machine (PM-SynRM). However, until the last decade, these types of machines, which exhibit high efficiency, wide speed range of operation and high power density [2], have only been adopted in applications requiring high accuracy or fast dynamics (and in few other market niches), due to their relatively high cost and the need for a properly controlled power supply. Recently, their use has spread to other applications, such as general-purpose drives, consumer goods, energy generation and traction, [3, 4]. In fact, their diffusion has been favored by a combination of factors, such as the rise of environmental consciousness, increased energy cost and energy-efficiency regulations, together with the decreasing cost of electronics.

Fig. 1.1 shows a possible taxonomy of synchronous motors. The most common machine in industry is the three-phase Induction Machine (IM), thanks to its low cost, robust construction and the possibility to be powered directly from the grid. The main disadvantage

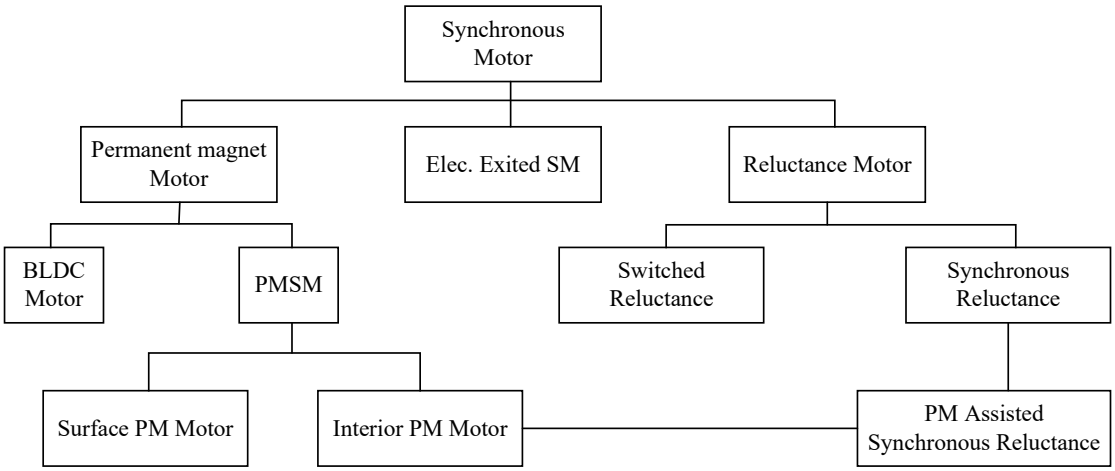

Figure 1.1: Taxonomy of Synchronous motors.

of this kind of motor is the generally low efficiency, which also leads to low power density. In particular, the induction operating principle of this machine ("asynchronous" operation) requires considerable current to flow in the rotor, which involves additional power losses and heating [5]. Besides efficiency and compactness, IMs also suffer from some specific reliability issues (e.g., in rotor bars [6] and bearings [7]), which are mainly due to the high rotor temperature. In fact, it should be noted that heat generated in the rotor is problematic, since it is more difficult to provide good dissipation (for keeping the temperature low) and temperature measurement (for protection) on the rotor, than on the stator.

Table 1.1: IM, PMSM and SynRM comparison.

Motor Type	Advantages	Disadvantages
IM	Low cost, line-start capability	low power factor, bearing faults
PMSM	high torque density, high performance in wide speed range	high cost
SynRM	high speed capability, reliable due to the rotor structure, high dynamic	high torque ripple, low power factor

1.1 IPMSM and SynRm Advantages and Disadvantages

As already mentioned, nowadays the PMSM are being increasingly adopted in many applications. The field in which these machines are having the major success is Electric and Hybrid Vehicles, both light ones (e-bikes, scooters and similar) and cars. The design of permanent magnet machines is heavily affected by the seletion of rare-earth materials, which also has important implications on the cost and sustainability of the production process.

Neodymium-iron-boron (Nd-Fe-B) and samarium-cobalt (Sm-Co) are two common materials for permanent magnets, in combination with small amounts of some relatively rare materials, such as dysprosium. Unfortunately, the price of these materials is relatively high and very volatile, heavily impacting the cost of the whole machine [8]. Also, permanent magnets are prone to demagnetization and degradation, depending on operating temperature, over-current events, moisture level and chemicals to which the machine may be exposed. Careful design and proper manufacturing process can decrease the likelihood of such negative events. In general, while PMSM's operation is based on the electro-dynamical principle of electro-mechanical conversion, the reluctance principle can also be integrated, leading to the so-called IPMSM. This motor variant normally employs a reduced amount of permanent magnet materials and also achieves higher power density and can operate in a wide speed range.
SynRM's rotor design distinguishes it from PMSMs, since it does not comprise any windings nor permanent magnets. In this case, the machine does not have the dissipation issues of IM and high cost of PMSM, and this typically results in an affordable and reliable alternative, which is the reason why SynRMs are seen as the future replacement of IMs. However, these machines operate at a lower power factor, which in turns leads to the need for a slightly over-sized power supply (i.e. a larger current rating of the driving inverter). In Table. 1.1 a summary comparison is presented based on advantages and disadvantages of the IM, PMSM and SynRM.

1.2 Maximum Torque per Ampere (MTPA) Algorithms

Based on the working principle and model of AC machines, there are infinite operating points that result in the same value of produced torque. In other words, in the control of such motors, there is a "degree of freedom", i.e. a variable whose value can be set almost arbitrarily, even if aiming at the same mechanical output (torque and speed). This clearly calls for a method for selecting the "optimal" operating point (typically in the form of a two-element current vector), given a certain optimality criterion. In PMSMs and SynRMs stator conduction losses (also referred to as "Joule" or "copper" losses) are dominant, at least in the low-speed range. For this reason, the most common optimization criterion adopted in the selection of the operating point is the minimization of current amplitude for a given torque, which can be expressed, equivalently, as maximization of torque for a given current magnitude. In both literature and industry, this condition is typically named Maximum Torque Per Ampere (MTPA). The MTPA trajectory (or "current locus") can be evaluated (theoretically or experimentally) considering a constant load condition and finding the current vector that features the minimum magnitude [9]. Based on the standard (constant-parameters) model of the machine, the analytical solution to this problem is relatively simple, although this strongly depends on the input and output variables selected. As an example, determining

the current values based on the desired torque (which is the ideal input-output selection from the control perspective) according to the MTPA condition, is relatively complex, since it involves solving a quartic equation. Moreover, since the behavior of the motor, in terms of magnetic characteristics (i.e. flux-linkage vs. current) is typically non-linear (due to magnetic saturation) and considering that the permanent magnet behavior is affected by temperature [10], the analytical solution becomes insufficient in many cases, making the implementation of SynRM challenging. As an example, in [11] and [12], the parameters of the motor are initially considered constant but, due to magnetic saturation, the theoretical MTPA algorithm is inaccurate. Magnetic non-linearity has been taken into account in [9], [13] and [14].

It is possible to accomplish the MTPA procedure with the help of Look Up Table (LUT)[15],[16]. It is also possible to get LUT data by conducting a series of laboratory experiments, although this takes more time and resources and may not adequately account for the fluctuation related to magnetic structure, components, and temperature, especially if only a few samples are tested. The LUT information can be obtained via the parameters identification methods. Such techniques still suffer from inaccuracy issues and, if implemented online, affect the overall control stability and performance. Due to these problems, LUT-based methods for MTPA operations have significant limitations [17]. In [18], a search strategy is used, in order to modify the operating point (in terms of current) so that, at steady-state, it fulfills the MTPA requirement at the required load torque. Although these solutions do not require prior knowledge of motor parameters, the slow convergence ratio of the tracking techniques results in low dynamic performance [19].

Recent years have seen the introduction of the new approaches for estimating the MTPA with the injection of specific signals. The main idea behind these techniques is based on Extremum Seeking Control (ESC) [20], i.e. the operating point is varied around its steady-state value, for the purpose of testing whether the variable of interest (torque or current, in this case) increases, decreases or remains constant, i.e. searching for a minimum or maximum. In the case of the so-called "MTPA tracking", signal injection consists in varying the current phase angle, while either the current magnitude or the torque variations is observed. Given the difficulty in directly detecting the generated torque and its variations, the MTPA tracking error can be extracted from speed oscillations, [21]. However, relatively high- performance speed sensing is required, which limits the applicability of this approach. An alternative approach has been proposed, which detects active power oscillations, based on voltage and current signals, [22] [23]. In [24], the proposed MTPA tracking algorithm based on "low-frequency" signal injection, is thoroughly analysed and experimentally validated. In this case, the current magnitude is observed, while it is assumed that the speed regulator keeps the produced torque equal to the load, despite the current angle variation injected. Both the convergence and the stability of this method were studied in [25]. A flux amplitude signal is injected, instead, in [26], in order to calculate the torque variation while observing the resulting variation of current magnitude. Whenever signals are injected (Real Signal Injection, RSI [18],[23],[22],[25],[27]) for the only purpose of MTPA tracking,

additional power losses are introduced and speed ripple or vibration are also caused. Possible mechanical resonance can be avoided by carefully choosing the injection frequency. However, since the estimation relies on terminal current and voltage measurements, harmonics in those variables could affect the signal processing.
In order to avoid these issues, Virtual Signal Injection (VSI), [28], [29], [30] has been introduced, which applies a parameter-estimation technique in order to obtain a MTPA correction signal which is supposed to be similar to the one used in RSI. Although the two classes of methods have been studied quite extensively in literature, a fair evaluation in terms of accuracy and performance of RSI and VSI was still missing. The present work comprises a direct comparison between them (Chapter. 3). As mentioned above, in the case of RSI, the actual response of the machine to the injected perturbation is considered in terms of measured torque or speed oscillations, and adopted to drive the estimates (e.g. the current space vector angle) towards the actual MTPA condition. On the other hand, VSI allows to find out the MTPA condition of the analytical model of the machine, i.e. to solve an on-line analytical optimization problem. In fact, the system response to the injected signal is obtained based on the model and some of the parameters needed for its calculation are estimated based on the actual fundamental voltage and current measurements. Therefore, in VSI is not really estimating the MTPA condition of the actual machine, but can be considered as a strategy to enhance the simplest MTPA methods with information retrieved online. The accuracy of this approach is therefore limited by the knowledge of some machine parameters (especially when saturation and/or cross-saturation are considered) and on the approximations that need to be introduced.
In the Chapter. 3, the analysis of both the classes is reported, also considering specific aspects and the influence of simplifying hypothesis that are normally introduced to allow an effective implementation. The results related to the analytical description of the tracking errors in the VSI case have been extended with respect to previous literature, also introducing a strategy for compensating the steady-state errors arising from non-linear flux maps. An effective analytical model of the machine inductance is embedded in the analysis of the tracking loop, allowing to improve tracking accuracy even in the case the machine flux maps are known with relatively low resolution. Furthermore, to improve the accuracy of the MTPA trajectory using both VSI and RSI, a LUT of $d-$ axis apparent inductance is used and the results are compared with conventional RSI and VSI.

1.3 Flux-Weakening and Maximum Torque Per Voltage

When operating a PMSM or SynRM at relatively high speed, e.g. in the MTPA condition, a given torque corresponds to a certain flux-linkage amplitude and thus the steady-state voltage magnitude is approximately proportional to speed. Thus, above a certain speed (i.e. the "base speed"), the available phase voltage (which depends on the DC-bus voltage value) will not be sufficient for keeping the current under control. To overcome this issue, other

operation regions are introduced, namely Flux-weakening (FW) and Maximum Torque Per Voltage (MTPV) regions, in which flux-linkage magnitude is reduced, with respect to its normal value.
In the FW region, the operating point current values should be chosen so that the desired torque is produced and the voltage constraint is satisfied. If the current amplitude required for both conditions to be fulfilled is above its limit (e.g. above the rated value), the current magnitude must be fixed at the limit, while torque will be lower than the desired value. Considering the mechanical characteristic of the drive (i.e. the available torque vs. speed curve), these constraints result in the available torque being constant up to the base speed. The range above that value is known as the "constant-power range", since the electrical apparent power (voltage-current product) remains constant, while torque is almost inversely proportional to speed. On other hand, at very-high-speed, it may be necessary to apply the MTPV strategy, in which the current limit is properly reduced, in order to obtain the maximum available torque for a given speed and available voltage.

Similar to the case of MTPA, obtaining FW control is challenging, due to the non-linear relationship between current and voltage magnitude, which is further complicated by the non-linear flux characteristics of IPMSMs and SynRMs. Since achieving correct FW and MTPV is required for obtaining a wide operating range, considerable research effort has been dedicated to the development of effective control methods applicable in these regions. In the first experiments [31] and [32], the torque capacity of IPMSMs in FW operation was the primary focus. The control scheme based on LUT and approaches using models were also given [33],[34],[35],[36],[9],[12],[37],[38]. Although these methods are indeed effective, the overall performance of the drive may suffer significantly, if parameters are altered or any errors are made [39].
In order to solve these issues, several closed-loop techniques have been proposed, aiming at a robust FW control, ideally parameter-independent or "parameter-free". Even in this case, the ideal current references may be calculated and used as a feed-forward term, improving the control performance during transients.

As previously discussed, to overcome the non-linearity, inductance variation can be taken into account via LUTs. Otherwise, the analytical solution is explored to identify the roots of the quartic equation in the MTPA, Flux-Weakening (FW) and MTPV regions. In [40], an analytical solution is presented for regulating the motor's torque. The optimal values for the currents are obtained using Ferrari's method, although this approach is difficult to utilize because it does not take into account the current limit constraint. Moreover, the computation time, for a typical microcontroller platform, is relatively long. To simplify the quartic equation, numerous approximation strategies are investigated. In [41], the Taylor's series is used to lower the orders of the quartic equation. Both the current limit and the voltage ellipse limit are studied, and Euler's quartic solution is employed in [42].
Some publications even focus on numerical solutions. In these techniques, the problem is transformed into two non-linear equations using the Lagrange-multiplier method. Both [43] and [44] employ Newton's method and the Gauss-newton method. However, in these meth-

ods, as it could be assumed, the computing time is relatively decreased, but the accuracy is low, compared to the analytical solution.

In Chapter. 4, a novel analytical solution is presented, based on current magnitude minimization, to obtain the reference currents according to the desired torque. Thanks to a different problem formulation, the proposed method is much simpler than other analytical solutions. In fact, the number of cubic roots (the most demanding operation) to be computed in this case is lower than other analytical models, which greatly helps to decrease the computation time. The method is applied on an IPMSM in MTPA and FW region. Although the MTPV operation is considered in the torque control loop, the proposed method is focused on MTPA and FW regions.

1.4 Non-linear Parameters of the IPMSM

Due to the non-linear magnetic behavior of IPMSM and SynRM, the maps of the flux-linkages (as a function of current) are important for many aspects, including current control, gains adaption and axes decoupling, MTPA, FW and sensor-less control. Off-line characterization approaches require a large amount of time for commissioning and devoted hardware. In the typical process, the parameters will be obtained from the system under test, operating at constant speed condition and steady state, where these parameters are extracted by imposing different reference currents under test. The simplest way for representing flux-linkage is the analytical method with constant machine parameters [11],[45], i.e. iron magnetic saturation is neglected. These methods can be easily implemented in low-cost digital hardware. In order to improve the flux accuracy, a very popular method consists in the use of LUT[46][47]. Approximating functions have also been proposed, e.g. by fitting a polynomial function of currents. The estimated function can be improved by considering other nonlinear parameters like temperature effects, mechanical and iron losses [40]. In this case, all parameters are obtained off-line, then the control parameters are used online to calculate the machine parameters instantaneously. In [48], by using the Group Method of Data Handling (GMDH) method, the apparent inductance is estimated just for sensor-less application. However, the whole map is not approximated, thus limiting the scope of application of the method.
In Chapter. 5, GMDH method is proposed, in order to approximate the flux-linkage maps for an IPMSM. Thanks to the adoption of a neural network, the set of approximating functions is used in an efficient way. The approximation method allows to calculate the flux-linkages online, based on current inputs. The proposed approximation GMDH has been analyzed in a study case. The results show that the accuracy of GMDH is higher than polynomial approximation, according to error percentage (2-3 times smaller error).

1.5 Dead-time compensation

All the techniques for the selection of optimal operating point and for the control of IPMSM and SynRM rely on the possibility to accurately control the stator currents by means of a three-phase voltage source inverter, which is seen as a variable-voltage actuator. However, the non-ideal behavior of the inverter may result in distorted phase currents and so sub-optimal operation of the machine. In order not to degrade the performance of the drive system, compensation of inverter non-linearity are needed. These effects are mainly due to presence of dead-times, voltage drops and parasitic/intrinsic capacitive effects of power devices and electric machine. Accurate compensation of these effects is of paramount importance in many drives applications, as resulting output voltage distortion has strong effects on the performance of current control loop, especially at low speed, where the operating voltage of the machine is comparable to the level of distortion introduced by the non-linearity components. This phenomenon is even more concerning in sensor-less systems, as low-speed performance is heavily affected by the correct knowledge of machine feeding voltage, that is normally not directly measured, as reference values are adopted instead to limit drive electronics complexity. Therefore, inverter non-linearity effects are injected into the estimation loop and degrade the reliability and accuracy of the estimates.

As distortion voltage components depend mainly on leg output currents, most of the compensation techniques proposed in past literature employ a certain voltage to current characteristic to approximate the non-linearity effects, which is often identified within a self-commissioning procedure. The simplest model for dead-time effect considers diode clamping only, and results in a compensation curve that simply depends on current flow direction, as analyzed in a quite old contribution, [49]. Some more recent methodologies propose the use of different correcting functions, e.g. linear saturated, [50], sigmoid, [51], exponential, [52] for approximating and finally compensating the non-linearities. A much more complex method is proposed in [53], requiring a fine external tuning to adapt the compensation function to the commercial drive. The effect of dead-time with different PWM schemes is analyzed in [52], and new non-linearity effect identification is introduced adopting the Discontinuous PWM. The aforementioned approaches require identification of parameters of the correction functions or filling up Look-Up Tables (LUTs), that can be subsequently interpolated online to be used by the control algorithm, [54]. Most compensation methods need current sensors or current references to determine the phase current direction, other approaches [55] [56] use extra hardware for zero-crossing detection, to find the current polarity in order to improve the compensation when the amount of ripple cannot be neglected, e.g. low inductance machines and/or high voltage systems and/or low switching frequency converters feeding the machine.

A quite different approach has been recently introduced, [57], where an analytical model for the physical behavior of the inverter non-linearity is considered, as well as a proper test procedure allowing the self-identification of the parameters of that model, e.g. the equivalent voltage drop, output capacitance and resistance. A crucial aspect, which has been analyzed

and addressed in this thesis, is the autonomous selection of the threshold current of the measured voltage vs. current characteristics, a value whose knowledge is mandatory for the accurate estimation and compensation of the non-linearity effects in a self-commissioning scenario.

1.6 Thesis Overview

In this thesis, the advanced control of Interior Permanent Magnet Synchronous Motor is studied. The PMSM mathematical model, which is necessary for analyzing and controlling the motor, is described in Chapter. 2, along with the description of the main magnetic structures of synchronous motors. The different motor types have also been compared, highlighting their advantages and disadvantages. Following this evaluation of the PMSM analytical model, the equations describing the mechanical and electrical dynamics are obtained. Furthermore, MTPA and FW constraints, operation regions and control implementation illustrate the PMSM's behavior. The motor operates in the MTPA region up to a specific speed (base speed), and at high speeds it functions in the flux-weakening region, as is formulated in this chapter.

The maximum torque per ampere control has been examined in Chapter. 3 for IPMSM and SynRM. The functioning, advantages, and disadvantages of the Real Signal Injection and Virtual Signal Injection algorithms are comprehensively reviewed. Moreover, the stability analysis of MTPA tracking algorithms has been carried out and a gain adaption strategy for both techniques has been proposed. Simulations have been performed to validate the fundamentals of the two techniques and to identify their drawbacks. A specific approach has been adopted for analyzing the MTPA tracking errors of the two methods, i.e. an analytical model was used to create ideal non-linear flux-linkage maps of a "reference" SynRM machine. This allows to remove any potential measuring errors or "glitches" from the real machine flux maps and allow for a very accurate quantitative comparison (based on calculations and simulation). The main computing operations that the control must carry out are also briefly discussed before the tests. Accurate simulation results, also based on an IPMSM, confirm that the RSI algorithm is more accurate than VSI. Given the non-linearity of the tracking loop, a gain adaptation strategy has also been proposed and tested successfully. The VSI ensures faster dynamics, mainly because of the lower impact of measurement noise. It is also shown that, with RSI, large sensors noise is problematic and forces to reduce the tracking bandwidth.

In Chapter. 4, a new analytical solution is studied to control the torque in IPMSM. The proposed approach adopts a vector magnitude minimization criterion to find the MTPA operating point of an IPMSM, for a given desired torque value. By using this method, the quartic equation for calculating the current references is simplified, thanks to the 3^{rd}

and 2^{nd} order coefficients being null. The complexity of the proposed solution is reduced significantly and, in particular, the cubic root needs to be calculated less times than for the method found in literature. The computation time of the proposed method and the previous Ferrari's method are compared experimentally for a typical microcontroller implementation. The computation time is decreased by more than 50% with respect to the classical technique. Furthermore, the novel solution is applied to an IPMSM in MTPA region experimentally considering constant and adaptive q-axis inductance. As a results, the proposed method track the MTPA trajectory with a high accuracy.

In Chapter. 5, the GMDH method is proposed for the approximation of flux linkage maps of an IPMSM. According to this approximation, the inputs are the currents and a suitable set of functions is fitted. The method is compared with a polynomial method, showing that the accuracy of GMDH is higher than polynomial method. In fact, the error is reduced by 2 to 3 times, compared to the polynomial approximation.

The self-commissioning of the dead-time compensation curve is analyzed in Chapter. 6. The adopted model is based on physical parameters, such as the actual dead-time, capacitance of the switching node and total series resistance on the inverter phase. An off-line identification procedure allows to identify all parameters. A crucial aspect of this approach, namely the selection of a threshold separating the linear and non-linear part of the distortion curve, is studied in this chapter. Two new methods are proposed, which ensure minimal identification error. Their development is reported, together with validation, demonstrating the superiority of the results over state-of-the-art approaches. Finally, the effects of the mentioned inverter distortion on the accuracy of current sampling and control loops, mainly dependent on the capacitance value and operating point, are also analyzed for the first time. An original compensation strategy is proposed and validated by means of accurate simulations and experiments.

Chapter 2

Interior Permanent Magnet Synchronous Machine and Synchronous Reluctance Machine

2.1 Introduction

Over the past few decades, numerous studies have been conducted to improve the effectiveness of electrical devices like PMSM, SynRM and PM-SynRM. The greatest torque per ampere contribution, wide speed operating range, and high efficiency of these machines made them attractive for usage in industry [3, 4]. The PMSM have used in many applications. The advantages of this machines are high torque density, high efficiency and operating in wide range speed [2]. Selecting the rare-earth materials is quite important in these kind of machine. Neodymium-iron-boron (Nd-Fe-B) and samarium-cobalt (Sm-Co) are two common materials for permanent magnets. However, The price of theses materials are high and it will increase the cost of the whole machine [8]. Also, there can be some issue with possible faults on the permanent magnets.
SynRM's rotor design distinguishes it from PMSMs. There is not any permanent magnets in the rotor of these kind machine that make it more reliable. In this case, the machine does not have the high cost of PMSM.
In this chapter, the magnetic structure of the Interior Permanent Magnet Synchronous Machine (IPMSM) and Synchronous Reluctance Machine (SynRM) is studied. Then, the dynamical models of the IPMSM is presented. In addition, the Maximum Torque Per Ampere (MTPA), flux-weakening and Maximum Torque Per Voltage (MTPV) are introduced in last sections.

2.1.1 Surface Permanent Magnet Synchronous Machine (SPMSM)

In (Fig. 2.1), an SPMSM's schematic is depicted. The surface of the rotor is where the SPMSM's permanent magnets are mounted. Since the magnetic permeability of ceramic

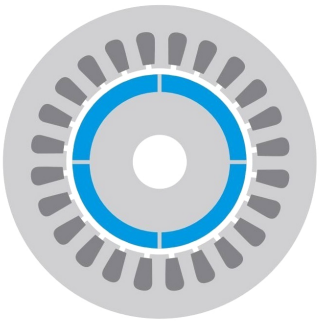

Figure 2.1: Schematic of Surface Permanent Magnet Synchronous Machine (SPMSM).

and rare-earth magnet materials is nearly that of free space, the permanent magnet can be considered as a part of air-gap. As a result, the effective airgap of an SPMSM as viewed by the stator windings is equal to the sum of the permanent magnet thickness product and airgap [58]. Due to the homogeneity of the air-gap thickness, the winding's inductance is almost unaffected by the position of the rotor. Due to the interaction of the permanent magnet and armature reaction fields, SPMSMs only have the aligning torque contribution. SPMSMs utilize a lot of permanent magnets since the reluctance torque component is absent, which makes it challenging to manage in the region of weakening fields. The maximum induced Electro Motive Force (EMF) needs to be bounded in order to keep safety at high speeds in the case that the inverter drives the SPMSM fails. Because both torque and back EMF of a SPMSM are related to the flux-linkage of the permanent magnet, this requirement conflicts with the necessity for high torque. The only solution to overcome this issue is to increase the inverter's Voltage-Ampere (VA) rating, which results in massive inverters and cost.

2.1.2 Interior Permanent Magnet Synchronous Machine (IPMSM)

Fig. 2.2 display a possible structure of IPMSM (V-shaped PMs). IPMSM, Radially Internal Permanent Magnet Synchronous Machine (RI-PMSM), and V-Shaped Internal Permanent Magnet Synchronous Machine (VI-PMSM) are some types of typical IPMSMs rotor topologies. IPMSMs have permanent magnets that are mounted inside the rotor compared to SPMSMs, and this distinction provides several benefits. First, because the steel rotor core physically encloses and protects the permanent magnets, IPMSMs are more mechanically robust and applicable for high speed, high torque processes. Second, because the steel rotor core's magnetic permeability different from the permanent magnet, rotor position affects the winding inductance, providing reluctance torque and improving capability in the flux weakening region. Additionally, the IPMSMs offer excellent overload capability throughout the full speed range [59].

Since the permanent magnet flux-linkage contributes to the motor torque, the back-emf of the IPMSM at high velocity is substantially lower than that of an equivalent SPMSM.

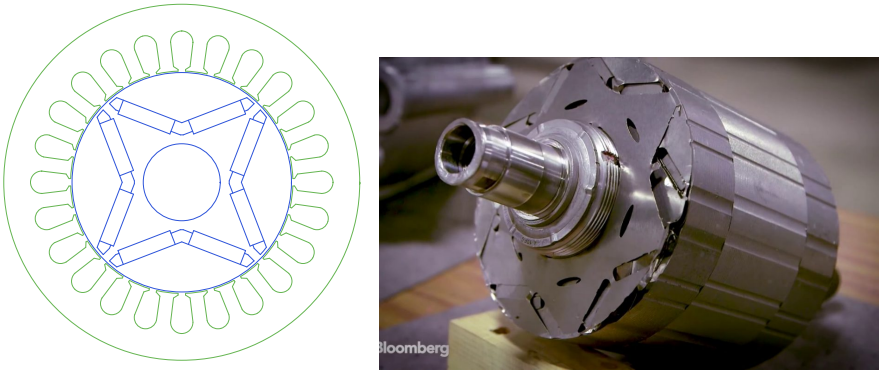

Figure 2.2: Schematic and photograph of Interior Permanent Magnet Synchronous Machine (V-shaped).

2.1.3 Synchronous Reluctance Machine (SynRM)

SynRM has some advantages, i.e, motor simple design, lack of permanent magnet and winding in the rotor and rotor with a low moment of inertia. The machines have a high efficiency due to the lack of windings on the rotor. Thus, there is a lower value of overheating of the stator winding and bearing assemblies that decrease the whole losses in the motor. However, compared to permanent magnet (PM) machines, the torque density, power density, and power factor (PF) of SynRMs are relatively low, that adding PMs into SynRM rotors could enhance motor performance. A schematic and photograph of an industrial SynRM is shown in Fig. 2.3.

The Synchronous Reluctance Motor (SynRM) utilizes the reluctance concept and rotating sinusoidal MMF, which can be produced by the traditional 3-phase stator, for torque production. In the SynRM, field is produced by a sinusoidally distributed winding in a slotted stator and it links the stator and rotor through a small air gap. The field is rotating at synchronous speed, and can be assumed to have a sinusoidal distribution.

Figure 2.3: Schematic and Photograph of Synchronous Reluctance Machine.

2.2 Machine Dynamical Models

2.2.1 IPMSM mathematical model in the stator reference frame

IPMSMs are rapidly being utilized in automobile tractions and a range of applications because of their benefits. Both Direct Torque Control (DTC) [60–64] and Direct Flux Vector Control (DFVC) [65–67] in the stator flux-linkage synchronous reference frame as well as Field Oriented Control (FOC) in the rotor synchronous reference dq frame [9, 34, 68] can be used to control IPMSMs. It is vital to understand the dynamic and mathematical machine model as well as its electrical and magnetic properties in order to investigate the electric and magnetic behavior of the IPMSM under various operating situations. Several dynamic and mathematical IPMSM models are reported in the literature [69–73]. The traditional dynamic and mathematical machine models are discussed in this section. The conventional dynamic and mathematical IPMSM model's foundational simplifying assumptions are as follows:

- sinusoidal spatial distribution of the Magneto Motive Force (MMF) force in the air gap;
- linear magnetic behavior of the machine and lack of cross-saturation effects (these hypotheses will be eliminated later, in particular when dealing with MTPA tracking);
- lack of hysteresis and eddy currents in the iron core;
- lack of slot harmonic effects,
- lack of temperature effects on the machine.

The general voltage formulae are as follows once referring to a three-phase machine:

$$\begin{cases} u_a = R_s i_a(t) + \frac{d\lambda_a(t,\theta_e)}{dt} \\ u_b = R_s i_b(t) + \frac{d\lambda_b(t,\theta_e)}{dt} \\ u_c = R_s i_c(t) + \frac{d\lambda_c(t,\theta_e)}{dt} \end{cases} \tag{2.1}$$

Where λ_i is the magnetic flux-linkage, u_i is the phase voltage and i_i is the phase current for i phase. R_s is the phase resistance, which ought to be the same for each of the three phases. In an IPMSM, both the currents flowing through each stator phase and the magnetic flux coming from the rotor permanent magnets affect flux-linkage to the stator phases. Given the assumption of linear magnetic behavior (or constant magnetic permeability) and negligible iron losses, the following relationships can be used to express the flux-linkage:

$$\begin{cases} \lambda_a(t) = \lambda_{a,i}(t) + \Lambda_{mg_a}(t) \\ \lambda_b(t) = \lambda_{b,i}(t) + \Lambda_{mg_b}(t) \\ \lambda_c(t) = \lambda_{c,i}(t) + \Lambda_{mg_c}(t) \end{cases} \tag{2.2}$$

where Λ_{mg_n} is the flux-linkage created by permanent magnets and $\lambda_{n,i}$ is the flux-linkage created by stator current excitation. On the basis of the model, it is possible to assume that the flux-linkage Λ_{mg_a}, Λ_{mg_b}, and Λ_{mg_c} are sinusoidal:

$$\begin{cases} \Lambda_{mg_a} = \Lambda_{mg} cos(p_p \theta_r) \\ \Lambda_{mg_b} = \Lambda_{mg} cos(p_p \theta_r - \frac{2}{3}\pi) \\ \Lambda_{mg_c} = \Lambda_{mg} cos(p_p \theta_r - \frac{4}{3}\pi) \end{cases} \tag{2.3}$$

where Λ_{mg} indicates the maximum flux-linkage induced by permanent magnets in each phase and p_p is the pole pairs. The following relationships can be used to express the flux-linkage that is generated by stator current excitation:

$$\begin{cases} \lambda_{a,i} = L_{aa} i_a + L_{ab} i_b + L_{ac} i_c \\ \lambda_{b,i} = L_{ba} i_a + L_{bb} i_b + L_{bc} i_c \\ \lambda_{c,i} = L_{ca} i_a + L_{cb} i_b + L_{cc} i_c \end{cases} \tag{2.4}$$

Whereas the three phases' self-inductances are L_{aa}, L_{bb}, and L_{cc}, the mutual-inductances between the three phases are L_{ab}, L_{bc}, and L_{ac}. It can be considered that the self and mutual inductances as being time and rotor position dependent.

$$\begin{cases} L_{aa} = L_{\sigma s} + L_{ms0} + L_m cos(2p_p \theta_r) \\ L_{bb} = L_{\sigma s} + L_{ms0} + L_m cos(2p_p \theta_r - \frac{2}{3}\pi) \\ L_{cc} = L_{\sigma s} + L_{ms0} + L_m cos(2p_p \theta_r - \frac{4}{3}\pi) \end{cases} \tag{2.5}$$

It is determined by adding a constant term ($L_{\sigma s} + L_{ms0}$) and a sinusoidal term with a double electrical frequency (amplitude L_m). The stator flux that surrounds in the air without affecting the rotor is represented by the constant $L_{\sigma s}$, which is relative to the leakage inductance. L_{ms0} and L_m stand for the magnetization inductance's constant component and anisotropy component's amplitude ($2p_p\theta_r$ angle function), respectively. The mutual inductances account for the flux that each winding links to the other windings' current flow. These also depend on the machine's anisotropy and can be described by the relationships shown below:

$$\begin{cases} L_{ab} = L_{ba} = -M_s + L_m cos(2p_p \theta_r - \frac{2}{3}\pi) \\ L_{bc} = L_{cb} = -M_s + L_m cos(2p_p \theta_r) \\ L_{ca} = L_{ac} = -M_s + L_m cos(2p_p \theta_r - \frac{4}{3}\pi) \end{cases} \tag{2.6}$$

where M_s is the average mutual induction coefficient among the stator winding's phases. The following matrix represents the relationships mentioned above:

$$\begin{bmatrix} u_a \\ u_b \\ u_c \end{bmatrix} = \begin{bmatrix} R_s & 0 & 0 \\ 0 & R_s & 0 \\ 0 & 0 & R_s \end{bmatrix} \begin{bmatrix} i_a \\ i_b \\ i_c \end{bmatrix} + \frac{d \begin{bmatrix} \lambda_a \\ \lambda_b \\ \lambda_c \end{bmatrix}}{dt} \tag{2.7}$$

$$\begin{bmatrix} \lambda_a \\ \lambda_b \\ \lambda_c \end{bmatrix} = \begin{bmatrix} L_{aa} & L_{ab} & L_{ac} \\ L_{ba} & L_{bb} & L_{bc} \\ L_{ca} & L_{cb} & L_{cc} \end{bmatrix} \begin{bmatrix} i_a \\ i_b \\ i_c \end{bmatrix} + \begin{bmatrix} \Lambda_{mg_a} \\ \Lambda_{mg_b} \\ \Lambda_{mg_c} \end{bmatrix} \tag{2.8}$$

Another way to state the Eq. 2.7 and Eq. 2.8 compactly is as follows:

$$[u_{abc}] = [R_s][i_{abc}] + \frac{d[\lambda_{abc}]}{dt} \tag{2.9}$$

$$[\lambda_{abc}] = [L_{abc}][i_{abc}] + [\Lambda_{mg_{abc}}] \tag{2.10}$$

Eq. 2.10 can be substituted for Eq. 2.9 of electric voltage.

$$\begin{aligned} [u_{abc}] = [R_s][i_{abc}] + \frac{d[L_{abc}][i_{abc}] + [\Lambda_{mg_{abc}}]}{dt} = \\ = [R_s][i_{abc}] + \frac{d[L_{abc}]}{dt}[i_{abc}] + \frac{d[i_{abc}]}{dt}[L_{abc}] + \frac{d[\Lambda_{mg_{abc}}]}{dt} = \\ = [R_s][i_{abc}] + \frac{d\theta_r}{dt}\frac{d[L_{abc}]}{d\theta}[i_{abc}] + \frac{d[i_{abc}]}{dt}[L_{abc}] + \frac{d\theta_r}{dt}\frac{d[\Lambda_{mg_{abc}}]}{d\theta_r} = \\ = [R_s][i_{abc}] + \omega_m\frac{d[L_{abc}]}{d\theta_r}[i_{abc}] + [L_{abc}]\frac{d[i_{abc}]}{dt} + \omega_m\frac{d[\Lambda_{mg_{abc}}]}{d\theta_r} \end{aligned} \tag{2.11}$$

where, $[R_s][i_{abc}]$ are the components of the drop voltages in phases a, b and c. $[L_{abc}]\frac{d[i_{abc}]}{dt}$ are the induced back EMF to stator windings. $\omega_m\frac{d[L_{abc}]}{d\theta_r}[i_{abc}]$ are the rotational back EMF caused by the machine's anisotropy and $\omega_m\frac{d[\Lambda_{mg_{abc}}]}{d\theta_r}$ are the rotationally-induced back EMF that permanent magnet flux produces.

Input power expression can be obtain by multiplying the transposed vector of the currents $[i_{abc}]^T$ to the all components of Eq. 2.11.

$$\begin{aligned} [P_{e_{abc}}] = [i_{abc}]^T[u_{abc}] = [i_{abc}]^T[R_s][i_{abc}] + [i_{abc}]^T\omega_m\frac{d[L_{abc}]}{d\theta_r}[i_{abc}] + \\ [L_{abc}][i_{abc}]^T\frac{d[i_{abc}]}{dt} + \omega_m[i_{abc}]^T\frac{d[\Lambda_{mg_{abc}}]}{d\theta_r} \end{aligned} \tag{2.12}$$

where, $[i_{abc}]^T[u_{abc}]$, $[i_{abc}]^T[R_s][i_{abc}]$, $[L_{abc}][i_{abc}]^T\frac{d[i_{abc}]}{dt}$, $[i_{abc}]^T\omega_m\frac{d[L_{abc}]}{d\theta_r}[i_{abc}]+\omega_m[i_{abc}]^T\frac{d[\Lambda_{mg_{abc}}]}{d\theta_r}$ represents input electric power(P_e), stator winding losses (P_{cu}), stored power in magnetic field and motor's shaft mechanical power (P_m) respectively.

As a result, the following relationship can be used to express the electromechanical torque to the shaft:

$$T_{em} = \frac{P_m}{\omega_m} = [i_{abc}]^T \frac{d[L_{abc}]}{d\theta_r}[i_{abc}] + [i_{abc}]^T \frac{d[\Lambda_{mg_{abc}}]}{d\theta_r} \tag{2.13}$$

where the reluctance torque component is $[i_{abc}]^T \frac{d[L_{abc}]}{d\theta_r}[i_{abc}]$. $[i_{abc}]^T \frac{d[\Lambda_{mg_{abc}}]}{d\theta_r}$ is a representation of the torque created by the machine as a result of the interplay between the flux generated by the permanent magnets and the currents flowing through the phases of the stator. The resulting mathematical representation of the IPMSM consists of a set of non-linear differential equations with difficult solutions. This problem is solved by using a mathematical approach that involves changing the coordinates from the *abc* stator reference frame system to the synchronized $dq0$ reference frame system.

2.2.2 $dq0$ synchronous reference frame for the IPMSM mathematical model

Three differential equations with variable coefficients make up the mathematical model in the stator reference frame system mentioned in the previous section. It is complicated the use of such a mathematical model for the purpose of operating an IPMSM. You can apply linear mathematical transformations to create differential equations with constant parameters. In particular, the Park transformation enables the change from a three-phase stator reference system to a two-phase reference frame system, with the real axis aligned with the polar rotor axis and spinning at the electrical rotor speed ω_{me}. This transformation has the benefit of being simplified to a set of equations in the reference $dq0$, where the self- and mutual-induction coefficients are independent of the rotor location and remain constant over time. As seen in Fig. 2.4, the stator reference system (a,b,c) is first transformed into the fixed two-phase reference system (α,β) in order to achieve the Park model.

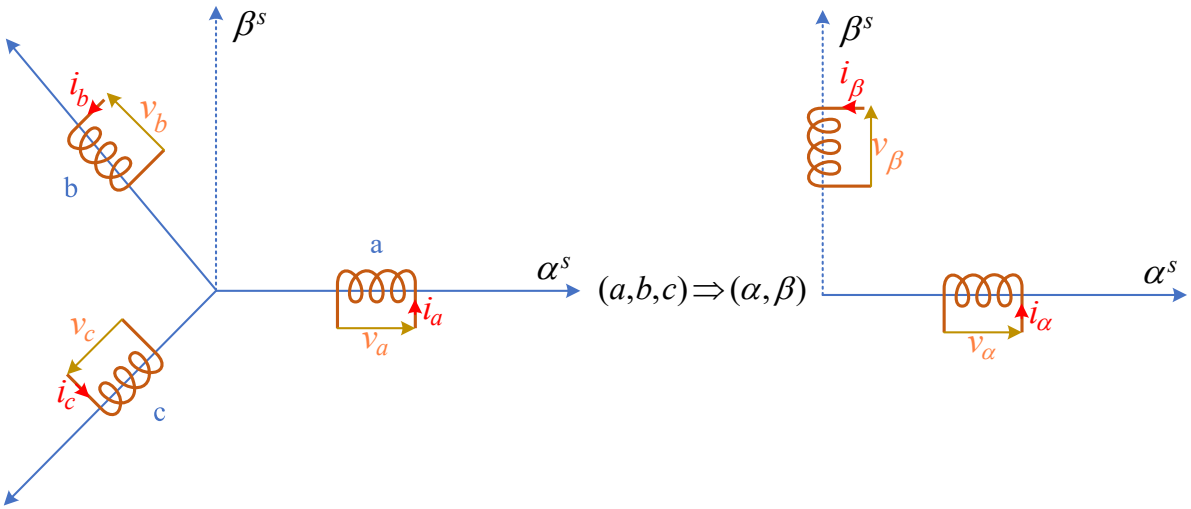

Figure 2.4: Transformation of coordinated from (a,b,c) to (α,β).

A system with only two windings aligned at 90 degrees and that is magnetically uncoupled is the result of such a transformation. The inductive coefficients are still a function of the

angular position of the rotor in this model because the stator and rotor parameters are evaluated in relation to the appropriate physical reference frame. To express stator and rotor quantities under a single reference, a further transformation is required. The rotor quantities are studied in relation to a system of axes $(d,q,0)$ revolving integrally with the rotor. Fig. 2.5 depicts this additional coordinates transformation, in which the stator quantities referred to the system (d,q) are provided.

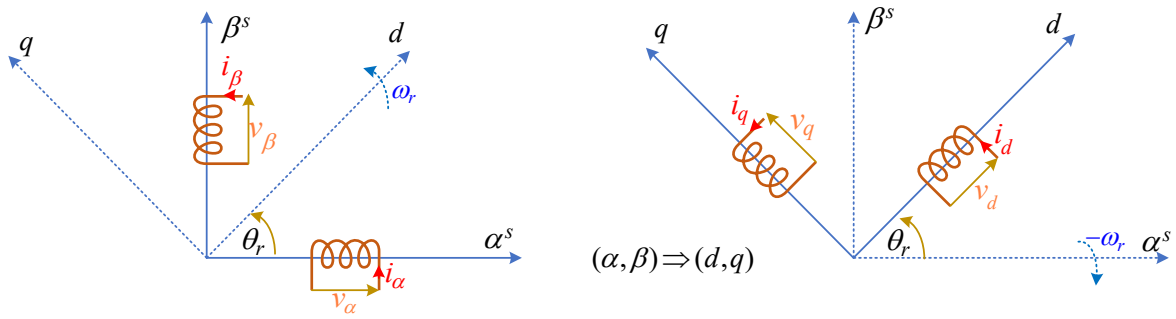

Figure 2.5: Transformation of coordinated from (α,β) to (d,q).

The following transformation matrix is used to convert the quantities from the three-phase reference system (a,b,c) to the reference system $(d,q,0)$:

$$[T] = \frac{2}{3}\begin{bmatrix} cosp\theta_r & cos(p\theta_r - \frac{2}{3}\pi) & cos(p\theta_r - \frac{4}{3}\pi) \\ -sinp\theta_r & -sin(p\theta_r - \frac{2}{3}\pi) & -sin(p\theta_r - \frac{4}{3}\pi) \\ \frac{1}{2} & \frac{1}{2} & \frac{1}{2} \end{bmatrix} \tag{2.14}$$

The inverse matrix, which enables the conversion of the quantities from the coordinate system $(d,q,0)$ to the three-phase coordinate system (a,b,c), also can be defined:

$$[T]^{-1} = \frac{2}{3}\begin{bmatrix} cosp\theta_r & -sinp\theta_r & 1 \\ cos(p\theta_r - \frac{2}{3}\pi) & -sin(p\theta_r - \frac{2}{3}\pi) & 1 \\ cos(p\theta_r - \frac{4}{3}\pi) & -sin(p\theta_r - \frac{4}{3}\pi) & 1 \end{bmatrix} \tag{2.15}$$

The following relationships define the electrical quantities in the $(d,q,0)$ reference system:

$$[u_{dq0}] = [T][u_{abc}] = \frac{2}{3}\begin{bmatrix} cosp\theta_r & cos(p\theta_r - \frac{2}{3}\pi) & cos(p\theta_r - \frac{4}{3}\pi) \\ -sinp\theta_r & -sin(p\theta_r - \frac{2}{3}\pi) & -sin(p\theta_r - \frac{4}{3}\pi) \\ \frac{1}{2} & \frac{1}{2} & \frac{1}{2} \end{bmatrix} \begin{bmatrix} u_a \\ u_b \\ u_c \end{bmatrix} \tag{2.16}$$

$$[i_{dq0}] = [T][i_{abc}] = \frac{2}{3}\begin{bmatrix} cosp\theta_r & cos(p\theta_r - \frac{2}{3}\pi) & cos(p\theta_r - \frac{4}{3}\pi) \\ -sinp\theta_r & -sin(p\theta_r - \frac{2}{3}\pi) & -sin(p\theta_r - \frac{4}{3}\pi) \\ \frac{1}{2} & \frac{1}{2} & \frac{1}{2} \end{bmatrix} \begin{bmatrix} i_a \\ i_b \\ i_c \end{bmatrix} \tag{2.17}$$

$$[\lambda_{dq0}] = [T][\lambda_{abc}] = \frac{2}{3}\begin{bmatrix} cosp\theta_r & cos(p\theta_r - \frac{2}{3}\pi) & cos(p\theta_r - \frac{4}{3}\pi) \\ -sinp\theta_r & -sin(p\theta_r - \frac{2}{3}\pi) & -sin(p\theta_r - \frac{4}{3}\pi) \\ \frac{1}{2} & \frac{1}{2} & \frac{1}{2} \end{bmatrix}\begin{bmatrix}\lambda_a \\ \lambda_b \\ \lambda_c\end{bmatrix} \tag{2.18}$$

The flux equation for the IPMSM mathematical model is as follows after applying the previous indicated coordinate transformation:

$$\begin{aligned}[\lambda_{dq0}] = [T][\lambda_{abc}] = [T][L_{abc}][i_{abc}] + [T][\Lambda_{mg_{abc}}] = \\ [T][L_{dq0}][T]^{-1}[i_{dq0}] + [T][T]^{-1}[\lambda_{dq0}] = \begin{bmatrix} L_d & 0 & 0 \\ 0 & L_q & 0 \\ 0 & 0 & L_0 \end{bmatrix}\begin{bmatrix} i_a \\ i_b \\ i_c \end{bmatrix} + \begin{bmatrix} \Lambda_{mg} \\ 0 \\ 0 \end{bmatrix}\end{aligned} \tag{2.19}$$

The voltage equations can be obtained as follow:

$$\begin{aligned}[u_{dq0}] = [T][u_{abc}] = [T][R_s][i_{abc}] + [T]\frac{d[\lambda_{abc}]}{dt} = \\ = [T][R_s][T]^{-1}[i_{dq0}] + [T]\frac{d([T^{-1}][\lambda_{dq0}])}{dt} \\ = R_s\begin{bmatrix} i_d \\ i_q \\ i_0 \end{bmatrix} + [T][T]^{-1}\frac{d\begin{bmatrix}\lambda_d \\ \lambda_q \\ \lambda_0\end{bmatrix}}{dt} + [T]\omega_m\frac{d[[T]^{-1}]}{d\theta}\begin{bmatrix}\lambda_d \\ \lambda_q \\ \lambda_0\end{bmatrix} = \\ = R_s\begin{bmatrix} i_d \\ i_q \\ i_0 \end{bmatrix} + \frac{d\begin{bmatrix}\lambda_d \\ \lambda_q \\ \lambda_0\end{bmatrix}}{dt} + p_p\omega_m\begin{bmatrix}-\lambda_d \\ \lambda_q \\ \lambda_0\end{bmatrix}\end{aligned} \tag{2.20}$$

The voltage equation was formed by substituting Eq. 2.19 for Eq. 2.20.

$$\begin{bmatrix} u_d \\ u_q \\ u_0 \end{bmatrix} = R_s\begin{bmatrix} i_d \\ i_q \\ i_0 \end{bmatrix} + \begin{bmatrix} L_d & 0 & 0 \\ 0 & L_q & 0 \\ 0 & 0 & L_0 \end{bmatrix}\frac{d\begin{bmatrix} i_d \\ i_q \\ i_0 \end{bmatrix}}{dt} + p\omega_m\begin{bmatrix} -L_q i_q \\ L_d i_d + \Lambda_{mg} \\ 0 \end{bmatrix} \tag{2.21}$$

The following expression provides the (d,q,0) coordinate system's power balance:

$$P_i = [i_{abc}]^T[u_{abc}] = [i_{dq0}]([T]^{-1})^T[T]^{-1}[u_{dq0}] = \frac{3}{2}(u_d i_d + u_q i_q + u_0 i_0) \tag{2.22}$$

By using this equation, the following results are obtained:

$$
\begin{aligned}
P_i = [i_{abc}]^T[u_{abc}] = [i_{dq0}]([T]^{-1})^T[T]^{-1}[u_{dq0}] = \\
[i_{dq0}]([T]^{-1})^T[T]^{-1}([R_s][i_{dq0}] + [L_{dq0}]\frac{d}{dt}[i_{dq0}] + p_p\omega_m \begin{bmatrix} -\lambda_q \\ \lambda_d \\ \lambda_0 \end{bmatrix}) = \\
= [i_{dq0}]([T]^{-1})^T[T]^{-1}[R_s][i_{dq0}] + [i_{dq0}]([T]^{-1})^T[T]^{-1}[L_{dq0}]\frac{d}{dt}[i_{dq0}] \\
+[i_{dq0}]([T]^{-1})^T[T]^{-1}p_p\omega_m \begin{bmatrix} -\lambda_q \\ \lambda_d \\ \lambda_0 \end{bmatrix}
\end{aligned}
\tag{2.23}
$$

Where the first term represents the joule losses in the stator windings P_{cu}, the second term represents variation in the time unit of the energy stored in the magnetic field produced by the armature ampere-turns (P_{mf}) and the last term represents the output electromechanical power P_m. The electromechanical power P_m is equal to:

$$
\begin{aligned}
P_m = [i_{dq0}]([T]^{-1})^T[T]^{-1}p_p\omega_m \begin{bmatrix} -\lambda_q \\ \lambda_d \\ \lambda_0 \end{bmatrix} = \frac{3}{2}p_p\omega_m[\lambda_d i_q - \lambda_q i_d] = \\
= \frac{3}{2}p_p\omega_m[\Lambda_{mg} i_q + (L_d - L_q) i_d i_q]
\end{aligned}
\tag{2.24}
$$

It is feasible to extract the electromechanical torque expression from this equation:

$$
T_e = \frac{3}{2}p_p[\lambda_d i_q - \lambda_q i_d] = \frac{3}{2}p_p[\Lambda_{mg} i_q + (L_d - L_q) i_d i_q] \tag{2.25}
$$

The expression of electromechanical torque consists of two parts: the fundamental torque, which depends on the flux-linkage induced by permanent magnets and q-axis current, and the reluctance torque, which depends on the saliency of the machine and both d- and q-axis currents. Below, all the dynamic and mathematical model equations are presented:

$$
u_d = R_s i_d + L_d\frac{di_d}{dt} - p_p\omega_m L_q i_q \tag{2.26}
$$

$$
u_q = R i_q + L_q\frac{di_q}{dt} + p\omega_m L_d i_d + p\omega_m\Lambda_{mg} \tag{2.27}
$$

$$
T_e = \frac{3}{2}p_p[\Lambda_{mg} i_q + (L_d - L_q) i_d i_q] \tag{2.28}
$$

$$
T_e = T_r + F\omega_m + J\frac{d\omega_m}{dt} \tag{2.29}
$$

$$
\frac{d}{dt}\theta_r = \omega_m \tag{2.30}
$$

2.3 Control Strategies

2.3.1 Current, Voltage and Speed Limits

The voltage of the inverter needs to be higher than the motor-terminals voltage in order to control the motor current. The DC link voltage, on the other hand, is constrained. The IPMSM dynamics steady state model is presented as:

$$U_d = R_s I_d - \Omega_{me} L_q I_q \tag{2.31}$$

$$U_q = R_s I_q - \Omega_{me} L_d I_d + \Omega_{me} \Lambda_{mg} \tag{2.32}$$

The current and voltage vectors in steady state condition are illustrated in Fig. 2.6 based on Eq. 2.31 and Eq. 2.32. When $i_d < 0$ and $i_d > 0$ during motoring, two aspects are compared. Since $\Omega_{me} L_d i_d < 0$ is laid on the q-axis, as shown in Fig. 2.6a, the negative d-axis current lowers the voltage at the motor terminals. By canceling off the back EMF by this coupling voltage, $\omega_{me}\Lambda_{mg}$, which increases with speed. Therefore, it enhances the speed range. On the other hand, positive d-axis current, raises the voltage vector. In order

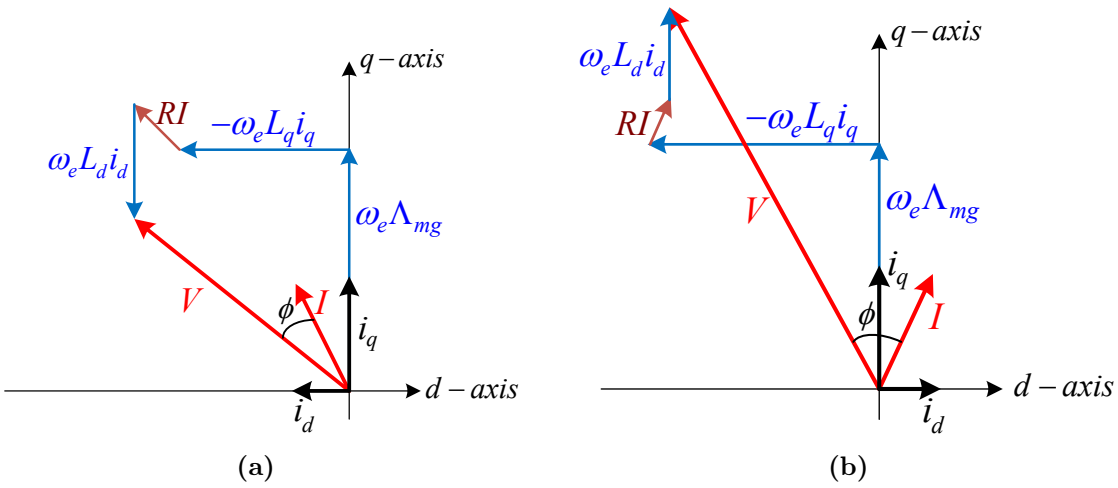

Figure 2.6: Voltage magnitude and power factor depending on i_d polarities during motoring: (a) $i_d < 0$ and (b) $i_d > 0$.

to keep the current under control the terminal voltage must not exceed the available voltage from the inverter. Fig. 2.6a the angle difference, ϕ is not very large and both the current and voltage vectors are in the second quadrant. According to Fig. 2.6b, the vectors of the current and voltage are in distinct quadrants if $i_d > 0$. As a result, the power factor is low. Last but not least, negative $d-$axis current improves power factor while limiting voltage rise. The torque expression Eq. 2.28 can be rewritten as

$$T_e = \frac{3}{2} p_p [\Lambda_{mg} + (L_d - L_q) i_d] i_q \tag{2.33}$$

Since L_q is expected to be greater than L_d, the term $(L_d - L_q)i_d$ is positive when the d-axis current is negative, which increases $\Lambda_{mg} + (L_d - L_q)i_d$ with respect to the case with $i_d = 0$. As a result, negative d-axis current leads to increased torque, for the same q-axis current, i.e. the reluctance torque adds to the electro-dynamical one. The former can be as large as the latter component, in some well-designed IPMSMs, especially when operating at high speeds. Finally, the current vector is parallel to the Ohmic voltage drop. Although the resistive voltage increases the magnitude of terminal voltage, its contribution can be neglected at high speed, for the sake of simplicity, since this voltage component is typically small with respect to the $\omega_{me}\lambda_{d,q}$ terms. Similar vector diagrams in the case of regeneration are shown in Fig. 2.7. The shaft torque is negative if i_q is negative. It functions as a generator by absorbing external mechanical power and transforming it into electrical power. When $i_q < 0$, the two scenarios are compared. With regard to the magnitude of the terminal voltage, the same effect can be seen. With $i_d < 0$, the terminal voltage is lower. When regeneration occurs, it is preferred to obtain a power factor of -1 ($PF = -1$), or ($\phi \approx 180°$) in this case. From this vantage point, the scenario where $i_d < 0$ is better. The Ohmic voltage drop, as opposed to motoring, aids in reducing the terminal voltage.

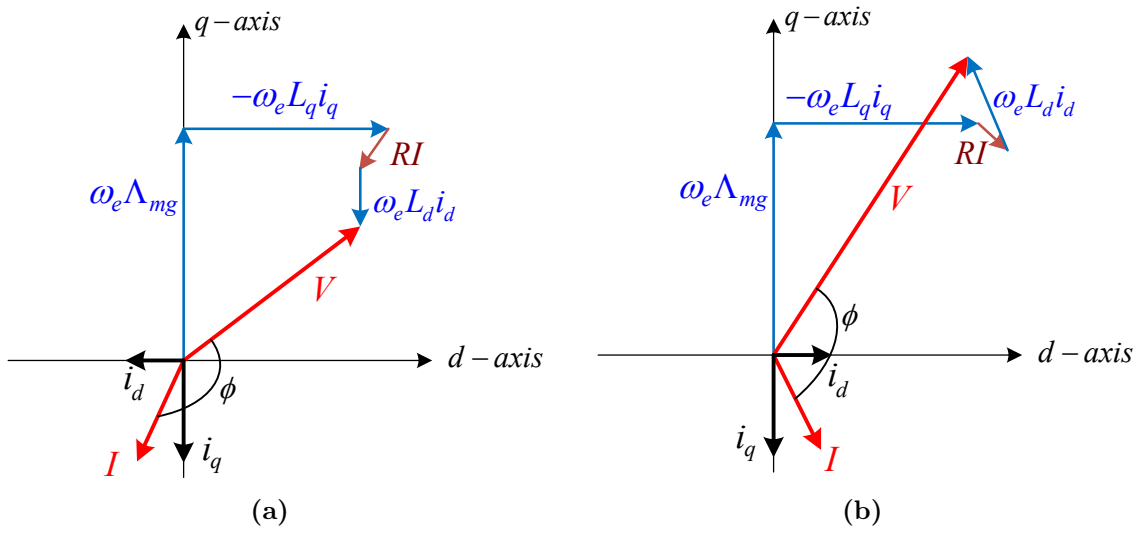

Figure 2.7: Voltage magnitude and power factor depending on i_d polarities during motoring: (a) $i_d < 0$ and (b) $i_d > 0$.

Torque Versus Current Angle A lossless model's vector diagram can be shown in Fig. 2.8. The current angle β is typically considered starting from the q-axis. It follows from the polar description that

$$i_d = -I sin\beta \tag{2.34}$$

$$i_q = I cos\beta \tag{2.35}$$

where $I = \sqrt{i_d^2 + i_q^2}$ and $\beta = tan^{-1}(\frac{-i_d}{i_q})$. With Eq. 2.34 and Eq. 2.35 as substitutes in the torque equation,

$$T_e = \frac{3}{2} p_p [\Lambda_{mg} I cos(\beta) - \frac{1}{2}(L_d - L_q) I^2 sin(2\beta)] \tag{2.36}$$

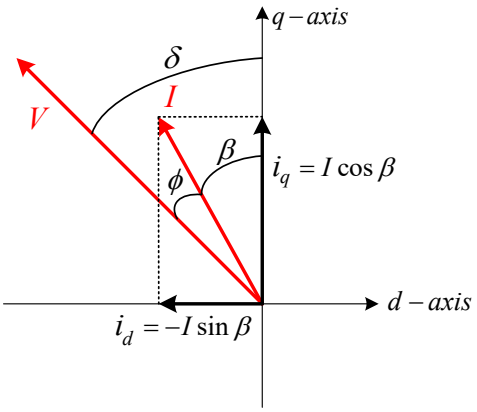

Figure 2.8: Vector diagram of a lossless model.

Also take note that the current angle must be greater than zero ($\beta > 0$) in order for the reluctance torque to be positive when $L_q > L_d$. It implies that the current along the d-axis must be negative. When $L_q > L_d$, torque is illustrated against current angle in Fig. 2.9. For a medium value of β, the reluctance torque's relative magnitude is not low.

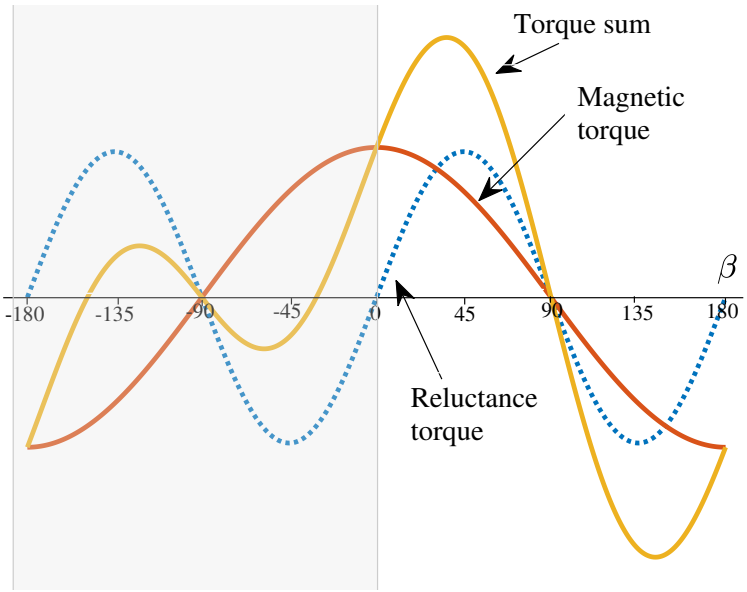

Figure 2.9: Torque against the current angle for a given value of current amplitude.

2.3.2 MTPA Classification and Implementation scheme

It is important to classify the MTPA estimation method in order to their dependence and independence to the motor non-linear parameters. Fig. 2.10 illustrate a taxonomy of MTPA

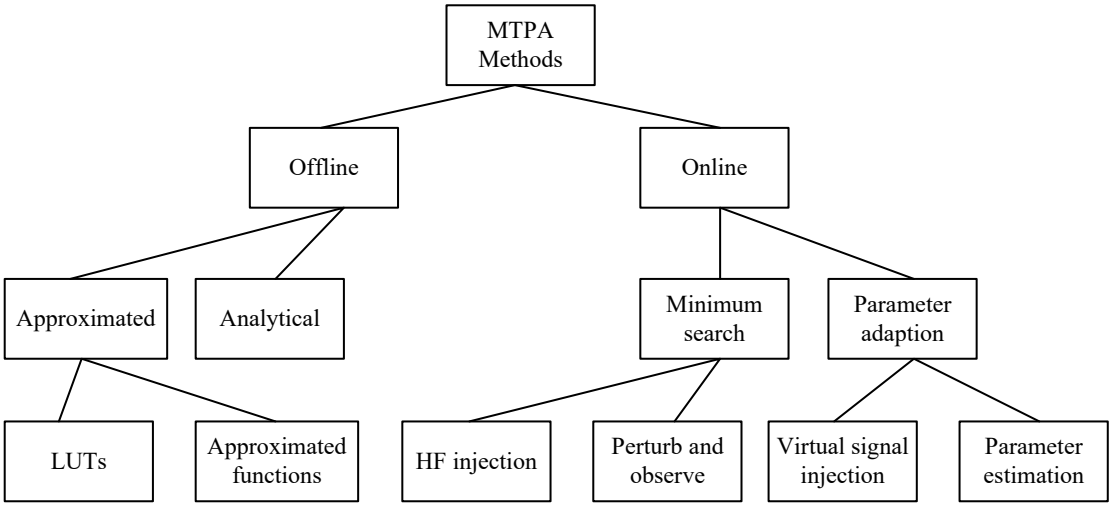

Figure 2.10: Taxonomy of MTPA techniques.

estimation methods that it is divided to two main families, i.e, online and offline [17]. Commonly the speed controller's output is applied to the MTPA algorithm. However, depends on the MTPA estimation methods the input can be different. After processing the $d-$ and $q-$ axis reference currents should be obtained.
In conventional method of MTPA estimation, the differentiation of T_e with respect to β is taken:

$$\frac{\partial T_e}{\partial \beta} = \frac{3p_p}{2}[-\Lambda_{mg} I sin + (L_d - L - q) I^2 cos2\beta] = 0 \tag{2.37}$$

thus,

$$2(L_d - L_q) I sin^2\beta + \Lambda_{mg} sin\beta - (L_d - L_q) I = 0 \tag{2.38}$$

Fig. 2.11 illustrate the MTPA trajectory in dq axis currents.

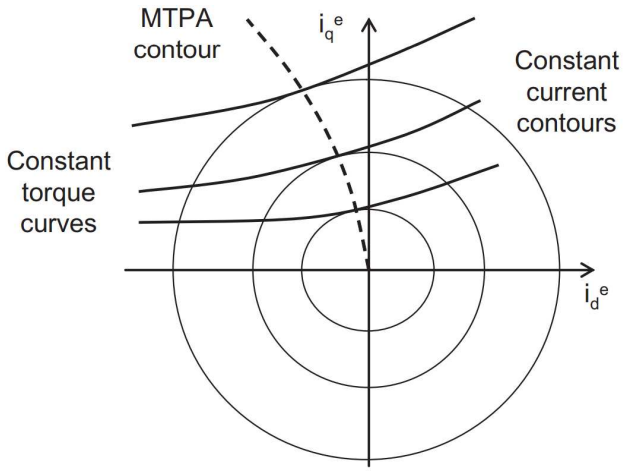

Figure 2.11: MTPA trajectory.

The angle β can be obtained:

$$\beta = sin^{-1}\left[\frac{-\Lambda_{mg} + \sqrt{\Lambda_{mg} + 8(L_d - L_q)^2 I^2}}{8(L_d - L_q)^2 I^2}\right] \tag{2.39}$$

Eq. 2.39 is the loss minimization current angle for a given current magnitude I. according to $i_d = -I_s sin\beta$ the dq reference currents are obtained.

$$i_d = \frac{\Lambda_{mg} - \sqrt{\Lambda_{mg}^2 + 8I^2(L_d - L_q)^2}}{4(L_d - L_q)} \tag{2.40}$$

$$i_q = \sqrt{I^2 - i_d^2} \tag{2.41}$$

As it illustrated in Fig. 2.12 the MTPA input is x and the output is (y_1,y_2) which they can be different parameters. In Field Oriented Control (FOC) technique, the outputs usually are $d-$ and $q-$ reference currents, i.e i_d^* and i_q^*. there are some different MTPA estimation

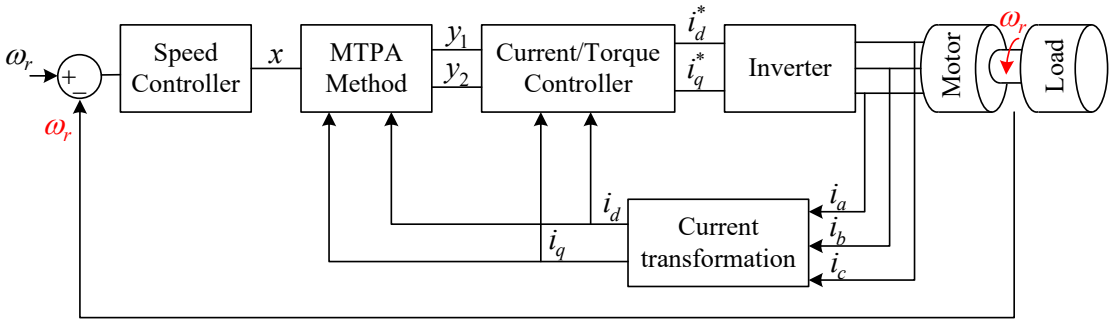

Figure 2.12: General block diagram with MTPA technique.

method configuration that are presented in Fig. 2.13

As it mentioned before, these different implementations can be used online and offline. In offline methods, an open loop is used to modify the reference currents. In some methods such as Real Signal Ingection (RSI) and Virtual Signal Injection (VSI) a feedback from measured current is needed to modify the reference currents. In Fig. 2.13a, the input is the reference torque and the outputs are the reference currents. Also, the amplitude of the stator current can be used as the input of the MTPA calculation block. In this implementation the angle between i_d and i_q (Fiq. 2.13b) is modified. Fig. 2.13c shows another configuration of the MTPA technique implementation with reference torque as the input. In this configuration $q-$axis current is a function of the torque and obtained $d-$axis reference current.
Furthermore, approximation can be used to implement MTPA estimation methods. In this implementation outputs can be polynomial functions that are estimated by the non-linear parameters and measured currents of the motor (Fig.2.13d).

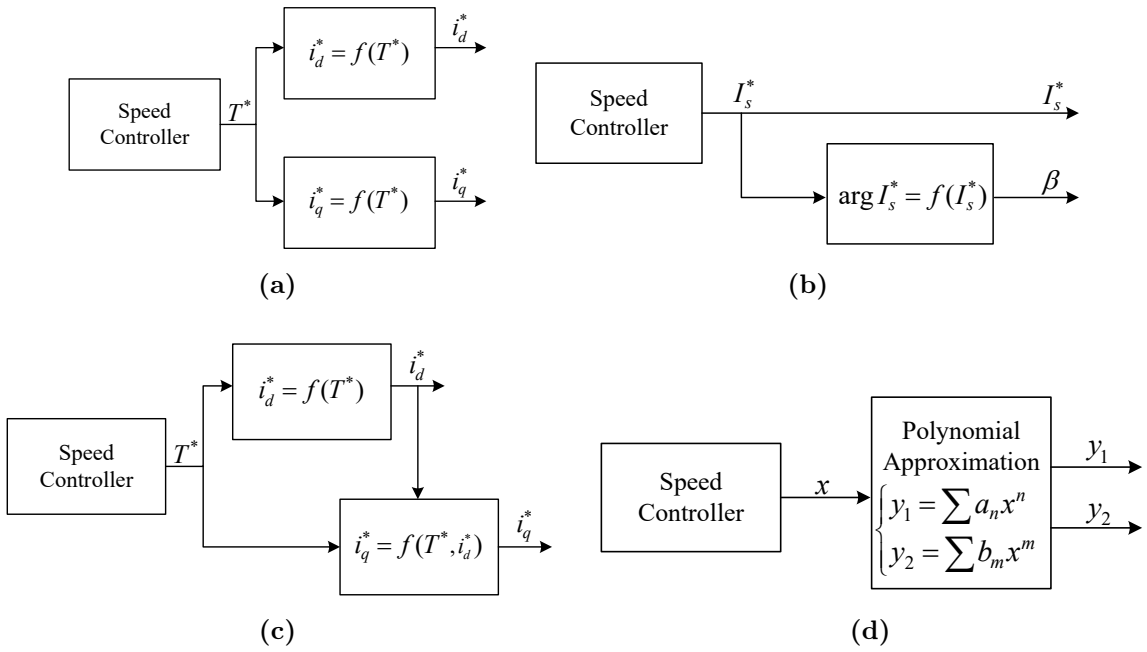

Figure 2.13: Different implementation of MTPA technique (a) reference torque as input (b) reference current as input (c) reference torque as input (d) polynomial approximation based solution.

2.3.3 Constant Power Speed Range (CPSR).

Let U_s stand for the maximum voltage's magnitude. The voltage limit is then explained by

$$U_d^2 + U_q^2 \leq U_s^2 \tag{2.42}$$

By lowering the Ohmic voltage so that Eq. 2.31 and Eq. 2.32 yield a simplified steady state IPMSM model.

$$U_d = -\Omega_{me} L_q I_q \tag{2.43}$$

$$U_q = \Omega_{me} L_d I_d + \Omega_{me} \Lambda_{mg} \tag{2.44}$$

From Eq. 2.42, it follows that

$$L_d^2 (I_d + \frac{\Lambda_{mg}}{L_d})^2 + L_q^2 I_q^2 \leq \frac{U_s^2}{\Omega_{me}^2} \tag{2.45}$$

It is an ellipse equation. Keep in mind that the major and minor axes are dependent on speed. The primary axis is horizontal since $L_d < L_q$. It is clear from Eq. 2.45 that as the speed increases, the ellipses shrinks to $(\frac{-\Lambda_{mg}}{L_d}, 0)$, as seen in Fig. 2.14, the current limit, however, is a fixed circle:

$$I_d^2 + I_q^2 \leq I_s^2 \tag{2.46}$$

At the point where an ellipse and a circle intersect, a feasible maximum power solution

is established. The torque-speed curve and current contour are shown in Fig. 2.15. The

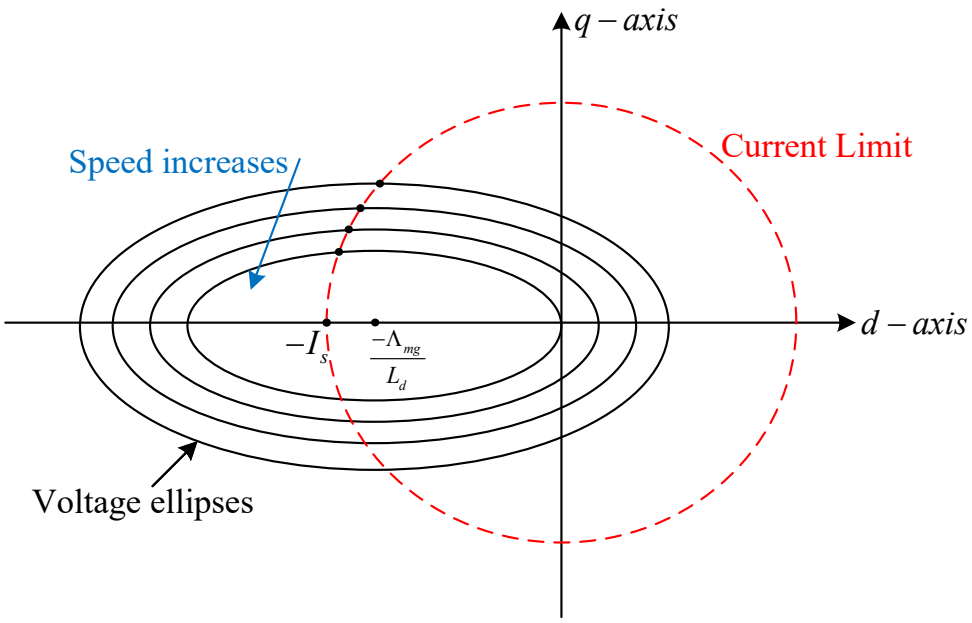

Figure 2.14: Voltage ellipses and current limit.

terminal voltage reaches its maximum with a rated inverter voltage at the base speed, also known as the rated speed. On the current limit circle, the rated condition is indicated by the letter A. The voltage limit decreases as speed rises further. The maximum power solution then descends to the circle's horizontal axis. As a result, the solution with the highest possible power goes closer to the circle's horizontal axis at high speed.

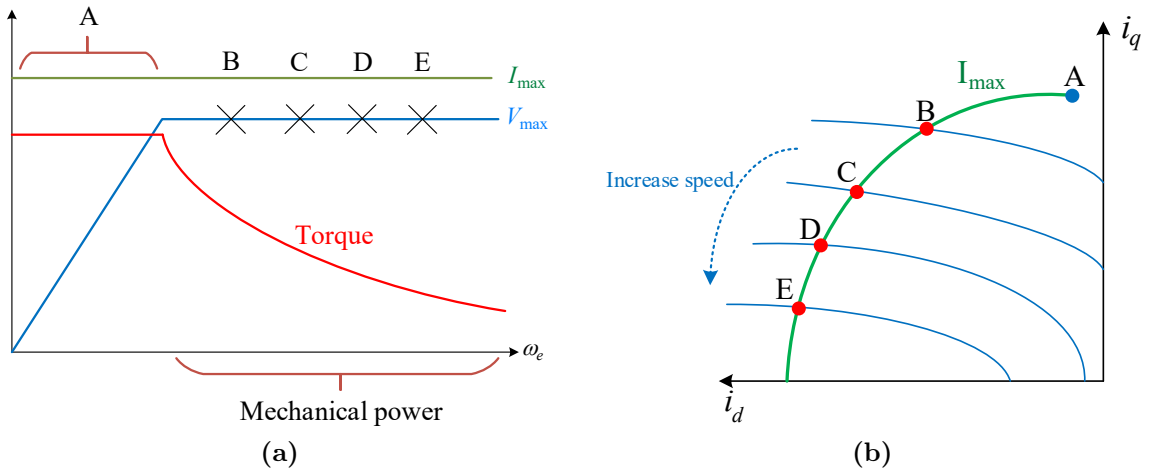

Figure 2.15: (a) Speed vs torque, current and voltage (b) current trajectory in dq plane.

When the speed is increased, the operations at points B, C, D, and E occur in the order shown in Fig. 4.4. In order to satisfy the voltage requirement, a bigger current along the $d-$axis, in the negative direction, must be provided. $\omega_{me}L_d i_d$, in particular, counteracts the increasing back EMF, $\omega_{me}\Lambda_{mg}$, and a larger i_d (in the negative direction) is achieved at

the expense of decreasing the $q-$axis current. Since both the voltage and the current are held at the same value, the intersections that are shown in Fig. 2.15b belong to the contour of constant (apparent) power, which is denoted by the equation $P_e = U_s I_s$. If there is a relatively small amount of loss, the majority of the electrical power will be transformed into the mechanical power $P_m = T_e \omega_{me}$. In the event that the power factor is very close to one, the contour $\overline{BE}$ will be used to characterize the Constant Power Speed Range (CPSR). Since i_q approaches zero as ω_{me} increases, based on the Eq. 2.45 the Eq. 2.47 can be obtained.

$$(i_d + \Lambda_{mg})^2 \leq \frac{U_s^2}{(L_q \omega_{me})^2} \tag{2.47}$$

When ω_{me} is increased sufficiently large, the right hand side of Eq. 2.47 disappears. As a result, it ought to be obvious that $i_d \to -\frac{\Lambda_{mg}}{L_d}$ as $\omega_{me} \to \infty$. As was observed in [74], the requirements that are met will determine whether or not one is capable of producing power at an unlimited speed. the ability of producing power at infinite speed is determined by the criteria.

$$\Lambda_{mg} \leq L_d I_s \tag{2.48}$$

This indicates that in order to prolong the speed range indefinitely, the demagnetizing flux, denoted by $L_d I_s$ and produced by the stator coil, must be greater than the PM flux, denoted by Λ_{mg}. The voltage limits, current limitation, and power plots vs speed are displayed for three different situations in Fig. 2.16. The following is a condensed summary of the specific illustrations for each of the three cases: [32] a) $\Lambda_{mg} > L_d I_s$: This refers to the situation in which the rotor flux exceeds the maximum d-axis flux that the stator current can provide. If the machine operates at the current limit, the apparent power remains constant, while available torque decreases with speed. Because the ellipse's center, $-\frac{\Lambda_{mg}}{L_d}$, is outside the current limit, no more intersections will occur above the critical speed (where $I_q = 0$ and thus torque is null), given by

$$\omega_{critical} = \frac{U_s}{\Lambda_{mg} - L_d I_s} \tag{2.49}$$

b) $\Lambda_{mg} = L_d I_s$: This is the situation in which $\frac{\Lambda_{mg}}{L_d} = I_s$. Because the center of the ellipse is located on the current limit circle, there is always an intersection for any value of that is arbitrarily large ω_{me}. Therefore, the theory suggests that the constant maximum power can be extended to the infinite speed. This means that in theory, the constant maximum power can be applied to an unlimited speed.

c) $\Lambda_{mg} < L_d I_s$: The constant power range will also be increased to an unlimited speed. However, the output power is reduced after peaking. This is the most common design setting.

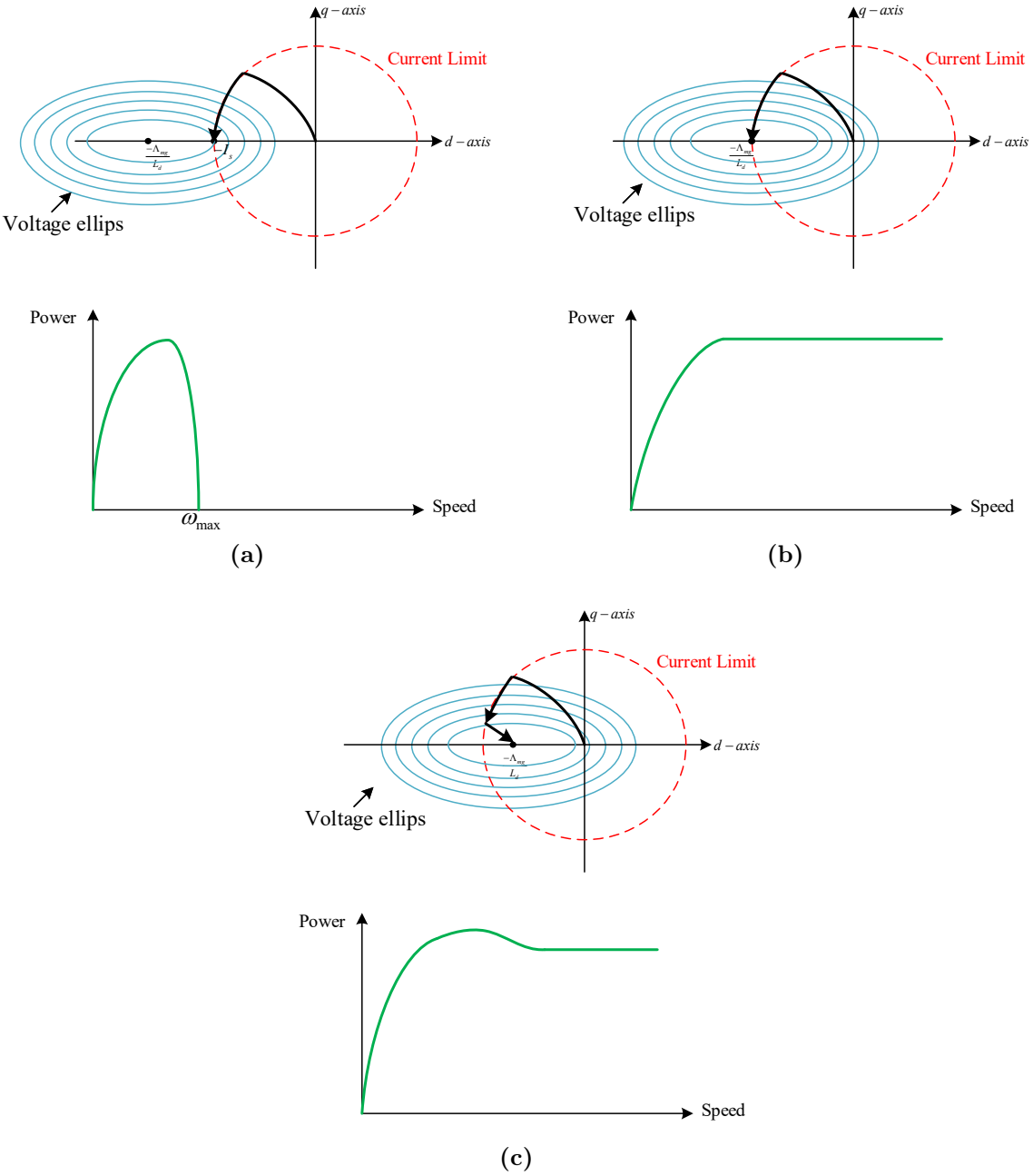

Figure 2.16: The voltage limits, current limitation, and power plots vs speed for (a) $\Lambda_{mg} > L_d I_s$ (b) $\Lambda_{mg} = L_d I_s$ (c) $\Lambda_{mg} < L_d I_s$

.

Chapter 3

Online Methods for Maximum Power Point Tracking (MTPA)

In recent years, new approaches for estimating the maximum torque per ampere (MTPA) have been introduced with the use of specific signals. The main idea behind these techniques is to vary the operating point around its steady-state value and observe how the variable of interest (torque or current) changes in response, in order to find a minimum or maximum. This is known as the ESC approach [20].
One technique, known as MTPA tracking, involves varying the current phase angle while observing either the current magnitude or the torque variations. To extract the MTPA tracking error, speed oscillations are analyzed [21], but this requires relatively high-performance speed sensing, which limits its applicability. An alternative approach has been proposed that detects active power oscillations based on voltage and current signals [22] [23]. In this approach, the current magnitude is observed while assuming that the speed regulator keeps the produced torque equal to the load, despite the current angle variation. Another technique, known as Virtual Signal Injection (VSI) [28], [29], [30], has been introduced to overcome the limitations of Real Signal Injection (RSI). VSI uses a parameter-estimation technique to obtain an MTPA correction signal, instead of directly measuring torque or speed oscillations. VSI is based on the analytical model of the machine and some of the parameters needed for its calculation are estimated based on the actual voltage and current measurements. VSI is not actually estimating the MTPA condition of the actual machine, but can be considered as a way to enhance the simplest MTPA methods with information retrieved online. However, the accuracy of VSI is limited by the knowledge of some machine parameters and the approximations that need to be introduced.
In this chapter, a direct comparison between RSI and VSI is performed, considering the accuracy and performance of both techniques. An analytical description of the tracking errors in the VSI case is reported, including a strategy for compensating the steady-state errors arising from non-linear flux maps. An effective analytical model of the machine inductance is embedded in the analysis of the tracking loop, allowing for improved tracking accuracy, even with low-resolution knowledge of the machine flux maps. To further improve accuracy,

a look-up table (LUT) of the d-axis apparent inductance is used in both RSI and VSI, and the results are compared to conventional RSI and VSI [75].

3.1 Real Signal Injection

Real signal injection MTPA tracking is based on the evaluation of the actual machine torque oscillation due to a high-frequency current injection, allowing the closed-loop correction of the current space vector angle towards the MTPA condition. Different approaches have been proposed in past literature based on this main concept, [26], [23], [27]. The implementation of this class of methods introduces strong constraints on the accuracy and dynamics of the speed measurement affecting the overall performance of MTPA tracking, e.g. [27].
Tracking the MTPA trajectory is an optimization problem. Considering the constant torque of the machine T_{ref}, The minimization of the current $|I_s(\gamma)|$ is a function of current vector angle γ_{MTPA}:

$$\min_{\gamma} |i_s(\gamma)| \text{ subject to } T(|I_s|, \gamma) = T_{ref} \tag{3.1}$$

To obtain the minimum point for a vector angle value the following condition should be satisfied:

$$\frac{dI_s}{d_\gamma}(\gamma_{MTPA}) = 0 \tag{3.2}$$

A high-frequency signal is injected to get the response of the derivative. That the results give the modified proper vector angle signal. Fig. 3.1 illustrate the MTPA tracking loop block diagram. By the sum of the MTPA tracking loop output and high sinusoidal frequency signal δ_γ (with frequency f_i and amplitude A) the reference angle of current vector γ^* is calculated.

$$\gamma^* = \gamma_0 + \delta_\gamma = \gamma_0 + Asin(2\pi f_i t) \tag{3.3}$$

The frequency of the injected signal should be less than the bandwidth of the current control. The amplitude and vector angle of the actual current is assumed to be equal to the reference values ($\gamma = \gamma^*$ and $I_s = I_s^*$). In order to reject the disturbance created by the injected current phase angle oscillation, the speed regulator will generate a variation in current amplitude.

$$I_s(\gamma_0 + \delta_\gamma) = I_s(\gamma_0) + \delta I_s = I_{s_0} + \delta I_s \tag{3.4}$$

where I_{s_0} and γ_0 are the equilibrium points. Using the results of the small signal behavior analysis, a block diagram similar to the one in Fig. 3.1 can be obtained. The linearized transfer function is determined as follows:

$$W(s) = \frac{\delta i_s(s)}{\delta \gamma(s)} = -\frac{\partial T_e}{\partial \gamma} \frac{C(s)P(s)}{1 - (-C(s)P(s))\frac{\partial T_e}{\partial i_s}} \tag{3.5}$$

where the $C(s)$ and $P(s)$ functions refer to the speed controller and the mechanical load plant transfer functions, respectively. The solution to Eq. 3.5 can be broken down into two

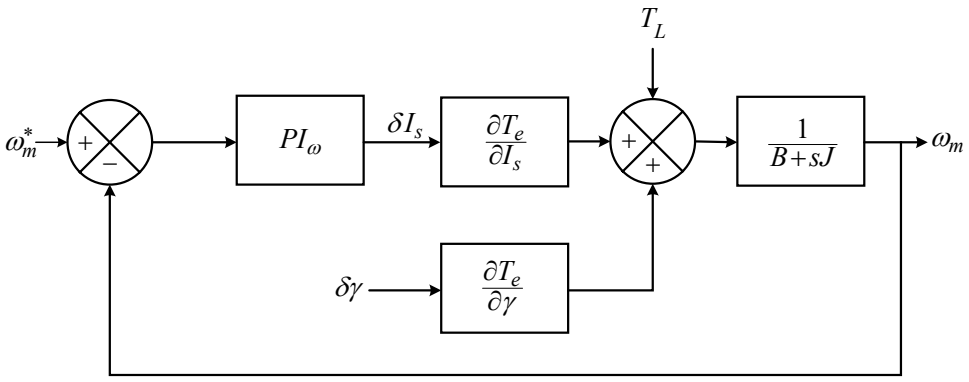

Figure 3.1: Small-signal linearized equivalent model of the speed control loop.

parts: the static gain, and the dynamical part. In this case, it is the closed-loop speed response transfer function.

$$\Omega_{loop}(s) = \frac{C(s)P(s)\frac{\partial T_e}{\partial i_s}}{1 + C(s)P(s)\frac{\partial T_e}{\partial i_s}} \tag{3.6}$$

The following equivalency is valid only if the system is operating under conditions of constant torque:

$$dT_e = \frac{\partial T_e}{\partial i_s} di_s + \frac{\partial T_e}{\partial \gamma} d\gamma = 0 \Rightarrow \frac{\partial T_e}{\partial \gamma} = \frac{\partial i_s}{\partial \gamma}\frac{\partial T_e}{\partial i_s} \tag{3.7}$$

The following equation can be found by substituting the Eq. 3.7 into Eq. 3.5:

$$W(s) = \frac{\partial i_s}{\partial \gamma}\frac{C(s)P(s)\frac{\partial T_e}{\partial i_s}}{1 + C(s)P(s)\frac{\partial T_e}{\partial i_s}} \tag{3.8}$$

The term $\partial i_s/\partial\gamma$ can be derived from derivatives of torque with respect to phase angle and magnitude of current vector correspondingly by using Eq. 3.7. In this manner, the end result is as follows:

$$\frac{\partial i_s}{\partial \gamma} = -\frac{i_s[\Lambda_{mg}\cos\gamma + (L_d - Lq)i_s\cos(2\gamma)]}{\sin\gamma[\Lambda_{mg} + (L_d - L_q)2i_s\cos\gamma]} \tag{3.9}$$

Taking into consideration the time domain, the current vector magnitude oscillation δi_s is rewritten as follows, based on the following considerations:

$$\delta i_s(t) = \frac{\partial i_s}{\partial \gamma}|\Omega_{loop}(j2\pi f_p)|A\sin(2\pi f_p t + \angle\{\Omega_{loop}(j2\pi f_p)\}) \tag{3.10}$$

where $|\Omega_{loop}(j2\pi f_p)|$ and $\angle\{\Omega_{loop}(j2\pi f_p)\}$ represent the magnitude and phase, respectively, of the closed-loop speed control transfer function $W(s)$ computed at the injection frequency. One needs to filter and demodulate the detected disturbance to get a continuous signal. Fig. 3.2 depicts a scheme for MTPA tracking, which involves applying a high pass filter to the perturbed signal and then multiplying the filtered signal by the perturbation to obtain the demodulated signal.

To ensure that both signals have the same phase shift, it is important to notice that the

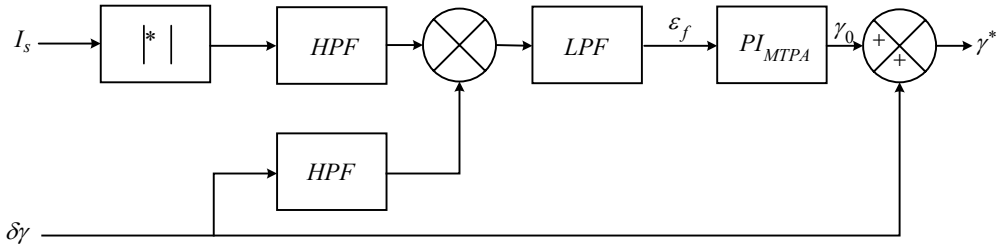

Figure 3.2: MTPA tracking loop block diagram.

perturbation itself is filtered. Second-order terms at higher harmonics are suppressed by filtering the demodulated signal with a Low Pass Filter (LPF). The error signal ϵ_f as obtained can be expressed as:

$$\epsilon_f = LPF\{\delta i_s * \delta\gamma\} \approx \frac{1}{2} k_{HPF}^2(j2\pi f_p)\Re\{\Omega_{loop}(j2\pi f_p)\}A^2\frac{di_s}{d\gamma} \tag{3.11}$$

where $\Re\{\Omega_{loop}(j2\pi f_p)\}$ is the real part of the speed regulation transfer function calculated at injection frequency.
Now the phase angle of the current vector can be corrected by feeding the erroneous signal into a Proportional Integral (PI) regulator. Some factors should be considered to make sure about the correct result.

3.1.1 Stability Analysis

This algorithm's stability needs to be thought out. Gains of PI regulators must be selected sensibly, first and foremost, to guarantee adequate stability and a good convergence rate. The Lyapunov stability requirement provides a useful analytical framework for assessing robustness.

$$V(t) = \frac{1}{2}\epsilon_f^2(t) \tag{3.12}$$

considering a fully integral tracking regulator such as:

$$\frac{d\gamma}{dt} = -\epsilon_f K_{i_{MTPA}} \tag{3.13}$$

Lyapunov derivative is obtained as

$$\frac{dV}{dt} = \frac{dV}{d\epsilon_f}\frac{d\epsilon_f}{d\gamma}\frac{d\gamma}{dt} = K_{i_{MTPA}}\epsilon_f^2\frac{d\epsilon_f}{d\gamma} < 0 \tag{3.14}$$

For a variety of operating situations, the following inequality must hold true before stability is achieved:

$$\frac{d\epsilon_f}{d\gamma} = \frac{d}{d\gamma}\left(\frac{1}{2}A^2\frac{di_s}{d\gamma}k_{HPF}^2(j2\pi f_p)\Re\{\Omega_{loop}(j2\pi f_p)\}\right) > 0 \tag{3.15}$$

Eq. 3.15 cannot be solved analytically because of its complexity. In actuality, its computation involves various physical parameters and speed regulator gains. Inaccurate measurements of these parameters can lead to incorrect calculations. On the other hand, the closed-loop speed transfer function can be analyzed in a number of efficient ways.
First, certain considerations might be addressed regarding the High Pass Filter (HPF). Since the component around the injected frequency must pass through the filter undisturbed, the filter pole must be located at a lower frequency than the injection frequency ($f_{HPF} << f_p$). Thus, the term $k_{HPF}^2(j2\pi f_p)$ can be approximated to unity as follows:

$$\frac{d\epsilon_f}{d\gamma} = \frac{d}{d\gamma}\left(\frac{1}{2}A^2\frac{di_s}{d\gamma}\Re\{\Omega_{loop}(j2\pi f_p)\}\right) > 0 \tag{3.16}$$

The closed-loop speed control response can be almost unity if the injection frequency is selected so that it is well within the speed control bandwidth:

$$\Omega_{loop}(j2\pi f_p) \approx 1 \tag{3.17}$$

In accordance with the previous two conditions, the error signal ϵ_f possesses the maximum strength of the usable signal for a given injection amplitude. Taking these approximations into consideration, the Eq. 3.11 can be rewritten as follows:

$$\epsilon_f \approx \frac{1}{2}A^2\frac{di_s}{d\gamma} \tag{3.18}$$

the stability condition of Eq .3.15 is obtained as follow:

$$\frac{d\epsilon_f}{d\gamma} = \frac{1}{2}A^2\frac{d^2i_s}{d\gamma^2} > 0 \tag{3.19}$$

Eq .3.14 is confirmed for the range of angles being investigated because it can be shown that the derivative $d^2i_s/d\gamma^2$ is positive for any $\gamma \in [\pi/2, \pi]$.

3.1.2 Gain design and adaptation

The transfer function Eq. 3.8 is made up of two terms, as was already stated at the beginning of this section: a gain and a dynamical component (Eq. 3.9) that is equivalent to the speed control regulator. The gain component depends on the operating point, as is evident. This indicates that there are various transfer functions with various cut-off frequencies depending on the operating point. Varying cut-off frequencies result in different time constants in the time domain, which means that the operating point determines how long it takes to reach steady state. A method to linearize loop dynamics is presented in [3]. The approach is based on small-signal gain normalization with local linearization. Let's look at the non-linear tracking loop representation in Fig. 3.3. The plant's small-signal equivalent model is as follows:

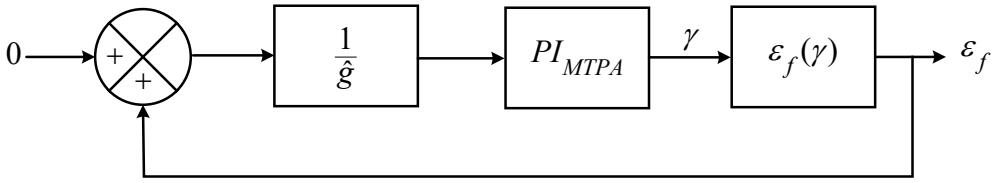

Figure 3.3: Equivalent schematic for the derivative-based normalization.

$$g = \frac{d\epsilon_f}{d\gamma} \tag{3.20}$$

Dividing the error signal by an estimated $\hat{g} \approx g$ of the gain, the loop dynamic can be made normalized. By use Eq. 3.9, the estimate can be derived as in Eq. 3.19. As a result, the system in Fig. 3.3 becomes linear and the dynamics of the tracking loop is no longer dependent on the operational point. In the vicinity of any steady-state operating point, the system obtains the behavior of a first-order low-pass filter. By examining the derivative of the Lyapunov candidate function Eq. 3.12, which becomes as follows in the case of accurate gain normalization, the stability can be examined:

$$\frac{dV}{dt} = K_{i_{MTPA}} \epsilon_f^2 < 0 \tag{3.21}$$

Analytical tracking regulator design is now simple because the model has been linearized using a method called gain normalization. As an integrator, the open-loop transfer function's cross-over frequency is equal to the integral gain and also relates to the closed-loop bandwidth.

$$K_{i_{MTPA}} = 2\pi BW_{MTPA} \tag{3.22}$$

According to earlier assumptions, the tracking bandwidth BW_{MTPA} is the only design requirement and must be upper bound by the injection frequency, which itself must be suitably lower than speed control bandwidth.

3.2 Virtual Signal Injection (VSI)

VSI allows to find out the MTPA condition of the analytical model of the machine, i.e. to solve an on-line analytical optimization problem, where the system response to the injected signal is obtained by the analytical model of the average torque of the machine and some of the parameters needed for its calculation are estimated starting from actual voltage and current measurements. As no injection is done on the actual machine, the main advantage of this method is related to the theoretical infinite tracking bandwidth, being related to the frequency of the virtually injected signal, that could be theoretically increased up to the Nyquist limitation. As in RSI case, the perturbation amplitude has to be kept small, so to reduce second order effects during the demodulation process.

The initial proposal is reported in [28], whilst in [29] the same authors provide an explanation of some wrong approximations adopted in the first proposal and a new expression of the torque aiming at improving the overall accuracy. Hereafter a full analytical development is reported, aiming at highlighting the general concept behind this approach and the required approximations that are needed to be introduced allowing a real implementation in an actual drives system, where magnetic saturation is normally present and machine parameters cannot be considered constant terms.

In steady state condition the power equation can be written as Eq. 3.23. In addition the average electromagnetic torque (lack of iron loss) equation can be obatined as Eq. 3.24.

$$P_m = \frac{3}{2}[(v_d - Ri_d)i_d + (v_q - Ri_q)i_q] = \frac{3}{2}\left[(v_q - Ri_q) + \frac{(v_d - Ri_d)}{i_q}i_d\right]i_q \tag{3.23}$$

$$\frac{P_m}{\omega_m} = T_e = \frac{3}{2}p_p[\Lambda_{mg} + (L_d - L_q)i_d]i_q \tag{3.24}$$

To calculate the high-frequency component of the $d-$ and $q-$axis currents, we use Eq. 3.26 and Eq. 3.27, respectively, when a high-frequency sinusoidal signal is injected into the stator current angle.

$$\Delta\beta = Asin(w_h t) \tag{3.25}$$

$$i_d^h = -I_s sin(\beta + \Delta\beta) \tag{3.26}$$

$$i_q^h = I_s cos(\beta + \Delta\beta) \tag{3.27}$$

From Eq. 3.23 the following equation is obtained:

$$\frac{P_m}{w_m} = T_e = \frac{3}{2}\left[\frac{(v_q - Ri_q)}{\omega_e} + \frac{(v_d - Ri_d)}{i_q\omega_e}i_d\right]i_q \tag{3.28}$$

Obviously, the operation condition effect the $(v_q - Ri_q)/\omega_e$ and $(v_d - Ri_d)/(i_q\omega_e)$ during injecting the high-frequency signal $\Delta\beta$ can be considered as constant values. Also, The parameters in Eq. 3.24 can be considered constant during injecting small sinusoidal signal (they vary respect to the $d-$ and $-q$ axis currents and temperature). A polynomial function (Eq. 3.29) can be used to approximate the relationship between torque and $d-$ and $q-$axis currents. This is possible because the alignment torque component and the reluctance torque component both contribute to the torque. The difference in the $d-$ and $q-$axis inductances is the cause of this difference.

$$T_e^h = \frac{3}{2}\left[\frac{(v_q - Ri_q)}{\omega_e} + \frac{(v_d - Ri_d)}{i_q\omega_e}i_d^h\right]i_q^h \tag{3.29}$$

as it explained Eq. 3.29 is an approximated polynomial function, there is error during injecting the high-frequency signal which the analyze is going to be described in the next sections.

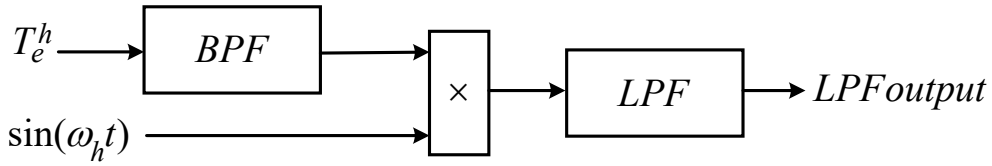

Figure 3.4: Schematic of signal processing block to extract.

As it can be seen the perturbed torque can be obtained by motor velocity, the i_d and i_q that perturbed by high-frequency signal and the $d-$ and $q-$axis voltages. In this case it does not need to inject a real signal to the stator current and perturb the torque.

3.2.1 Signal Processing for VSI

Eq. 3.29 can be expanded by Taylor's series:

$$T_e^h = T_e(\beta) + \frac{\partial T_e}{\partial \beta} A sin(\omega_h t) + \frac{1}{2}\frac{\partial}{\partial \beta}\left(\frac{\partial T_e}{\partial \beta}\right) A^2 sin^2(\omega_h t) + ... \tag{3.30}$$

The MTPA operation point can be demonstrated by the partial derivative of torque to the current angle $\partial T_e/\partial\beta$. As it illustrated in Fig. 3.4 the operation point of MTPA is extracted by a signal processing. The LPF is the proportional to $\partial T_e/\partial\beta$. In addition it should be mentioned again that the cut-off frequency of the filter should be lower than virtual perturbation signal ω_h.
Based on the equality of the Eq. 3.29 and Eq. 3.30 the torque can be obtained by following parameters.

- $d-$ and $q-$axis voltages, v_d and v_q,
- measured speed of the motor ω_e,
- $d-$ and $q-$axis currents, i_d and i_q,
- the perturbed $d-$ and $q-$axis currents produced by injecting signal ,i_d^h and i_q^h

As it illustrated in Fig. 3.4 the signal is processing by a Band Pass Filter (BPF), the center frequency of the filter is equal to the injected high-frequency signal. Then, according to the Eq. 3.30 the output signal of the BPF is the proportional item to the first order of the equation.
As a result, the following equation is obtained:

$$K\frac{\partial T_e}{\partial \beta} A sin^2(\omega_h t) = K\frac{\partial T_e}{\partial \beta} A\left(\frac{1}{2}[cos(0) - cos(2\omega_h t)]\right) = \frac{1}{2}KA\frac{\partial T_e}{\partial \beta} - \frac{\partial T_e}{\partial \beta} KAcos(2\omega_h t) \tag{3.31}$$

where K represents the gain of the BPF at the frequency where the signal is being injected. A first order order LPF will be applied to the right hand side of Eq. 3.30. The cut-off frequency of this filter will be lower than the frequency of the virtual perturbation signal.

The $\partial T_e/\partial\beta$ data can be retrieved in this method. Since the MTPA current angle is equal to the current angle, the LPF's output is effectively zero in this case. The integrator will use this state to produce the $d-$axis current reference necessary for MTPA functioning.

3.2.2 Square-Wave Injection

Different signal waves can be injected into the motor model, just as there is no actual signal injection into the motor. In this situation, it is possible to inject a square-wave signal, which has several benefits that are addressed in this section. It should be underlined that everything that has been thought about and assumed is still true in this situation because the operation point is still can be tracked.
Let's have a look at how the phase angle of the current vector is affected by the perturbation. Taking into account a square-wave perturbation with an amplitude of A and a period of T_s, the equation can be stated as follows:

$$\beta^* = \beta + \Delta\beta \text{ where } \Delta\beta = \begin{cases} A, & \text{when } nT_s \leq t \leq \left(n + \frac{1}{2}\right)T_s \\ -A, & \text{when } \left(n + \frac{1}{2}\right)T_s \leq t \leq (n+1)T_s \end{cases} \tag{3.32}$$

The perturbed torque due to the injected square-wave can be expanded by Taylor's series. The following equation illustrate the expression:

$$T_e^h(\Delta\beta) = T_e(0) + \Delta\beta \cdot \frac{\partial T_e^h}{\partial\beta}\bigg|_{\Delta\beta=0} + \frac{1}{2}\Delta\beta^2 \cdot \frac{\partial^2 T_e^h}{\partial^2\beta}\bigg|_{\Delta\beta=0} + \cdots \tag{3.33}$$

By selecting a small value for $\Delta\beta$, the second order terms does not need to be considered:

$$T_e^h \approx T_e + \Delta\beta\frac{\partial T_e}{\partial\beta} \tag{3.34}$$

Eq. 3.34 can rewritten as follow:

$$T_e^h - T_e \approx \Delta\beta\frac{\partial T_e}{\partial\beta} \tag{3.35}$$

Hereafter, the method depicted in Fig. 3.5 is used to demodulate the Eq. 3.35. When using a square wave, a BPF is unnecessary, as can be seen by comparing Fig. 3.4 and 3.5. When the system's overall bandwidth is raised in this way, settling time is decreased.
The signal error that comes out from the demodulator has the following form:

$$\epsilon_f = |A|\frac{dT_e}{d\beta} = sign(\Delta\beta)(T_e^h - T_e) \tag{3.36}$$

As for the other algorithms, signal error ϵ_f can be fed to a PI-regulator.

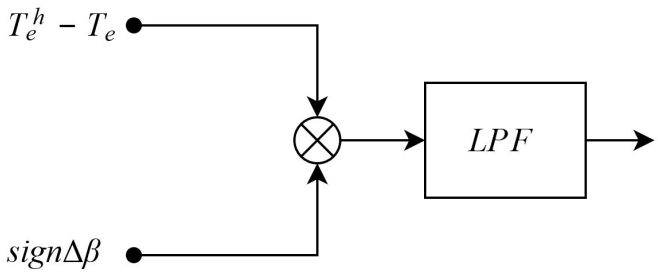

Figure 3.5: Demodulation for square-wave perturbation.

3.2.3 Gain design and adaptation

Another issue with VSI algorithms is that their dynamic performance is operating point dependent. Analyzing static gain is done in a way comparable to RSI. Since the procedure does not include any actual injection or dynamical systems, the problem of gain adaptation for VSI must be tackled mathematically.
The preceding section established that the PI regulator receives an error signal consisting of:

$$\epsilon_f = |A| \frac{\partial T_e}{\partial \beta} \tag{3.37}$$

This is how the error is affected by the angle:

$$\frac{\partial \epsilon_f}{\partial \beta} = |A| \frac{\partial^2 T_e}{\partial \beta^2} \tag{3.38}$$

One interpretation of the last formula is as follows: if we change the angle by a small amount, the resulting change in signal error will be proportional to the second derivative of torque with respect to the angle:

$$\frac{\partial^2 T_e}{\partial \beta^2} = \frac{3}{2} p_p \big(- \Lambda_{mg} I_s \sin(\beta) + 2(L_d - L_q) I_s^2 \sin(2\beta) \big) \tag{3.39}$$

Gain adaption for (3.39) is performed by dividing the error.

3.2.4 Disadvantages of RSI and VSI

In the previous sections, an explanation of two MTPA tracking algorithms operation is presented. But, the issues with the two algorithms have not been discussed. Both algorithms perform well in terms of tracking, but because of their different topologies, they have some issues. A brief comparison of the drawbacks of the two algorithms is presented in this subsection.
For the purpose of rejecting the oscillation of the current vector, an error signal must be generated by the speed control loop. To do this, the speed control loop must be fed with an accurate and reliable speed measurement. The speed sensor must be sensitive enough to detect even the slightest changes in velocity caused by the oscillation of the vector current.

A costly speed sensor is needed to provide a reliable reading. Therefore, the RSI algorithm cannot be used in situations where speed is not directly detected or when less accurate speed sensors are utilized.
The delay in the algorithm's final result is another drawback. In reality, the RSI algorithm's settling time is longer than the VSI algorithm because of the limits that have already been enforced for RSI. The bandwidth of the control loops makes this a challenging problem to handle. Increasing the bandwidth of the control loops is not a good idea because it could make the whole system unstable. However, if a system is provided with an accurate speed sensor, the algorithm provides accurate tracking characteristics.
Non-negligible parameter fluctuations and some false assumptions are made when calculating the torque derivative, both of which have been discovered through literature research of the VSI algorithm. The latter is thoroughly analyzed in [28].
Eq. 3.29 makes some assumptions based on the method described in [28]. It can be seen that the result of multiplying the term by i_d and i_q is equivalent to $L_d - L_q$ and multiplying the term by just i_q results in Λ_{mg}.
It can be observed that the result is actually the derivative of the torque equation multiplied by the amplitude of perturbation, if the computation of $\tilde{T}_e^h - \bar{T}_e$ is performed under the two assumptions provided below (i.e., by substituting the two terms in 3.29 with Λ_{mg} and $(L_d - L_q)$, respectively). These two presumptions, however, are incorrect because the real definitions of the two terms are written in the Eq. 3.40, which may be used to compute $\tilde{T}_e^h - \bar{T}_e$.

$$\begin{aligned} -L_q &= \frac{u_d - Ri_d}{\omega_e i_q} \\ (\Lambda_{mg} + L_d i_d) &= \frac{u_q - Ri_q}{\omega_e} \end{aligned} \tag{3.40}$$

Thus,

$$\tilde{T}_e^h - \bar{T}_e = \Delta\beta \frac{3}{2} p_p \left(\Lambda_{mg} I_s \cos(\gamma) + L_d I_s^2 \cos^2(\gamma) - L_q I_s^2 \cos(2\gamma) \right) \tag{3.41}$$

that Eq. 3.35 claims a different derivative value.
To get the correct derivative data, a new equation for calculating the torque is proposed in [29]. The following is the equation for the new model of the torque.

$$T_e = \frac{3}{2} p_p \left[\left(\frac{u_q - Ri_q}{\omega_e} - L_d i_d \right) + \left(L_d + \frac{u_d - Ri_d}{\omega_e i_q} \right) i_d \right] i_q \tag{3.42}$$

The new form of the voltage equations modified as below.

$$\begin{aligned} (L_d - L_q) &= \frac{u_d - Ri_d}{\omega_e i_q} + L_d \\ \Lambda_{mg} &= \frac{u_q - Ri_q}{\omega_e} - L_d i_d \end{aligned} \tag{3.43}$$

The right answer is achieved by using $T_e^h - T_e$ in this calculation. Observe that the MTPA

curve tracking procedure now calls for two parameters, R and L_d. Due to the negligible variation in these two values during motor operation, they can be considered as constants. Parameter dependence is now examined in detail. Torque calculations at the perturbed point might be problematic because of the non-linear behavior of machine parameters. According to the prior discussion, the current phase angle is to be perturbed by a square wave, indicated by $\Delta\gamma$. The perturbed torque can be expressed as follows using a first order Taylor's approximation:

$$T_e^h = \bar{T}_e + \Delta\gamma \frac{\partial \bar{T}_e}{\partial \gamma} + \mathcal{O}\left(\frac{\partial^2 \bar{T}_e}{\partial \gamma^2}\right) \rightarrow T_e^h - \bar{T}_e \approx \Delta\gamma \frac{\partial \bar{T}_e}{\partial \gamma} \tag{3.44}$$

This means that the derivative of the torque with respect to the same angle is directly proportional to the injected angle perturbation, and therefore the torque variation. Using what you know about the torque derivative, you can force the system's operating point to the MTPA condition. To construct the MTPA tracking loop, the torque variation $T_e^h - T_e$ could be used instead of the torque derivative, necessitating a real-time calculation of that term. The torque written in Eq. 3.42 is a close approximation $\tilde{T}_e^h = T_e^h + e_{\tilde{T}_e^h}$ of the true perturbed torque. The equation can be revised to account for the present dependence of both parameters as follows.

$$T_e^h = \frac{3}{2} p_p i_q^h \left\{ \Lambda_{mg}(i_d^h, i_q^h) + [L_d(i_d^h, i_q^h) - L_q(i_d^h, i_q^h)] i_d^h \right\} \tag{3.45}$$

Because accurate information regarding the machine's parameters at the perturbed operating point is not presently accessible, it is necessary to make use of an estimate of this kind. When the machine voltage equations are taken into account, the following two terms emerge:

$$[L_d(i_d^h, i_q^h) - L_q(i_d^h, i_q^h)] \approx \frac{u_d - R\bar{i}_d}{\omega_e \bar{i}_q} + L_d(\bar{i}_d, \bar{i}_q) \tag{3.46}$$

$$\Lambda_{mg}(i_d^h, i_q^h) \approx \frac{u_q - R\bar{i}_q}{\omega_e} - L_d(\bar{i}_d, \bar{i}_q)\bar{i}_d \tag{3.47}$$

Under the simplification assumptions that current derivatives and parameter fluctuations in the perturbed current operating point are minimal, it can be determined.

$$T_e^h - \bar{T}_e = \left(\tilde{T}_e^h - e_{\tilde{T}_e^h}\right) - \bar{T}_e \tag{3.48}$$

Then, based on the Eq. 3.48

$$\tilde{T}_e^h - \bar{T}_e = \frac{3}{2}\Delta\gamma p_p \left[\Lambda_{mg} I_s \cos(\gamma) + (L_d - L_q) I_s^2 \cos(2\gamma) \right] = \Delta\gamma \frac{\partial T_e}{\partial \gamma} + e_{\tilde{T}_e^h} \tag{3.49}$$

For highly non-linear electric machines like SynRM, the tracking error introduced by the second simplifying assumption above can be quite significant and hence require $e_{\frac{\partial T_e}{\partial \gamma}} = e_{\tilde{T}_e^h}/\Delta\gamma$. Using the polar equation for the torque derivative with respect to the present

angle, the computation of this inaccuracy is relatively simple.

$$\frac{\partial T_e}{\partial \gamma} = \frac{3}{2} p_p \left[\Lambda_{mg} I_s \cos(\gamma) + \left(L_d - L_q\right) I_s^2 \cos(2\gamma) + \frac{\partial \Lambda_{mg}}{\partial \gamma} I_s \cos(\gamma) + \left(\frac{\partial L_d}{\partial \gamma} - \frac{\partial L_q}{\partial \gamma} \right) \frac{I_s^2}{2} \sin(2\gamma) \right] \tag{3.50}$$

Eq. 3.51 is the result of a direct comparison with the $T_e^h - T_e$ expression for the torque variation.

$$e_{\frac{\partial T_e}{\partial \gamma}} = \frac{3}{2} p_p \left[\frac{\partial \Lambda_{mg}}{\partial \gamma} + \frac{\partial L_d}{\partial \gamma} i_d - \frac{\partial L_q}{\partial \gamma} i_d \right] i_q \tag{3.51}$$

It can be shown that the error is proportional to the torque and is related to the non-perturbed current operating point. As will be demonstrated in the following, understanding the machine's flux-maps enables one to compute the derivative terms of Eq. 3.51 and offer a direct correction for VSI tracking inaccuracy. The tracking loop model incorporates a useful analytical representation of the machine inductances to increase tracking precision even when the machine flux maps are known with only modest quantization.
The tracking error for the torque equation in Eq. 3.42 is also analyzed in [29]. Using the same approach used for (3.42), it can be seen that in equation (3.41) there is a term that is proportional to $\cos^2$. By rewriting it as:

$$\cos^2(\gamma) = \cos(2\gamma) + \sin^2(\gamma)$$

The derivative information can be written in this way:

$$T_e^h - \bar{T}_e = \Delta\gamma d 2 p_p \left(\Lambda_{mg} I_s \cos(\gamma) + L_d I_s^2 \cos(2\gamma) - L_q I_s^2 \cos(2\gamma) + L_d I_s^2 \sin^2(\gamma) \right) \tag{3.52}$$

Since the last term is not present in the derivative, the error can be written as:

$$e'_{\frac{\partial T_e}{\partial \gamma}} = d 2 p_p \left[\frac{\partial \Lambda_{mg}}{\partial \gamma} I_s \cos(\gamma) + \frac{\partial L_d}{\partial \gamma} I_s \cos(2\gamma) - \frac{\partial L_q}{\partial \gamma} I_s \cos(\gamma) - L_d I_s^2 \sin^2(\gamma) \right] \tag{3.53}$$

Comparing (3.51) and (3.53), it can be note the in the latter equation a term $-L_d I_s^2 \sin^2(\gamma)$ is added. This means that when the torque increases, also I_s increases meaning that $e'_{\frac{\partial T_e}{\partial \gamma}}$ becomes bigger and higher with respect to $e_{\frac{\partial T_e}{\partial \gamma}}$.

3.3 Using Virtual Signal Injection (VSI) for SynRM

In SynRM there is not any magnet, So, when the rotor spin the torque will be generated by the variation of the reluctance. Thus, the voltage equation can be written as below:

$$u_d = R i_d - \omega_e L_q i_q \tag{3.54}$$

$$u_q = R i_q + \omega_e L_d i_d \tag{3.55}$$

Based on the voltage equation the torque equation is obtained:

$$T_e = \frac{3}{2} p_p i_q i_d (L_d - L_q) \tag{3.56}$$

Based on Eq. 3.54 and Eq. 3.55 the inductances of the machine can be obtained as below:

$$\begin{aligned} -L_q &= \frac{u_d - R i_d}{\omega_e i_q} \\ L_d &= \frac{u_q - R i_q}{\omega_e i_d} \end{aligned} \tag{3.57}$$

By taking into account the VSI torque error, $T_e^h - T_e$, the derivative value can be directly calculated without the contribution of the parameters' change. All process that have explained for IPMSM, for SynRM is valid.

3.4 Results

In this section the experimental and simulation results are shown. The RSI algorithm and the VSI algorithm have been implemented and tested for an IPMSM. Hereafter, simulation and experimental results are compared, in particular, the steady state point in order to verify the accuracy of the two algorithms.

Table. 3.1 illustrate the characteristics of the IPMSM machine. The motor behavior is

Table 3.1: IPMSM Parameters.

Variable	Value
Number of pole pairs (p_p)	2
Base speed (ω_{base})	1480 RPM
Maximum torque	6.5 Nm
DC-link voltage (V_s)	250 V
$d-$axis inductance (L_d)	22 mH
$q-$axis inductance (L_q)	95 mH
Stator resistance (R_s)	3.4 Ohm

simulated with Plecs through flux maps that are measured from the motor. The characteristics of the apparent inductances are the following and they are represented in Fig. 3.6.

A first set of simulations has been carried out to verify the static accuracy of the tracking methods, whose main features. The non-linear analytical model of the SynRM has been considered in the first tests, in order to allow a fair validation and comparison, highlighting any possible difference of the tracking methods on a highly non-linear model, as compared to the one of the IPMSM that will be considered later.

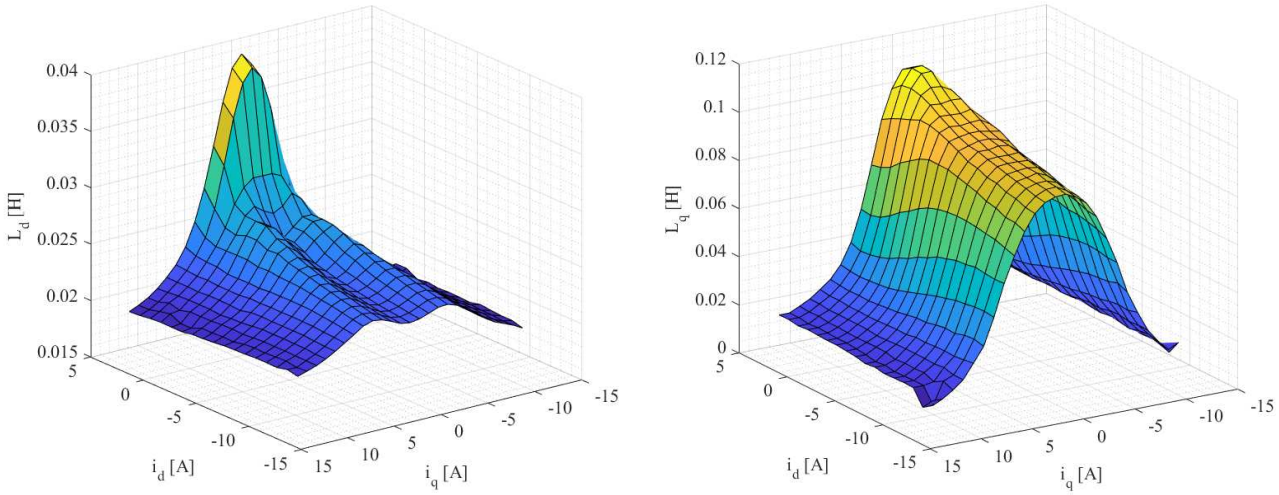

(a) **(b)**

Figure 3.6: $d-$ and $q-$axis inductances maps. (a) $d-$axis inductane (b) $q-$axis inductance.

The results of VSI method is presented based on the Eq. 3.29 is shown by blue cross '×' and Eq. 3.42 that is illustrated by violet circle 'O' in Fig. 3.7. There are two another trajectory that one of them is based on the LUT of flux maps and the other one is a contribution of the LUT of L_d for Eq. 3.29. The green triangle '△' shows the MTPA trajectory based on the LUT of all motor parameters and the red square '□' illustrate the trajectory based on Eq. 3.42 which contributed by the LUT of $d-$axis apparent inductance. As a results, the accuracy of MTPA trajectory using Eq. 3.29 is quite low that by using the right equation (Eq. 3.42), the MTPA trajectory's accuracy is improved. The results still can be better by considering the contribution of the $d-$axis inductance LUT.
Fig. 3.8 illustrate the results of adding a LUT of L_d as a compensator to Eq. 3.29 for VSI algorithm. The black cross '×' present the MTPA trajectory based on Eq. 3.29 that the accuracy is not acceptable. By using the an compenstor (L_d LUT map), the MTPA trajectory's accuracy is improved which is illustrated by black triangle '△'. Fig. 3.9 illustrate the results of using and LUT of L_d to contribute Eq. 3.42 for VSI. The black circle 'O' shows the MTPA trajectory based on Eq. 3.42 that the accuracy is acceptable. But, by using a LUT of L_d to contribute it, the MTPA trajectory is improved which is illustrated by red square '□'.
The test results of Fig. 3.10 aim at validating the effectiveness of the dynamics equalization through gain adaptation. Small-signal disturbance is injected into the error ϵ_f at $t = 8s$ when the system has already reached a steady-state condition for the tracking loop and the error is zero. The test has been carried out at three different level of load torque, namely 0.5, 3 and 6 Nm. In case the gain of the tracking loop is correctly compensated, the error follows a reference first order response independently on the torque operating point. It is also clear how the responses are different when proposed loop compensation is not adopted. The response of the equivalent first-order system to the reaction of the real system has a good match, as seen in Fig. 3.10. Therefore, it can be claimed that the gain is correctly

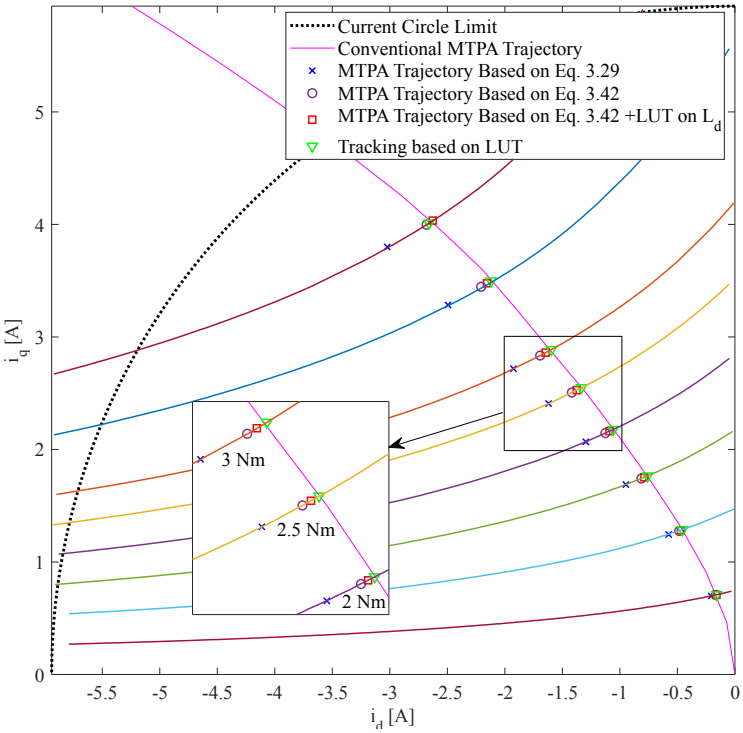

Figure 3.7: Comparison between VSI algorithms.

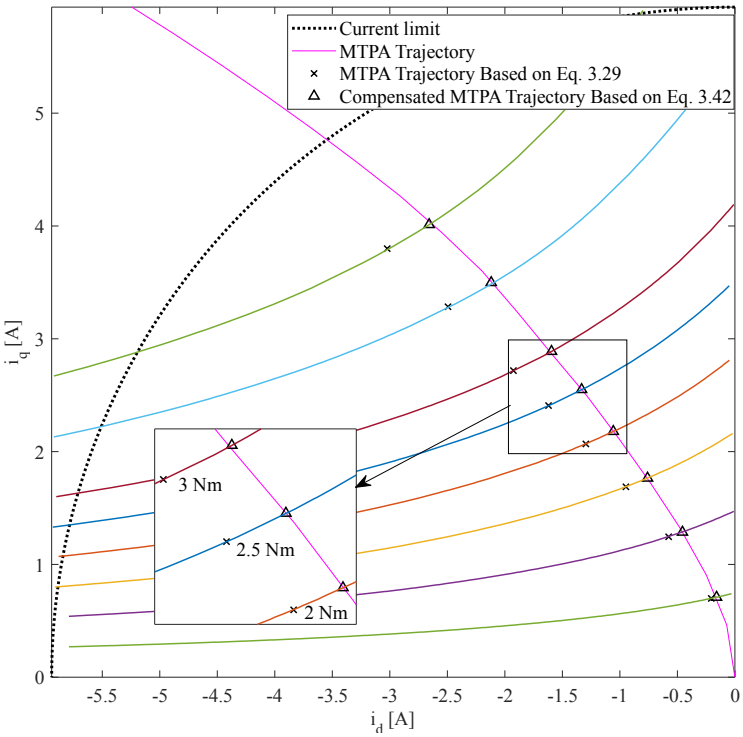

Figure 3.8: Applying compensator to the Eq. 3.29

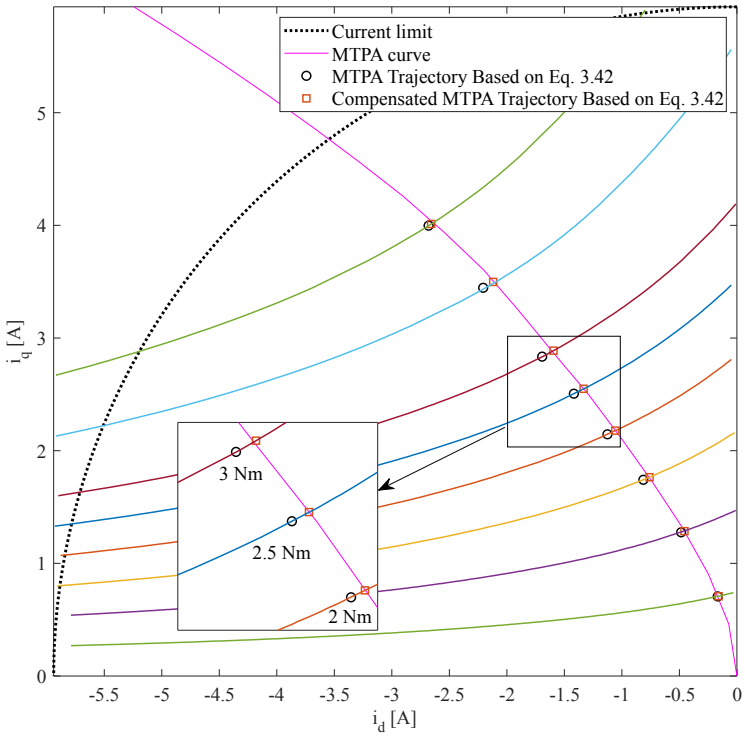

Figure 3.9: Applying compensator to the Eq. 3.42

compensated.
By correcting the gain of the tracking system, the settling time is also improved, especially for low torque loads.

3.4.1 RSI vs VSI for IPMSM

In this subsection a comparison between RSI and VSI is presented in terms of steady-state accuracy. The injection parameters for both method are the same, but the injection frequency is different. The frequency for RSI is 2 Hz and for VSI is 2.5 kHz. Furthermore, the gain compensation is used for both methods. As it can be seen in Fig. 3.11, the red cross '$\times$' shows the VSI methods based on Eq. 3.29 that the accuracy is quite low. The blue asterisk '$*$' presents the VSI methods based on the Eq. 3.42 that in this case the VSI method is improved. The RSI method is illustrated by the black triangle '$\triangle$'. As a results, the RSI method have a higher accuracy than VSI method.

3.4.2 VSI and RSI for SynRM

The procedure of VSI and RSI for SynRM is the same as IPMSM. Just in IPMSM there is the contribution of permanent magnets.
Fig. 3.12 presents the MTPA trajectory based on VSI, RSI and VSI+L_d LUT. The black cross '$\times$' shows the VSI method for this kind of machine. As a results, VSI has a linear behavior and does not tracking the MTPA trajectory due to the constant value of the $d-$ and $-q$ inductances. The RSI method which is illustrated by red triangle '$\triangle$' has a higher

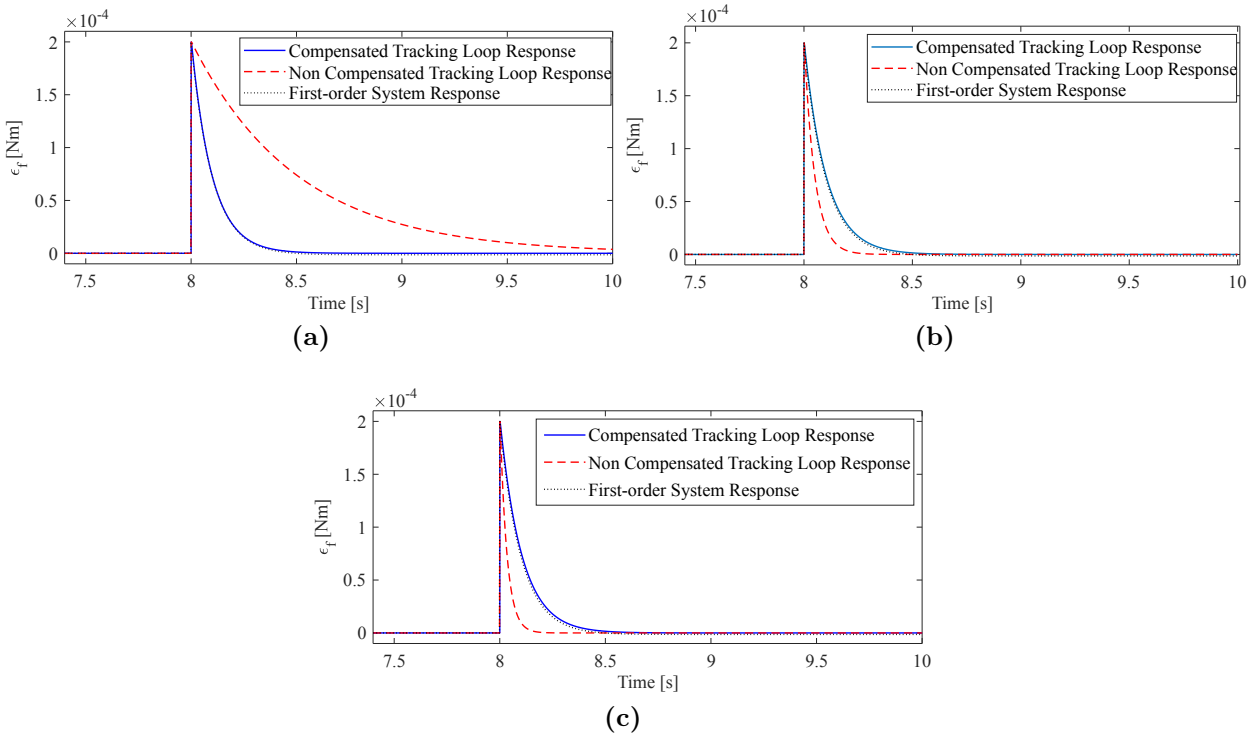

Figure 3.10: Gain compensation results.

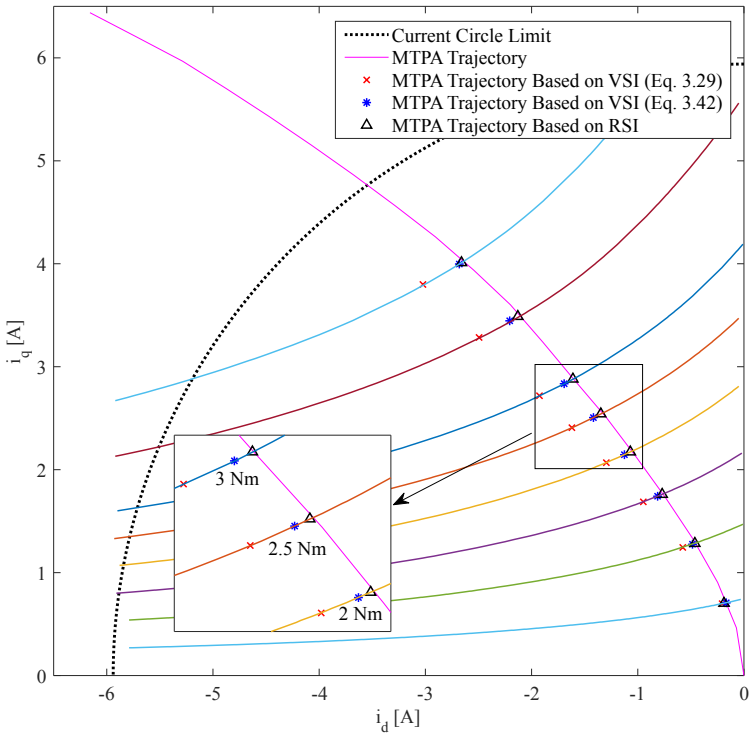

Figure 3.11: Demodulation for square-wave perturbation.

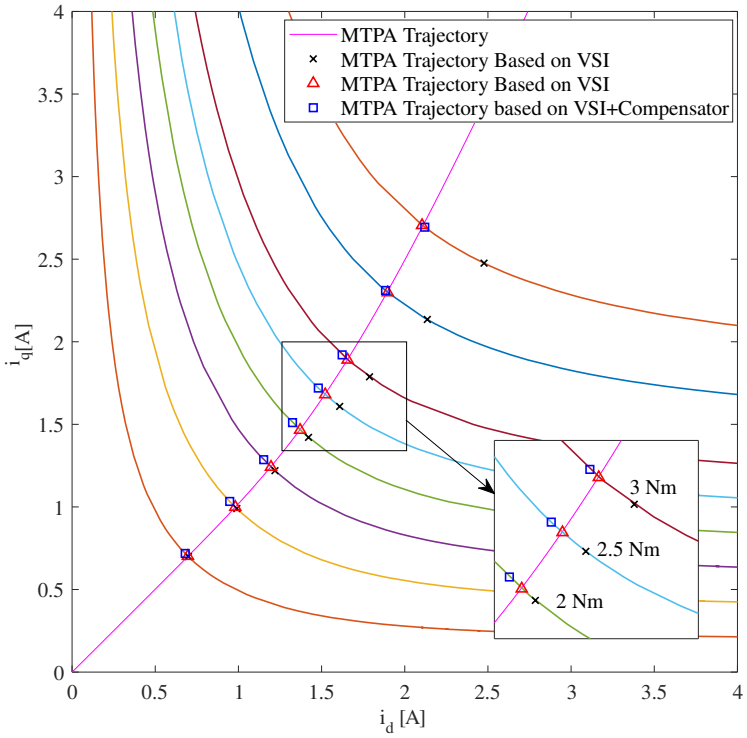

Figure 3.12: MTPA trajectory using RSI and VSI with polynomial approximation of SynRM parameters.

accuracy.

The behavior of VSI algorithm is improved by considering the non-linearity of the flux-linkage maps; a LUT of L_d is added that the results are presented by blue square '□'.

Using a LUT to overcome the non-linear behaviour of the machine parameters costs on memory of the microcontroller. There are some approximation methods to find the nonlinear behaviour of the machine parameters based on the $d-$ and $q-$axis flux-linkage. In [76] a polynomial approximaton is presented that in Chapter. 5 is studied.

The polynomial approximation is used instead of LUT in to compensate the error; the results are presented in Fig. 3.12 (blue square '□'). Based on the results, using polynomial approximation is not accurate as LUT.

3.4.3 Experimental Results

The experimental results are displayed in this subsection. For an IPM motor, the RSI and VSI algorithms have implemented and tested. Fig. 3.13 illustrate the control and power board of the experimental implementation. In order to confirm the accuracy of the two algorithms, simulation and experimental data are compared, focusing in particular to the steady state point.

Two power supply are used to power the drive; the first one provides 24V DC to the control board and the second power source provides 250V DC to the power board. The motor positioned on a test rig, is connected to the control board. An hysteresis brake is attached to the motor shaft to provide a controlled load torque. Using a PC interface and a serial

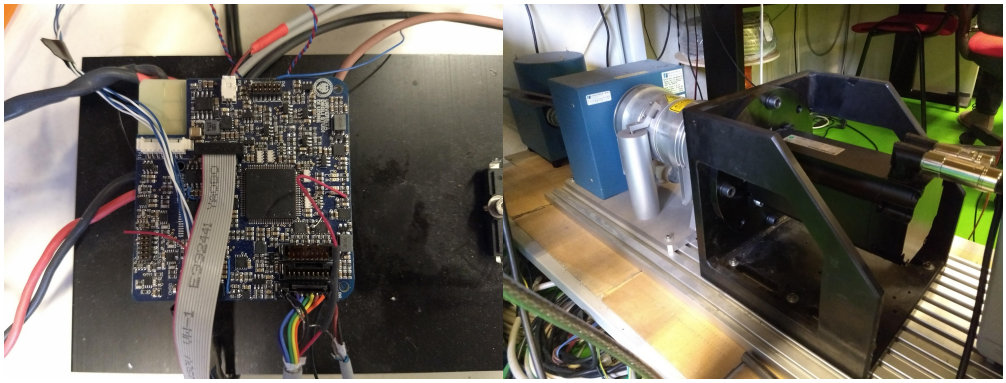

(a) (b)

Figure 3.13: (a) Control board and (b) power board of the experimental test.

port, the load torque can be adjusted.

Fig. 3.14 presents the experimental results using VSI and RSI for IPMSM. The $d-$ and $q-$axis currents are measured in steady state conditions.

The simulation results and experimental MTPA trajectories based on VSI are illustrated by orange cross '×' and blue cross '×' ,respectively. The gray triangle '△' shows the simulation results of the RSI MTPA trajectory and the red triangle '△' is the experimental results of MTPA trajectory based on the RSI.

The RSI method has a better accuracy compare with the VSI algorithm. There are some error between simulation and experimental results that comes from experimental limitations such as noise and the accuracy of the current sensors.

To improve the VSI algorithm results for IPMSM, a LUT of $d-$axis inductance is used and the simulation and experimental results are presented in Fig. 3.15. The blue cross '×' and green circle 'O' illustrate the simulation and experimental results of the MTPA trajectory based on the VSI algorithm, respectively.

The blue triangle '△' shows the simulation results of the MTPA trajectory based on the VSI algorithm with a LUT of $d-$axis inductance. And the experimental results of the MTPA trajectory based on the VSI algorithm with a LUT of $d-$axis inductance is shown by the red square '□'.

By using the LUT of the $d-$axis inductance the accuracy of the MTPA trajectory based on the VSI method is improved.

Like previous results, there are errors between simulation and experimental implementation that as explained it is because of the noise and the experimental limitations.

3.5 Conclusion

A fair evaluation of the accuracy and performance of RSI and VSI and a direct comparison between them is proposed in this chapter. Simulations have been carried out for two types of motors. To avoid possible errors due to interpolation of flux maps and measures inaccu-

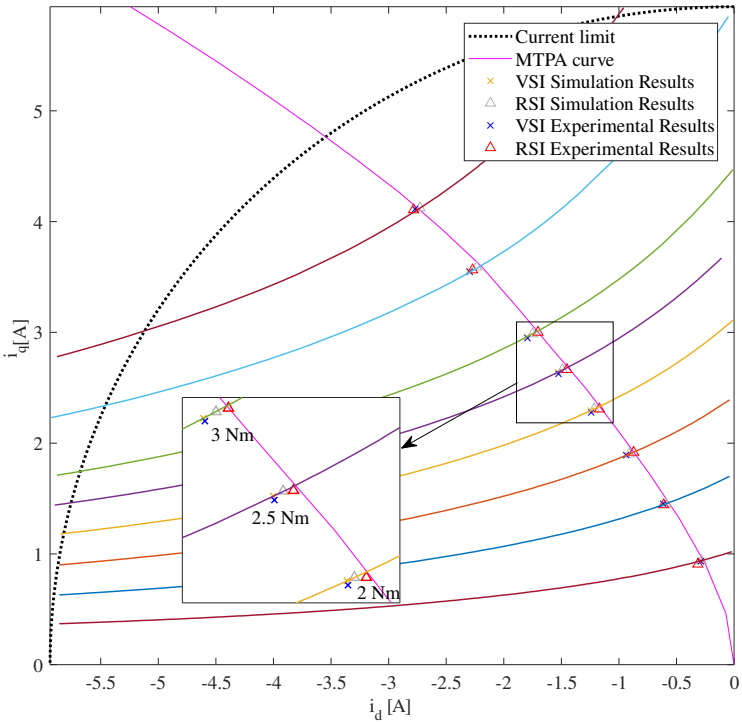

Figure 3.14: Experimental results of VSI and RSI algorithm for IPMSM.

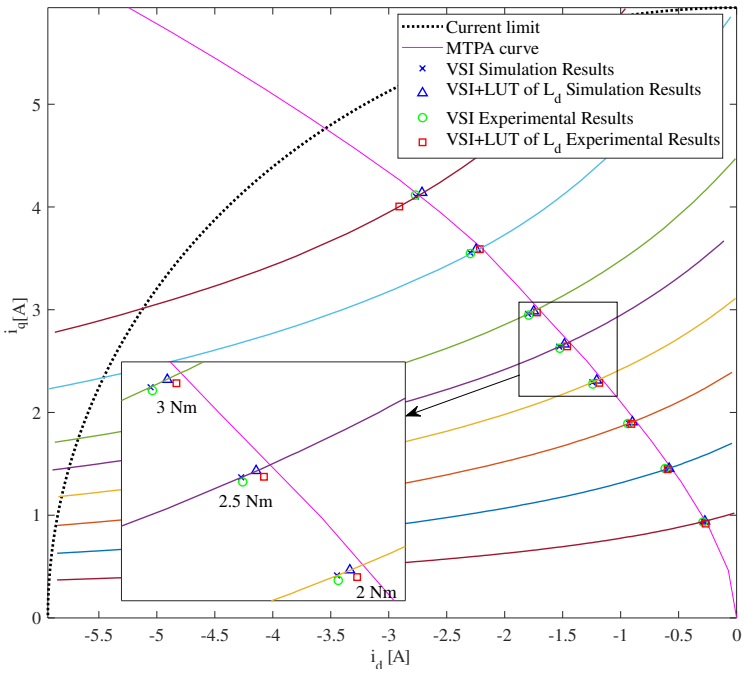

Figure 3.15: Experimental results of VSI and RSI algorithm for IPMSM.

racy, an analytical model of SynRM is developed and used to test the accuracy of the two algorithms. As can be seen from the results, if no compensation for tracking error is applied to VSI algorithm, RSI has better accuracy.
VSI accuracy in estimating the MTPA is affected by the knowledge of some machine parameters and should be considered indeed an estimation method based on the model knowledge, while RSI entirely relies on extremum seeking approach. In the VSI method, the steady-state MTPA error is mainly due to variation of magnetic parameters, which were supposed constant. In order to address this issue, a compensation strategy for the tracking error is introduced, resulting in a substantial improvement of accuracy, allowing to increase the accuracy of this method even in the case the machine flux maps are known with poor resolution. A further improvement is proposed, which allows analytical tuning and adaptation of the tracking loop gains, assuring both stability and the same dynamical performance in the whole machine operating range.
From the dynamical point of view, the model of an IPMSM is used to test the dynamical behavior of the two algorithms. Another test is carried out on a real SynRM to test the accuracy of the two algorithms even when quantization of flux maps is low. Experimental tests have been carried out on the real IPMSM in order to prove simulation results. As can be seen from the results, accuracy of the VSI algorithm is worse with respect to that of RSI, when no L_d LUT contribution is applied. However, since the saliency of the IPMSM is lower with respect to SynRM, the error is relatively small.
As a future work, the RSI and improved VSI can be tested on the Permanent Magnet assisted Synchronous Reluctance Motors (PMa-SyRMs).

Chapter 4

Torque control in a wide speed range

The operating of Permanent Magnet Synchronous Motors (PMSMs) and Sychronous Reluctance Motors (SynRMs) at high speeds in maximum torque per ampere (MTPA) condition leads to a certain flux-linkage amplitude corresponding to a given torque. This means that the steady-state voltage magnitude is proportional to speed, leading to insufficient phase voltage to control current above a certain speed, referred to as the "base speed". To address this, Flux-weakening (FW) and maximum torque per voltage (MTPV) regions are introduced, in which the flux-linkage magnitude is reduced. In the FW region, the current values should be chosen to produce the desired torque and satisfy the voltage constraint, but if the required current amplitude exceeds its limit, the current magnitude must be fixed at the limit, reducing the torque below the desired value.
The non-linear relationship between current and voltage magnitude, along with the non-linear flux characteristics of PMSMs and SynRMs, makes FW control challenging. To address this, various closed-loop techniques have been proposed, aiming for a robust FW control that is ideally parameter-independent. Some publications have focused on the analytical solution, using Ferrari's method to obtain the optimal current values [40], but this approach is computationally intensive and does not take into account the current limit constraint. To simplify the solution, approximation strategies such as using Taylor's series have been employed [41]. Some publications have also focused on numerical solutions using Lagrange-multiplier method and Newton's or Gauss-Newton method [43] [44], but these have lower accuracy compared to the analytical solution.
In this chapter, a novel analytical solution is presented, based on current magnitude minimization, to obtain the reference currents according to the desired torque. Thanks to a different problem formulation, the proposed method is much simpler than other analytical solutions. In fact, the number of cubic roots (the most demanding operation) to be computed in this case is lower than other analytical models, which greatly helps to decrease the computation time. The method is applied on an IPMSM in MTPA and FW region. Although the MTPV operation is considered in the torque control loop, the proposed method is focused on MTPA and FW regions.

4.1 Analytical model improvement for wide speed range

By considering core saturation effects, the stator flux linkages of the IPMSM can be obtain in synchronous reference frame.

$$\lambda_d(i_d, i_q) = L_d(i_d, i_q)i_d + \Lambda_{mg} \tag{4.1}$$

$$\lambda_q(i_d, i_q) = L_q(i_d, i_q)i_q \tag{4.2}$$

where i_d and i_q are the $d-$ and $q-$axes currents, L_d and L_q are the apparent inductances and Λ_{mg} is the stator flux linkage due to the permanent magnets; indeed it is the maximum value. The voltage equation in synchronous reference frame can be obtained as Eq. 2.31 and Eq. 2.32.
The current and voltage limits can be described as Eq. 2.46 and Eq. 2.45, if the Ohmic effect of stator resistance does not considered. As it can be seen in Fig. 4.1 the current limit shown by dashed circle centered (0,0) with I_s radius. The voltage limit is illustrated by doted ellipse centered $(-\frac{\Lambda_{mg}}{L_d}, 0)$. Based on Eq. 2.45 the voltage limit ellipse shrinks by increasing the speed of the motor.

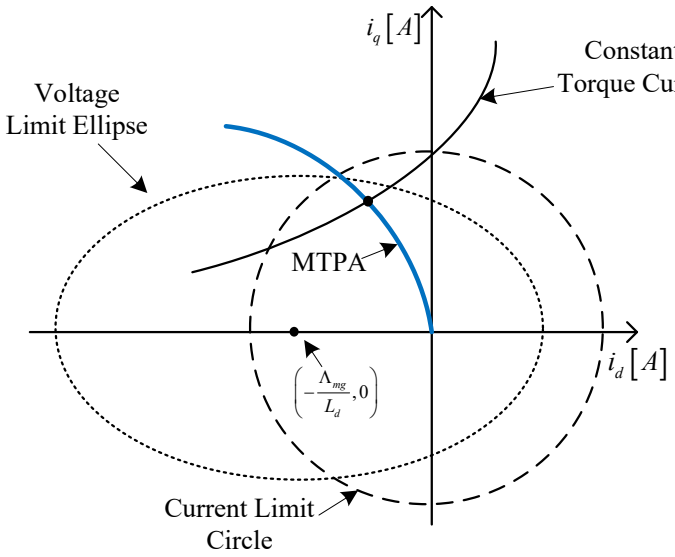

Figure 4.1: Constant torque curve, current circle limit and voltage limit ellipse in d-q axis.

4.1.1 Segmentation of Orientation Region

There are two states for operation region. In Chapter. 2, it discussed briefly. In this section, the segmentation of orientation region for two condition ($\frac{\Lambda_{mg}}{L_d} > I_{max}$ and $\frac{\Lambda_{mg}}{L_d} < I_{max}$) is explained in detail.

First Condition

First condition shown in Fig. 4.2, $\frac{\Lambda_{mg}}{L_d} > I_{max}$. By applying the convectional method the input is stator current (shown by '»'). In this condition, the MTPA operates in '*segmentI''*' ($O \sim H$). After reaching to the maximum stator current and voltage, the motor will operate in flux weakening region ('*segmentII''*') and the trajectory continuous from H through V where the value of apparent power is maximum constant value.
If the motor is controlled based on desired torque, the motor can operate in three segments (illustrated by '»'). '*segmentI*' is the MTPA region that is controlled based on the MTPA equation; current countor is depicted by $O \sim T$. From point T through U is the '*segmentII*' that the reference currents are obtained in constant torque region that the torque curve and the voltage ellipse have intersection. In this region the stator current is not in maximum value but the voltage is on maximum value. In this region, the motor operates based on the desired torque. And, the last operation region is the '*segmentIII*' that the $d-$ and $q-$ axis currents are evaluated by FW in maximum constant current region; illustrated by $U \sim V$. In this region the motor operate on the maximum apparent power.

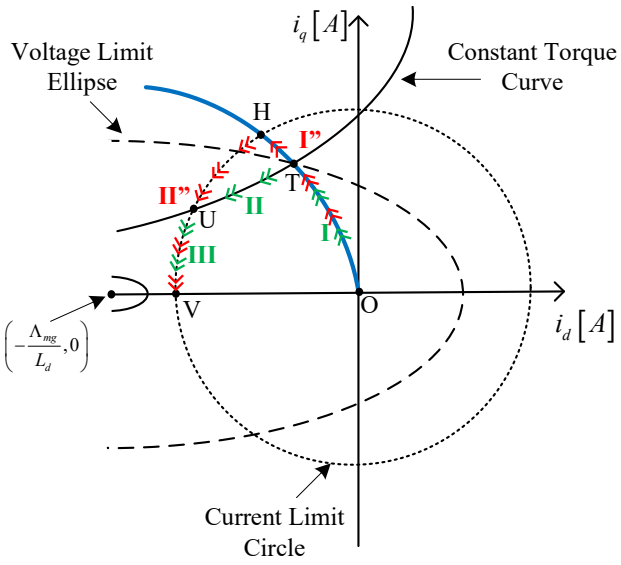

Figure 4.2: The operation region where $\frac{\Lambda_{mg}}{L_d} > I_{max}$.

Second Condition

In the second condition as shown in Fig. 4.3, $\frac{\Lambda_{mg}}{L_d} < I_{max}$. By applying the convectional method which the input is the stator current (shown by '»'). In this case, the MTPA is operate in '*segmentI''*' ($O \sim F$). After reaching to the maximum stator current and voltage the motor will operate in flux weakening region ('*segmentII''*') and the trajectory continuous from H through Q where the apparent power is maximum. After that, the motor will reach to the MTPV region and the trajectory will be R through S. In this region still motor operates in maximum stator voltage value ('*segmentIII''*').
If the motor controlled based on the desired torque, it operates in four segments (shown by

'»'). *'segmentI'* is the MTPA region; current trajectory is depicted by $O \sim P$. From point P through Q is the *'segmentII'* that the reference currents are obtained in constant torque region's equations. In this region, the constant torque curve and the voltage ellipse have intersection. Furthermore, in this region the the apparent power is on maximum value. The speed is not constant in different points. And the third operation region is the *'segmentIII'* that the $d-$ and $q-$ axis currents are evaluated by FW in maximum constant current region; illustrated by $Q \sim R$. The last operation part is called *'segmentIV'*, in this segment voltage ellipse has tangential intersection with constant torque curve, where the minimum stator current value can be obtained by MTPV estimation methods; the trajectory will be R through S. In this region motor operates in maximum stator voltage value.

Fig. 4.4 illustrates the torque vs speed curve of the motor in all range of the speed. The

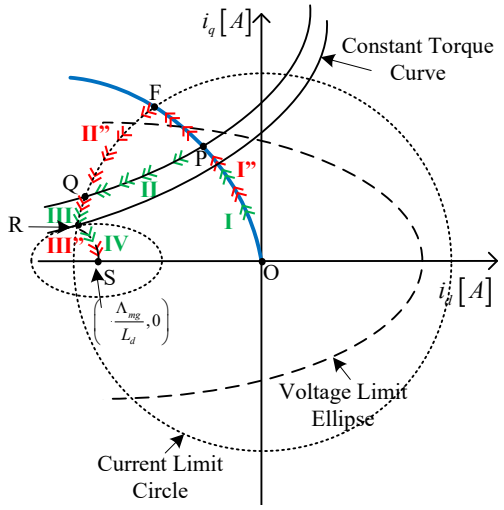

Figure 4.3: The operation region where $\frac{\Lambda_{mg}}{L_d} < I_{max}$.

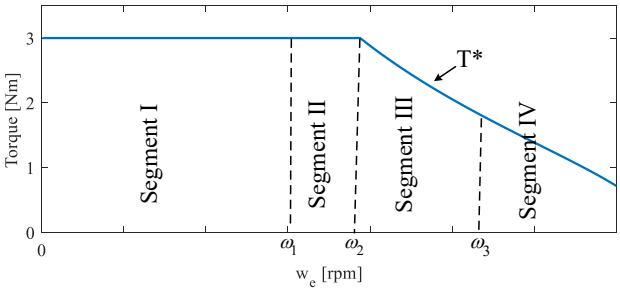

Figure 4.4: Torque vs speed curve in all speed range. $\frac{\Lambda_{mg}}{L_d} < I_{max}$.

torque is constant in *Segments I* and *II*. *Segment I* operates bellow ω_1. If the desired torque is the maximum torque, *Segment I* operates in base speed, in both condition ($\frac{\Lambda_{mg}}{L_d} < I_{max}$, $\frac{\Lambda_{mg}}{L_d} > I_{max}$) the torque is going to be decreased after ω_2. In second condiotion through *Segment IV* the motor operates in high speed range.

4.1.2 Conventional MTPA Solution

The conventional solution of MTPA region can be used to obtain $d-$ and $q-$ axis reference currents as follow [9]:

$$i_{d_{conv}} = \frac{\Lambda_{mg} \pm \sqrt{\Lambda_{mg}^2 + 8I_s^2(L_d - L_q)^2}}{4(L_d - L_q)} \tag{4.3}$$

$$i_{q_{conv}} = \pm\sqrt{I_s^2 - i_{d_{conv}}^2} \tag{4.4}$$

where $0 < I_s < I_{max}$. I_s is the output of the speed regulator. In this solution the controller does not have the ability to have the torque as the input of the MTPA region. Thus, if the desired torque is going to be controlled, this method is not applicable.

4.1.3 Ferrari's Analytical Solution

In [15], instead of using the stator current magnitude as the input of the MTPA, a desired torque is applied. In this paper, the Ferrari's method is used to obtain the $d-$ and $q-$ reference currents by finding the roots of the quartic equation, $x^4 + A_1x^3 + B_1x^2 + C_1x + D_1 = 0$. The Lagrangian multiplier solution is solved first to find the coefficients of the quartic equation. Where for the MTPA region the coefficients are,
$A_1 = \frac{3\Lambda_{mg}}{(L_d - L_q)}$,

$B_1 = \frac{3\Lambda_{mg}^2}{(L_d - L_q)^2}$,

$C_1 = \frac{\Lambda_{mg}^3}{(L_d - L_q)^3}$,

$D_1 = \frac{16T_{ref}^2}{18P_p^2(L_d - L_q)^2}$

Then the currents are obtained by Ferrari's method

$$i_{q_{MTPA_{1,2,3,4}}} = -\frac{A_1}{4} \pm_s \frac{\eta_1}{2} \pm_t \frac{\mu_1}{2} \tag{4.5}$$

where

$$\alpha_1 = \frac{1}{3}(3A_1C_1 - 12D_1 - B_1^2) \tag{4.6}$$

$$\beta_1 = \frac{1}{27}(-2B_1^3 + 9A_1B_1C_1 + 72B_1D_1 - 27C_1^2 - 27A_1^2D_1) \tag{4.7}$$

$$\gamma_1 = \frac{B_1}{3} + \sqrt[3]{\frac{\beta_1}{3} + \sqrt{\frac{\beta_1^2}{4} + \frac{\alpha_1^3}{27}}} + \sqrt[3]{-\frac{\beta_1}{3} - \sqrt{\frac{\beta_1^2}{4} + \frac{\alpha_1^3}{27}}} \tag{4.8}$$

$$\eta_1 = \sqrt{\frac{A_1^2}{4} - B_1 + \gamma_1} \tag{4.9}$$

$$\mu_1 = \sqrt{\frac{3}{4}A_1^2 - \eta_1^2 - 2B_1 \pm_s \frac{1}{4\eta_1}(4A_1B_1 - 8C_1 - A_1^3)} \tag{4.10}$$

Selecting the best value of the reference currents is explained in the [15]. Where,

$$i_{d_{MTPA}} = -\frac{A_1}{4} - \frac{\eta_1}{2} + \frac{\mu_1}{2} \tag{4.11}$$

$$i_{q_{MTPA}} = \frac{\frac{2T^*}{3p_p}}{\Lambda_{mg} + (L_d - L_q)i_{d_{MTPA}}} \tag{4.12}$$

To validate the Ferrari's method in MTPA region, it is compared with the conventional method. First, the $d-$ and $q-$ axis currents are obtained based on the conventional method. After calculating the reference currents, the electromagnetic torque equation is used to obtain the dq reference currents by Ferrari's solution. Then the obtained reference torque from

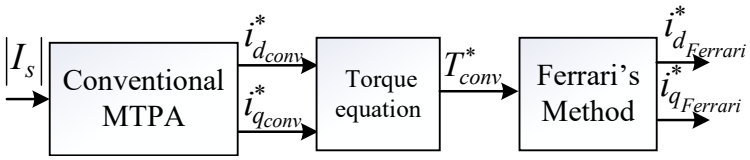

Figure 4.5: Ferrari's method validation using the obtained conventional torque.

the conventional method is used as the input of the Ferrari's method to obtain the $d-$ and $q-$ axis current values. Fig. 4.5 shows the Ferrari's method validation procedure in MTPA region. If the reference $d-$ and $q-$ axis currents of the Ferrari's method were equal to the $d-$ and $q-$ axis currents of the conventional method ($i_{d_{conv}} = i_{d_{Ferrari}}$,$i_{q_{conv}} = i_{q_{Ferrari}}$), it can be validate that the Ferrari's method is correct. Fig. 4.6 illustrate the simulation results of the MTPA region based on the conventional method (black circle 'O') and Ferrari's method (red asterisk '$*$'). According to the zoom-in on 2 Nm, 2.5 Nm and 3 Nm, both two methods fit on the MTPA trajectory. Also, the Ferrari's method is used to solve the equation for the flux-weakening region where just the coefficients of the quartic equation are different, $x^4 + A_2x^3 + B_2x^2 + C_2x + D_2 = 0$. Thus,

$A_2 = \frac{3\Lambda_{mg}}{(L_d - L_q)}(2 - \frac{L_q}{L_d})$,

$B_2 = \frac{\Lambda_{mg}^2}{(L_d - L_q)^2} + \frac{4\Lambda_{mg}^2}{L_d(L_d - L_q)^2} + \frac{\Lambda_{mg}^2}{L_d^2} - \frac{V_s^2}{\omega_e^2 L_d^2}$,

$C_2 = \frac{2\Lambda_{mg}}{L_d}(\frac{\Lambda_{mg}^2}{(L_d - L_q)^2} + \frac{\Lambda_{mg}^2}{L_d(L_d - L_q)^2} - \frac{V_s^2}{\omega_e^2 L_d(L_d - L_q)})$,

$D_2 = \frac{1}{(L_d - L_q)^2}(\frac{\Lambda_{mg}^4}{L_d^2} + \frac{L_q^2}{L_d^2}\frac{16T^{*2}}{9p_p^2} - \frac{V_s^2}{\omega_e^2}\frac{\Lambda_{mg2}}{L_d^2})$

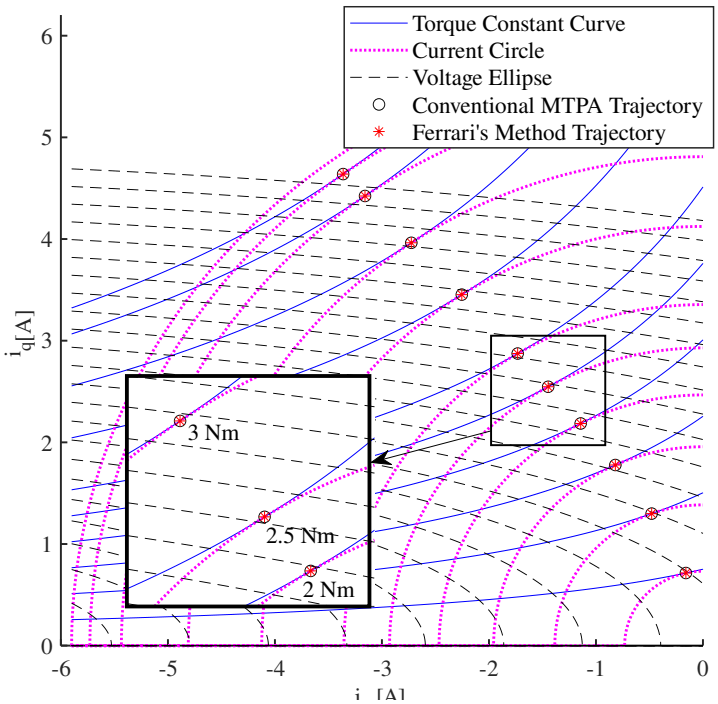

Figure 4.6: Simulation results of the MTPA region based on the conventional method and Ferrari's methods.

Then the reference currents of flux weakening region are obtained as follow,

$$i_{q_{FW_{1,2,3,4}}} = -\frac{A_2}{4} \pm_s \frac{\eta_2}{2} \pm_t \frac{\mu_2}{2} \tag{4.13}$$

where

$$\alpha_2 = \frac{1}{3}(3A_2C_2 - 12D_2 - B_2^2) \tag{4.14}$$

$$\beta_2 = \frac{1}{27}(-2B_2^3 + 9A_2B_2C_2 + 72B_2D_2 - 27C_2^2 - 27A_2^2D_2) \tag{4.15}$$

$$\gamma_2 = \frac{B_2}{3} + \sqrt[3]{\frac{\beta_2}{3} + \sqrt{\frac{\beta_2^2}{4} + \frac{\alpha_2^3}{27}}} + \sqrt[3]{-\frac{\beta_2}{3} - \sqrt{\frac{\beta_2^2}{4} + \frac{\alpha_2^3}{27}}} \tag{4.16}$$

$$\eta_2 = \sqrt{\frac{A_2^2}{4} - B_2 + \gamma_2} \tag{4.17}$$

$$\mu_2 = \sqrt{\frac{3}{4}A_2^2 - \eta_2^2 - 2B_2 \pm_s \frac{1}{4\eta_2}(4A_2B_2 - 8C_2 - A_2^3)} \tag{4.18}$$

Selecting the best value of the reference currents is explained in the [15]. Where,

$$i_{d_{FW}} = -\frac{A_2}{4} - \frac{\eta_2}{2} + \frac{\mu_2}{2} \tag{4.19}$$

$$i_{q_{FW}} = \frac{\frac{2T^*}{3p_p}}{\Lambda_{mg} + (L_d - L_q) i_{d_{FW}}} \tag{4.20}$$

there are two cubic roots in MTPA and flux weakening region according to the Eq. 4.8 and Eq. 4.16. The cubic roots will increase the computation time in microcontroller.

4.1.4 Proposed Minimum Vector Solution

In this section a novel solution is presented. The idea is to find the minimum vector of the current magnitude in MTPA region based on the desired torque. The $d-$ and $q-$axis reference currents can be obtained considering the electromagnetic torque equation. In fact, the main idea is minimizing the stator current to minimize the winding copper loss where is the dominant loss among other losses. The desired points in MTPA trajectory can be obtain by Minimum Vector Solution (MVS) based on constant torque curve. However, by using MTPA there will be some points outside the voltage limit ellipse Fig. 4.7 where is called flux weakening region. In this region, using the proposed method the minimum value of the stator current magnitude is obtained based on intersection of voltage ellipses and the torque curve.

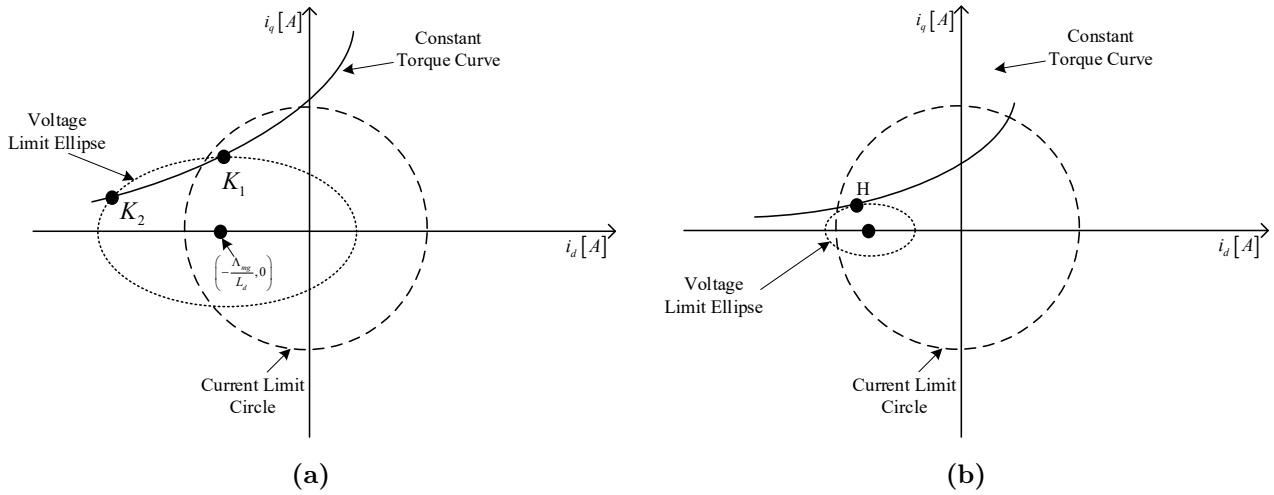

Figure 4.7: Voltage ellipse and constant torque intersection. (a) two intersections (b) MPTV region.

Minimum Vector Solution for Region i: MTPA region

In this region the minimum current is obtained by finding the minimum vector between point (0,0) and $(i_{d_{MTPA}}, i_{q_{MTPA}})$ by MVS based on the torque control loop. In fact, the minimum value of stator current is obtained by discovery the minimum vector from the center point of the coordinate and torque constant curve. The vector between point (0,0)

and ($i_{d_{MTPA}}$,$i_{q_{MTPA}}$) can be evaluated as follow:

$$D^2 = (i_{d_{MTPA}} - 0)^2 + (i_{q_{MTPA}} - 0)^2 \tag{4.21}$$

where $i_{d_{MTPA}}$ is found by electromagnetic torque equation average:

$$i_{d_{MTPA}} = \frac{2T_{ref} - \Lambda_{mg} 3 p_p i_{q_{MTPA}}}{3 p_p i_{q_{MTPA}} (L_d - L_q)} \tag{4.22}$$

T_{ref} is the reference torque. By substituting Eq. 4.22 in Eq. 4.21, the vector between desired points is evaluated.

$$D^2 = i^2_{q_{MTPA}} + \frac{4T^2_{ref} - 12 T_{ref} \Lambda_{mg} p_p i_{q_{MTPA}} + 9 \Lambda_{mg} p_p^2 i^2_{q_{MTPA}}}{9 p_p^2 i^2_{q_{MTPA}} (L_d - L_q)^2} \tag{4.23}$$

The minimum vector is at the point where $D'(i_{q_{MTPA}}) = 0$. When $D'(i_{q_{MTPA}}) = 0$ the square of D is zero. $D^2(i_{q_{MTPA}}) = 0$.
After solving and collecting $i_{q_{MTPA}}$ the quartic equation Eq. 4.24 is obtained. To find the $q-$ axis reference current Eq. 4.26 should be solved.

$$\frac{2.25}{T^2_{ref} \Lambda_{mg}} p_p^2 \Lambda_{mg} i^4_{q_{MTPA}} + \frac{1.5}{T_{ref}} p_p \Lambda_{mg} i_{q_{MTPA}} - 1 = 0 \tag{4.24}$$

The structure of quartic equation is $a_1 x^4 + b_1 x^3 + c_1 x^2 + d_1 x + e_1 = 0$. Based on the structue of the equation the coefficients are

$a_1 = \frac{2.25}{T^2_{ref}} p_p^2 (L_d - L_q)^2$,

$d_1 = \frac{1.5}{T_{ref}} p_p \Lambda_{mg}$,

$e_1 = -1$, $b_1 = c_1 = 0$. After finding the roots and doing simplification, the equation of $q-$axis current in MTPA region is calculated as follow:

$$i_{q_{MTPA_{1,2}}} = 0.5(\pm\sqrt{\frac{2d_1}{a_1\sqrt{C_1}} - C_1} - \sqrt{C_1}) \tag{4.25}$$

$$i_{q_{MTPA_{3,4}}} = 0.5(\pm\sqrt{-\frac{2d_1}{a_1\sqrt{C_1}} - C_1} - \sqrt{C_1}) \tag{4.26}$$

where,

$$A_1 = \sqrt[3]{0.5(3\sqrt{3}\sqrt{27a_1^2 d_1^4 - 256 e_1^3 a_1^3} + 27 a_1 d_1^2)} \tag{4.27}$$

$$B_1 = \frac{12 a_1 e_1}{A_1} \tag{4.28}$$

$$C_1 = \frac{A_1 + B_1}{3a_1} \tag{4.29}$$

There are four roots for $q-$axis current where the positive and non-complex root is acceptable as the best value for the reference current. The sign of a_1 and d_1 is positive, and the sign of e_1 is negative, then A_1 and C_1 are positive and B_1 is negative. Based on the sign of the parameters, $i_{d_{MTPA_{1,2}}}$ have real roots, that the real-positive root $i_{d_{MTPA_{1,2}}}$ is the best selection for $q-$axis current in the second quadrant of dq coordinate system. To find the real roots, $\frac{2d_1}{a_1\sqrt{C_1}}$ should be more than C_1 ($\frac{2d_1}{a_1\sqrt{C_1}} > C_1$). Thus the best selection of the $q-$axis current is:

$$i_{q_{MTPA}} = 0.5(\sqrt{\frac{2d_1}{a_1\sqrt{C_1}} - C_1} - \sqrt{C_1}) \tag{4.30}$$

The $d-$axis reference current is obtained by Eq. 4.22. To validate the MVS, it is compared with the conventional method. First, the $d-$ and $q-$ axis currents are obtained based on the conventional method. After calculating the reference currents the average torque equation is used to obtain the torque values in MTPA region based on the different stator currents value. Then the obtained reference torque from the conventional method is used as the input

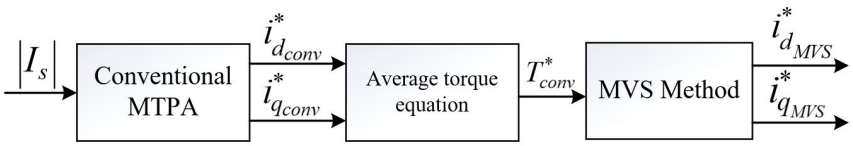

Figure 4.8: $d-$ and $q-$ axis reference current based on the MVS.

of the MVS to obtain the $d-$ and $q-$ axis current values. Fig. 4.8 shows the MVS validation procedure. If the reference $d-$ and $q-$ axis currents of the MVS method were equal to the $d-$ and $q-$ axis currents of the conventional method ($i_{d_{conv}} = i_{d_{MVS}}, i_{q_{conv}} = i_{q_{MVS}}$), it can be validate that the MVS solution is true. Fig. 7 illustrate the simulation results of the MTPA region based on the conventional method (orange dashed-line '- - -'), MVS (black square '□') and Ferrari's solution (red asterisk '∗'). According to the zoom-in on 2 Nm, 2.5 Nm and 3 Nm, all three methods fit on the MTPA trajectory.

Minimum Vector Solution for Region ii: Flux Weakening region

In conventional method the evaluation of $d-$ and $q-$ axis currents is done by maximum value of the stator current in flux-weakening region. But in some cases the maximum torque of the motor is limited in the current circle. In this region the intersection of the voltage ellipse and the costant torque curve is considered as the $d-$ and $q-$ axis reference currents. Fig. 4.7a illustrate the location of this points, there are two points K_1 and K_2 that according to the stator current magnitude, K_1 will be the best choice. Based on the MVS.

$$V_s^2 = v_{d_{FW}}^2 + v_{q_{FW}}^2 \tag{4.31}$$

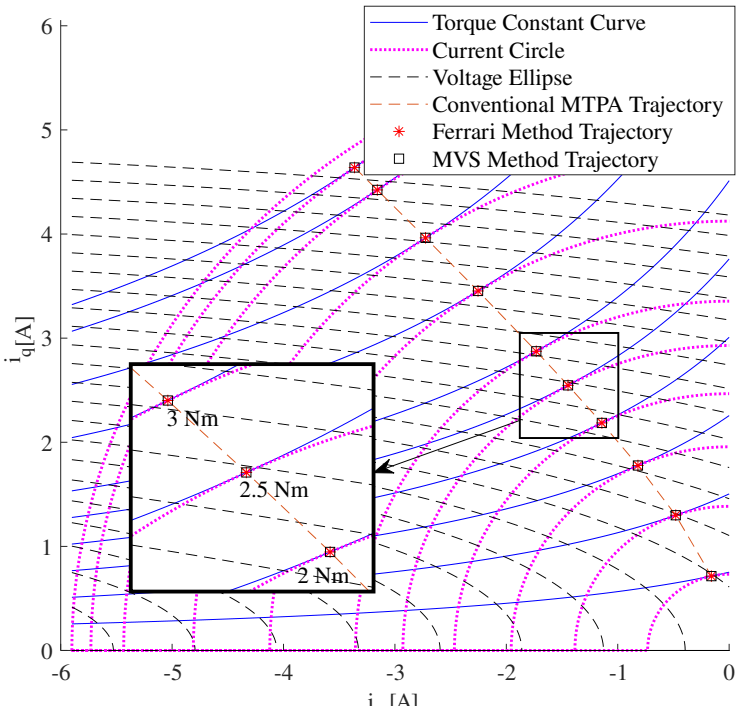

Figure 4.9: Simulation results of the MTPA region based on the conventional method, Ferrari's solution and MVS solution.

where $i_{q_{FW}}$ is obtained by electromagnetic torque equation.

$$i_{q_{FW}} = \frac{\frac{2T_{ref}}{3p_p}}{\Lambda_{mg} + (L_d - L_q)i_{d_{FW}}} \tag{4.32}$$

In steady state condition, the $d-$ and $q-$ axis voltages can be obtained as $v_{q_{FW}} = -L_q i_{q_{FW}} \omega_e$ and $v_{d_{FW}} = \omega_e L_d i_{d_{FW}} + \omega_e \Lambda_{mg}$. Thus, by substuting Eq. 4.32 in voltage equations in steady state condition and apply to the Eq. 4.31 the following equation is obtained,

$$(\Lambda_{mg}\omega_e + \frac{L_d\omega_e(2T_{ref} - 3\Lambda_{mg}i_{q_{FW}}p_p)}{+(L_d - L_q)i_{q_{FW}}p_p})^2 - V_s^2 + L_q^2 i_{q_{FW}}^2 \omega_e^2 \tag{4.33}$$

After collecting $i_{q_{FW}}$ a quartic equation is obtained:

$$\frac{9p_p^2(L_d - L_q)^2 L_q^2}{4L_d^2 T_{ref}^2} i_{q_{FW}}^4 + \frac{9p_p^2(-\Lambda_{mg}^2 L_q^2 \omega_e^2 + (L_d - L_q)^2 V_s^2)}{4L_d^2 T_{ref}^2} i_{q_{FW}}^2 - \frac{3\Lambda_{mg} L_q p_p}{L_d T_{ref}} i_{q_{FW}} + 1 = 0 \tag{4.34}$$

Where in this region,

$a_2 = \frac{9p_p^2(L_d - L_q)^2 L_q^2}{4L_d^2 T_{ref}^2}$,

$c_2 = \frac{9p_p^2(-\Lambda_{mg}^2 L_q^2 \omega_e^2 + (L_d - L_q)^2 V_s^2)}{4L_d^2 T_{ref}^2}$,

$d_2 = \frac{3\Lambda_{mg} L_q p_p}{L_d T_{ref}}$,

$e_2 = 1$ and $b_2 = 0$. Thus, the equation Eq. 4.35 and Eq. 4.36 are used to find the $q-$axis current.

$$i_{q_{FW_{1,2}}} = 0.5(C_2 \pm \sqrt{-\frac{4C_2}{3a_2} - B_2 - \frac{2d_2}{C_2 a_2}}) \tag{4.35}$$

$$i_{q_{FW_{3,4}}} = 0.5(-C_2 \pm \sqrt{-\frac{4C_2}{3a_2} - B_2 - \frac{2d_2}{C_2 a_2}}) \tag{4.36}$$

where,

$$A_2 = \frac{27a_2d_2^2}{2} - 36a_2c_2 + c_2^3 + \frac{\sqrt[3]{(2c_2^3 - 72a_2c_2 + 27a_2d_2^2)^2 - 4(c_2^2 + 12a_2)^3}}{2} \tag{4.37}$$

$$B_2 = \frac{A_2 + \frac{c_2^2 + 12a_2}{A_2}}{3a_2} \tag{4.38}$$

$$C_2 = \sqrt{B_2 - \frac{2c_2}{3a_2}} \tag{4.39}$$

The sign of a_2 is positive and d_2 is negetive, c_2 is positive if $\omega_e > \frac{(L_d - L_q)V_s}{(\Lambda_{mg} L_q}$, and it is negetive if $\omega_e < \frac{(L_d - L_q)V_s}{(\Lambda_{mg} L_q}$. It should be notice that c_2 should be positive to obtain real roots for $d-$ and $q-$ axis currents. Also, B_2 should be grater than $\frac{2c_2}{3a_2}$ ($B_2 > \frac{2c_2}{3a_2}$). The best current selection in the second quadrant dq coordinate system, considering the explained conditions is $i_{q_{FW_3}}$.
The $q-$ and $d-$ axis reference currents are obtained by voltage equation and Eq. 4.32 respectively.

$$i_{q_{FW_3}} = 0.5(C_2 + \sqrt{-\frac{4C_2}{3a_2} - B_2 - \frac{2d_2}{C_2 a_2}}) \tag{4.40}$$

Region *iii*: MTPV region

In the high speed region, if the $\frac{\Lambda_{mg}}{L_d} < I_{max}$ there will be tangential intersection between constant torque curve and voltage ellipse entire the current circle limit (Fig. 4.7b point H). By finding the tangential intersection the maximum torque is achieved for a given voltage. $i_d = \frac{\lambda_d - \Lambda_{mg}}{L_d}$ and $i_q = \frac{\sqrt{(V_s/\omega_e)^2 - \lambda_d^2}}{L_q}$, where by substituting voltage equation into electromagnetic torque, it can be obtained:

$$T_{tan}^2 = (\frac{3p_p}{2})^2(\lambda_d - L_q\frac{\lambda_d - \Lambda_{mg}}{L_d})^2\frac{(V_s/\omega_e)^2 - \lambda_d^2}{L_q^2} \tag{4.41}$$

The reference value of the $d-$axis flux linkage is calculated by evaluating differentiation with respect to λ_d and equal it zero.

$$\lambda_d^* = \frac{-L_q\Lambda_{mg} \pm \sqrt{L_q^2\Lambda_{mg} + 8(L_d - L_q)^2(V_s/\omega_e)^2}}{4(L_d - L_q)} \tag{4.42}$$

By using Eq. 4.42, $d-$ and $q-$ axis currents in MTPV region are obtained.

$$i_{d_{tan}} = \frac{\lambda_d^* - \Lambda_{mg}}{L_d} \tag{4.43}$$

$$i_{q_{tan}} = \frac{\sqrt{(V_s/\omega_e)^2 - \lambda_d^{*2}}}{L_q} \tag{4.44}$$

4.1.5 Current Control Algorithm and System Control Block Diagram

As it shown in Fig. 4.10, the torque control block diagram works based on selecting the reference currents by applying proposed MVS. By desired torque and the controlled speed of the motor as the input of the minimum vector algorithm the $d-$ and $q-$ axis reference currents are selected, as it is shown in Fig. 4.11. The flowchart steps are as below:

Step1: start algorithm.
Step2: read reference torque T_{ref} and motor parameters, L_d, L_q, Λ_{mg}, $V_{s_{max}}$, I_s and the motor speed ω_{me}.
Step3: if the $T_{ref} \leq T_{tan}$, request torque reduction and go to **Step2**. Otherwise go to **Step4**.
Step4: calculate $V_{s_{MTPA}}$.
Step5: if $|V_{s_{MTPA}}| \leq |V_{s_{max}}|$, go to **Step6**, otherwise go to **Step9**.
Step6: calculate $(i_{d_{MTPA}}, i_{q_{MTPA}})$.
Step7: if $i_{d_{MTPA}} + i_{q_{MTPA}} \leq I_s$ go to **Step8**, otherwise request torque reduction and go to **Step2**.
Step8 reference currents in MTPA region can be evaluated $(i_{d_{ref}} = i_{d_{MTPA}}, i_{q_{ref}} = i_{q_{MTPA}})$.
Step9: calculate $(i_{d_{FW}}, i_{q_{Fw}})$.
Step10 if $i_{d_{FW}} + i_{q_{FW}} \leq I_s$ go to **Step11**, otherwise request torque reduction and go to **Step2**.
Step11: reference currents in FW region can be evaluated $(i_{d_{ref}} = i_{d_{FW}}, i_{q_{ref}} = i_{q_{FW}})$.

4.1.6 Results

An IPMSM motor is selected (Table 4.1). MATLAB are used for simulation. In the simulations the non-linearity of the inductances has not been considered. If $\frac{\Lambda_{mg}}{L_d} > I_{max}$ then

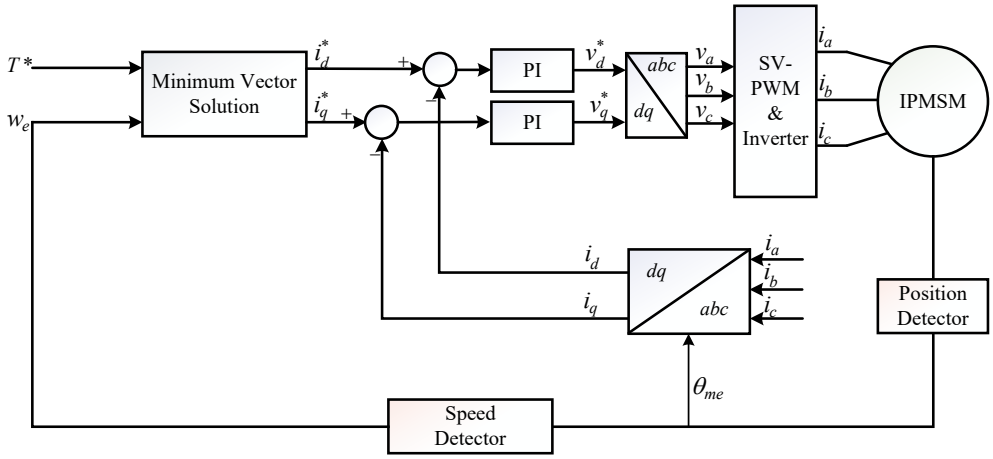

Figure 4.10: Torque control block diagram with MVS method.

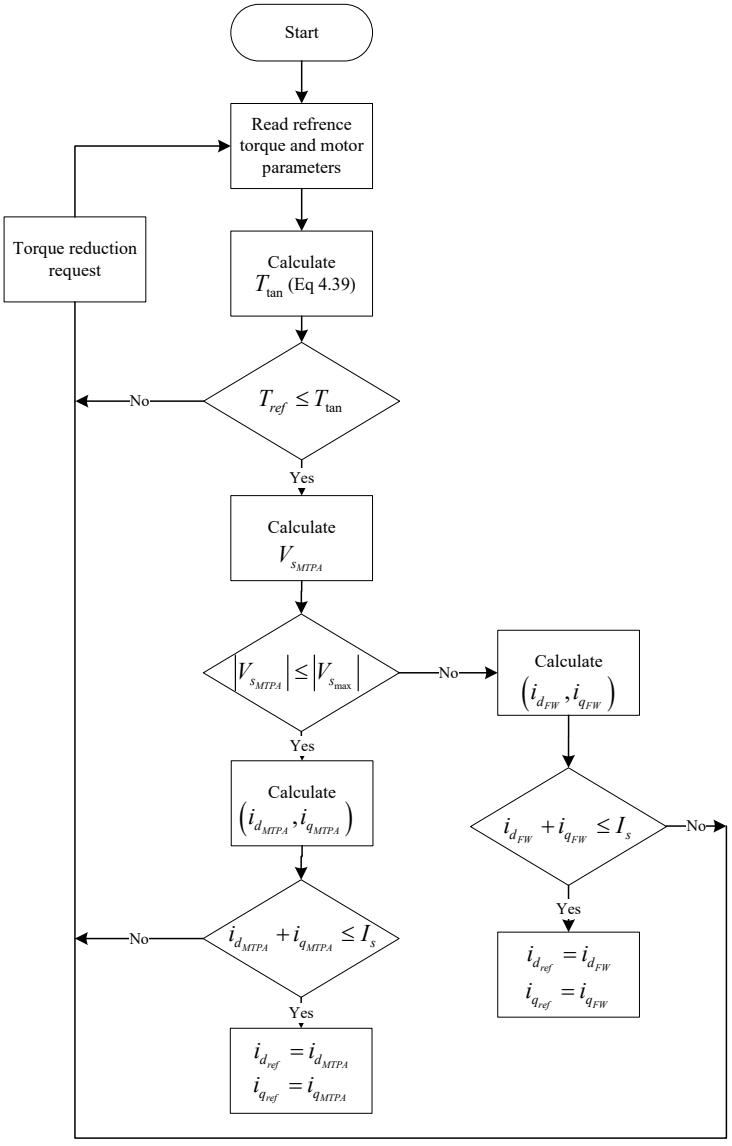

Figure 4.11: Reference current selection algorithm.

the motor works in first condition, thus the voltage does not have tangential intersection with torque entire current circle limit. As the first test, the torque is increased from 0.5 Nm to 6.5 Nm to check the MTPA trajectory. The maximum desired torque is considered as 6.5 Nm. The $d-$ and $q-$ axis current trajectory is presented in Fig. 4.12 that is tested in MATLAB. As it mentioned the operation region is changed from *region i* (MTPA region)

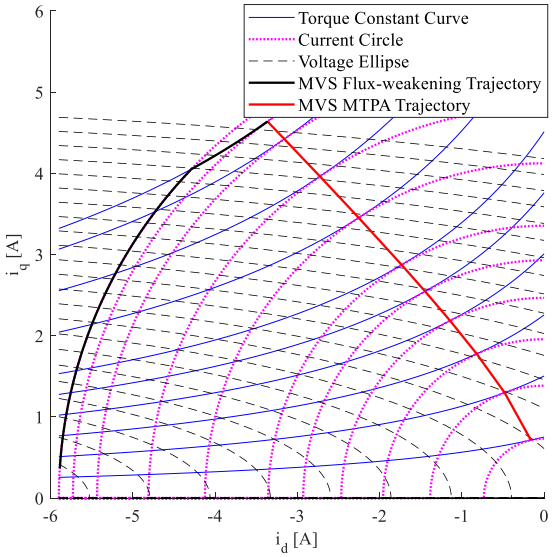

Figure 4.12: MATLAB simulations for $d-$ and $q-$ axis currents trajectory respect to the desired torque (6.5 Nm considered as maximum desired torque).

to *region ii* (Flux weakening region) at 1480 rpm when the desired torque is 6.5 Nm. Then at 1700 rpm due to the maximum current limitation the torque reduction is requested, and the reference currents are obtained by proposed method for *region ii*.
Fig. 4.13a illustrate the speed vs torque curve for 6.5 Nm. As it can be seen, the torque is 6.5 Nm through 1700 rpm and after that the torque reduction is requested. $d-$ and $q-$ axis current behavior is shown in Fig. 4.13b. Below 1480 rpm the $d-$ and $q-$ axis currents are -3.36 A and 4.63 A ,respectively. After that in flux weakening region, the currents are decreased based on voltage ellipse and torque curve intersection. The stator current is 5.72 A in MTPA region (under 1480 rpm).

Between 1480 rpm and 1700 rpm the stator current is increased (operate in *region ii*) and after 1700 rpm it is operated on maximum stator current (5.9 A) (Fig. 4.13c). Fig. 4.13d illustrates the variation of stator voltage respect to the speed. As it can be seen before 1480 rpm the stator voltage is increased and after 1480 rpm it is settled on 144 V.
Fig. 4.14 present the MTPA and flux weakening trajectory in MATLAB. In this test the maximum desired torque is 3 Nm. As the first test, the torque is increased from 0.5 Nm to 3 Nm to check the MTPA trajectory. In this scenario, the operation region is changed from *region i* (MTPA region) to *region ii* (Flux weakening region) in 2095 rpm. Then in 3879 rpm due to the maximum current limitation the torque reduction is requested, and the reference currents are obtained by proposed method for *region ii*. Fig. 4.15a illustrates the speed vs torque curve for 3 Nm. As the result, the torque is 3 Nm through 3879 rpm and

Table 4.1: IPMSM Parameters.

Variable	Value
Number of pole paires(p_p)	2
Base speed(ω_{base})	1480 RPM
Maximum torque	6.5 N.m
Maximum current(I_{max})	5.9 A
DC-link voltage(V_s)	250 V
Permanent magnet flux(Λ_{mg})	0.221613
$d-$axis inductance(L_d)	22 mH
$q$axis inductance(L_q)	95 mH
Stator resistance(R_s)	3.4 Ohm

after that the torque reduction is requested.
The $d-$ and $q-$ axis current behavior is shown in Fig. 4.15b. Below 2095 rpm the $d-$ and $q-$ axis currents are -1.73 A and 2.87 A, respectively. After that in flux weakening region, the currents are decreased based on voltage ellipse and torque curve intersection. The stator current is 3.35 A in MTPA region (under 2095 rpm). Between 2095 rpm and 3879 rpm the stator current is increased (operate based on *region ii*) and after 3879 rpm it is operated on maximum stator current (5.9 A) (Fig. 4.15c). Fig. 4.15d illustrates the variation of stator voltage respect to the speed. As it can be seen before 2095 rpm it is increased and after 2095 it is settled on 144 V.
In Table. 4.2, the computation time of Ferrari's method [15] and the proposed method based on experimental results in both MTPA region and flux-weakening region is presented. It

Table 4.2: Computation time comparison for Ferrari's method and proposed method (MVS) in MTPA and FW region

Analytical solution	Region	Computation time
Ferrari's solution	MTPA	6.15 μs
Ferrari's solution	FW	8.64 μs
MVS solution	MTPA	3.43 μs
MVS solution	FW	4.40 μs

is implemented on Texas Instruments C2000 microcontroller (TSM320F280049). The computation time for Ferrari's method and proposed method is 6.15 μs and 3.43 μs respectively in MTPA region that the calculation time reduction is 56%. For flux weakening region the results are 8.64 μs and 4.4 μs for Ferrari's and proposed solutions, respectively that the calculation time reduction is 50%. The main reason of this difference is the cubic roots. There are 2 cubic roots in Ferrari's solution and 1 cubic root in the proposed method. The computation time for cubic roots using TSM320F280049 is around 2.2 μs.

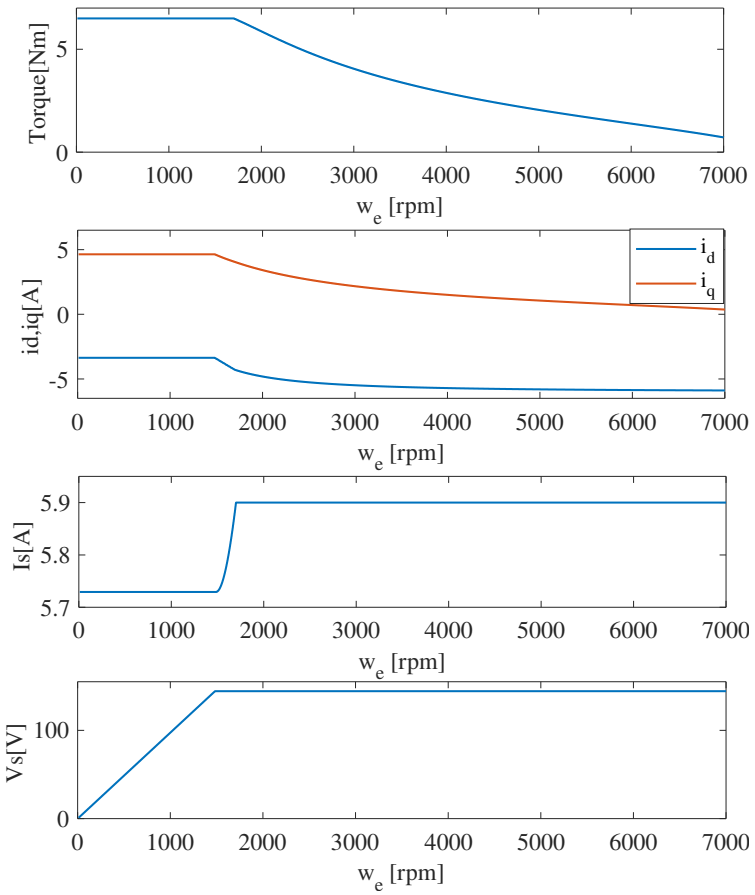

Figure 4.13: (a) speed vs torque (b) speed vs dq axis currents (c) speed vs stator current (d) speed vs stator voltage curves respect to the 6.5 Nm as maximum desired torque.

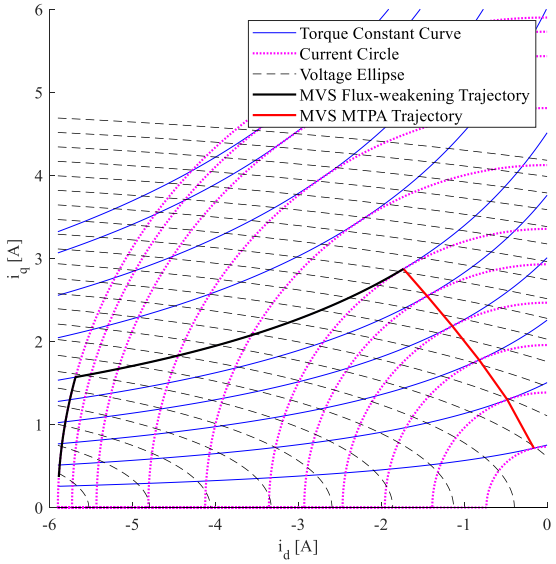

Figure 4.14: MATLAB simulations for $d-$ and $q-$ axis currents trajectory respect to the desired torque (3 Nm).

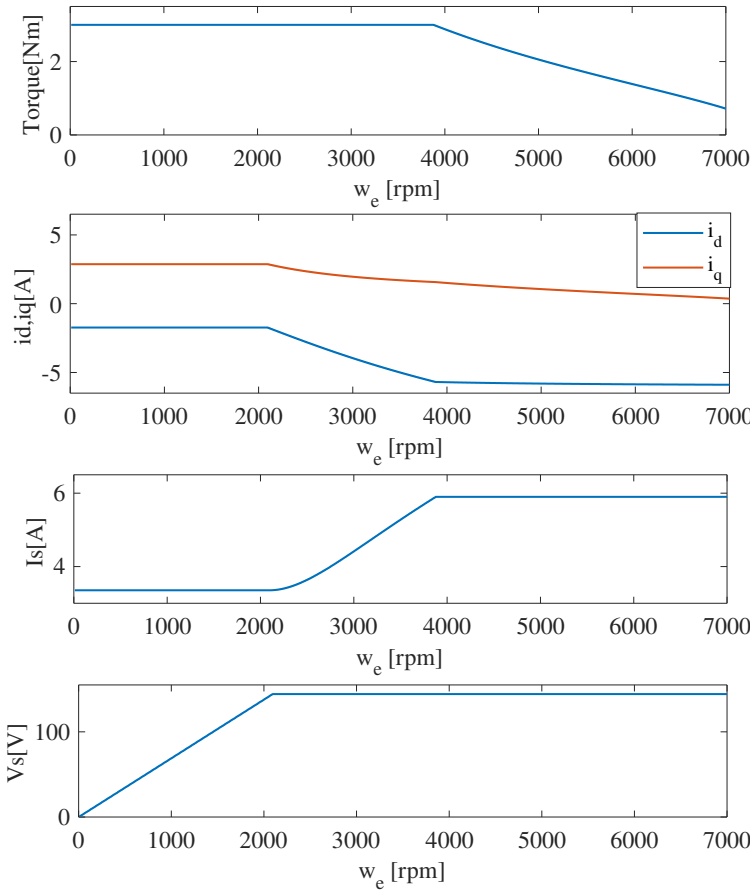

Figure 4.15: (a) speed vs torque (b) speed vs dq axis currents (c) speed vs stator current (d) speed vs stator voltage curves respect to the 3 Nm as desired torque.

4.1.7 Experimental Results

In this subsection, the experimental results of the novel method (MVS), in MTPA region are presented. Fig. 3.13 illustrates the control and power board of the experimental implementation. Two power supplies are used to power the drive; the first one provides 24V DC to the control board (TMS320F82069) and the second power source provides 100V DC to the power board. The motor positioned on a test rig, is connected to the inverter board. An hysteresis brake (Magtrol HD-715) is attached to the motor shaft to provide the load torque and is controlled by a Magtrol DSP7000.

The applied sampling frequency for the control is equal to the switching frequency, i.e. 10 kHz and the speed of the motor is 300rpm. The tests are carried out at three load torque values: 2Nm, 4Nm and 6Nm. The motor parameters and dq apparent inductance maps are presented in Table. 3.1. Fig .3.6 . Fig. 4.16 illustrate the MVS MTPA steady-state trajectory based on three experimental tests for each load torque value, namely calculated with constant inductance, adaptive $q-$axis inductance and other operating points out of the calculated MTPA, but at the same load torque ("MTPA perturbation"). As can be seen, the calculated MTPA points are very close to the actual MTPA (tangential point). The accuracy of the MVS is higher when the adaptive $q-$axis inductance is applied to the

MTPA. However, it can be seen that, even considering the constant inductance, the MTPA trajectory is tracked with an acceptable accuracy.

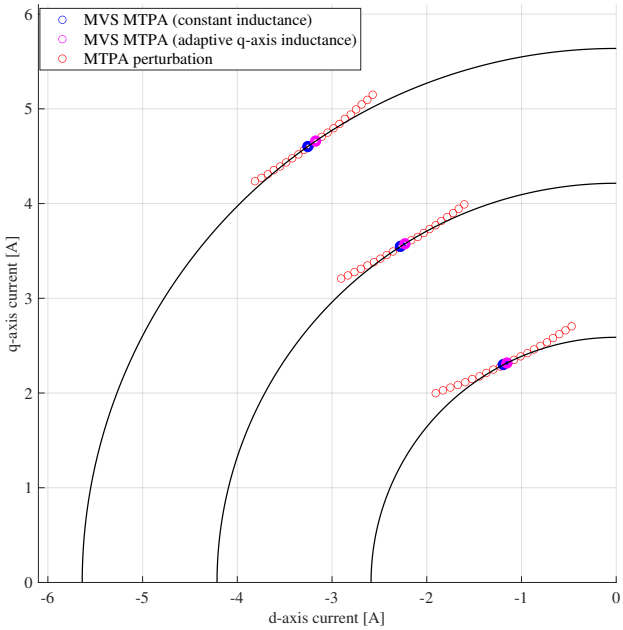

Figure 4.16: Minimum vector solution MTPA trajectory in dq axis currents coordinate using constant motor parameters and adaptive q-axis inductance.

Fig. 4.16 reports the same data as the previous figure, emphasizing the relationship between torque and current magnitude. The MVS, in both cases (i.e. calculated using constant inductance and adaptive $q-$axis inductance), guarantees the minimum current magnitude for a given load torque, or a value that is very close to the minimum, so that it cannot be practically discriminated. In fact, it should be noted that any differences in current that are in the order of few mA and up to few tens of mA should be disregarded, given the limited measurement accuracy of the setup. Considering that the current measurement range is approximately ± 30 A, a difference in the order of 10 mA corresponds to approximately 0.03% of the full-scale value.

Fig. 4.18 illustrates the accuracy of torque actuation, i.e. the correspondence between torque reference (command) and actual torque output. The measured points are very close equality (i.e. the load torque is very close to the commanded value). However, a constant difference is visible, which corresponds exactly to the no-load commanded torque, thus it can be attributed to the friction effects. The dashed line represents the expected total torque corresponding to each load torque value, i.e. the sum of load torque and friction. Since the measured points lay on the dashed line (especially in the adapted inductance case), it can be concluded that the MVS algorithm actuates the torque command very accurately, i.e. with less than 1% error (0.9, 0.2 and 0.4% for 2, 4 and 6 Nm, respectively).

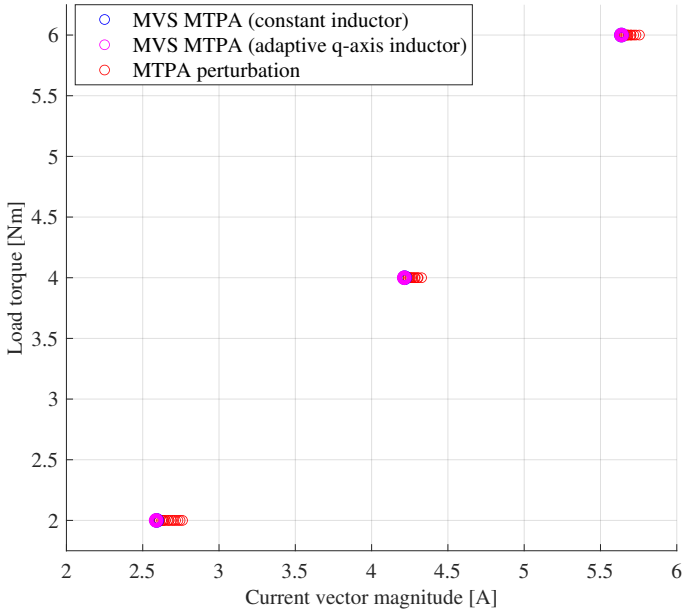

Figure 4.17: Torque reference versus current magnitude plane of minimum vector solution MTPA using constant motor parameters and adaptive q-axis inductance.

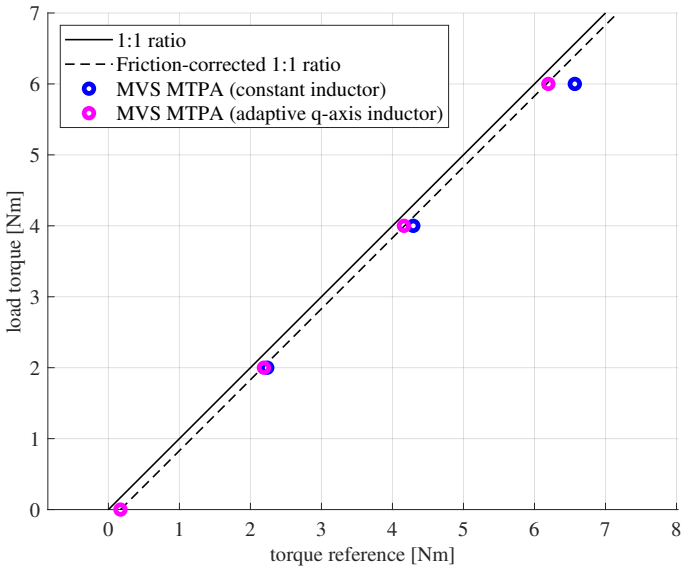

Figure 4.18: Torque reference versus load torque.

4.2 Conclusion

In this Section a new analytical solution is presented to control the motor torque in the maximum-torque-per-ampere and flux-weakening region with a torque constraint. The controller is designed to operate in wide speed range; MTPA, flux weakening and MTPV regions. Based on the proposed solution the complexity of the quartic equation of dq axis current is decreased significantly. The method is compared with another analytical solution, experimentally to investigate them based on the computation time. By using the proposed method, the computation time is decreased 56% versus Ferrari's method for MTPA region.

In flux weakening region the difference of computation time for the proposed method and Ferrari's solution is 51%. Furthermore, the novel solution is applied to an IPMSM in MTPA region experimentally considering constant and adaptive q-axis inductance. As a results, the proposed method track the MTPA trajectory with a high accuracy.
As the future work, the novel method is going to be tested experimentally in flux-weakening region. In addition, the minimum vector solution can be studied analytically in MTPV region.

Chapter 5

IPMSM and SynRM Parameters Approximation

In this chapter, a new method for approximating the flux-linkage maps of an Interior Permanent Magnet Synchronous Motor (IPMSM) using the Group Method of Data Handling (GMDH) method is proposed. The importance of these maps is due to the non-linear magnetic behavior of IPMSMs and Permanent Magnet Synchronous Motors (SynRMs), which makes them crucial for various control applications, including current control, gains adaptation, axes decoupling, Maximum Torque Per Ampere (MTPA), Field Weakening (FW), and sensor-less control.

In most case, off-line characterization methods have been used to obtain the system parameters, but these methods require a large amount of time for commissioning and specialized hardware. On the other hand, simple analytical methods that assume constant parameters may not provide accurate results. In order to improve the accuracy of the approximations, other methods have been proposed, such as the Look-Up Table (LUT) [46][47] method and polynomial approximation. The LUT method uses pre-computed data to obtain the system parameters, while polynomial approximation fits a polynomial function to the data. However, both methods require all parameters to be obtained off-line.

The GMDH method proposed in this chapter uses a neural network to efficiently approximate the flux-linkage maps online, based on the current inputs. The proposed method has been analyzed in a case study and the results show that the accuracy of the GMDH method is higher than the polynomial approximation, with up to 2-3 times smaller error. This means that the GMDH method is a more efficient and accurate approach for approximating the flux-linkage maps of IPMSMs.

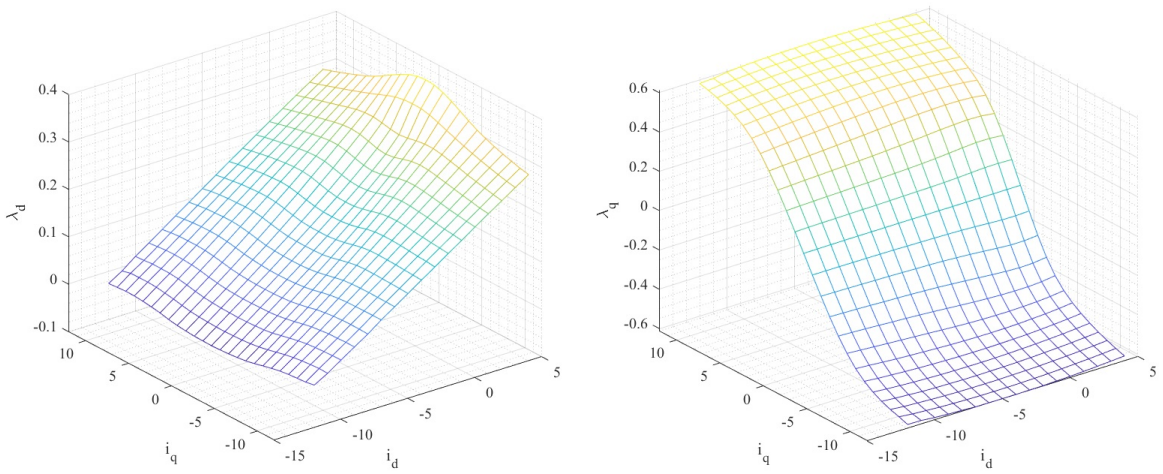

Figure 5.1: $d-$ and $q-$axis flux-linkages maps based on LUT. (a) for $d-$axis flux-linkage (b) for $q-$axis flux-linkage.

5.1 Using Polynomial Method to Approximate the PMSM Flux-linkage Maps

In polynomial method the relation of the motor parameters to the $d-$ and $q-$axis currents is going to be considered to extend the Taylor's series [76]. Eq. 5.1 and Eq. 5.2 are obtained by the Taylor's series for $d-$ and $q-$axis flux-linkages.

$$\begin{aligned}\lambda_d(i_d,i_q) =& \lambda_d(i_{d0},i_{q0}) + \frac{\partial\lambda_d}{\partial i_d}(i_d-i_{d0}) + \frac{\partial\lambda_d}{\partial i_q}(i_q-i_{q0}) + \frac{1}{2}\frac{\partial^2\lambda_d}{\partial i_d^2}(i_d-i_{d0})^2 + \\ &+ \frac{\partial^2\lambda_d}{\partial i_d\partial i_q}(i_d-i_{d0})(i_q-i_{q0}) + \frac{1}{2}\frac{\partial^2\lambda_d}{\partial i_q^2}(i_q-i_{q0})^2 + \frac{1}{6}\frac{\partial^3\lambda_d}{\partial i_d^3}(i_d-i_{d0})^3 + \\ &+ \frac{1}{2}\frac{\partial^3\lambda_d}{\partial i_d^2\partial i_q}(i_d-i_{d0}) + \frac{1}{2}\frac{\partial^3\lambda_d}{\partial i_d\partial i_q^2}(i_d-i_{d0})^2 + \frac{1}{6}\frac{\partial^3\lambda_d}{\partial i_q^3}(i_q-i_{q0})^3\end{aligned} \tag{5.1}$$

$$\begin{aligned}\lambda_q(i_d,i_q) =& \lambda_q(i_{d_0},i_{q_0}) + \frac{\partial\lambda_q}{\partial i_d}(i_d-i_{d0}) + \frac{\partial\lambda_q}{\partial i_q}(i_q-i_{q0}) + \frac{1}{2}\frac{\partial^2\lambda_q}{\partial i_d^2}(i_d-i_{d0})^2 + \\ &+ \frac{\partial^2\lambda_q}{\partial i_d\partial i_q}(i_d-i_{d0})(i_q-i_{q0}) + \frac{1}{2}\frac{\partial^2\lambda_q}{\partial i_q^2}(i_q-i_{q0})^2 + \frac{1}{6}\frac{\partial^3\lambda_q}{\partial i_d^2}(i_d-i_{d0})^3 + \\ &+ \frac{1}{2}\frac{\partial^3\lambda_q}{\partial i_d^2\partial i_q}(i_d-i_{d_0}) + \frac{1}{2}\frac{\partial^3\lambda_q}{\partial i_d\partial i_q^2}(i_d-i_{d0})^2 + \frac{1}{6}\frac{\partial^3\lambda_q}{\partial i_q^3}(i_q-i_{q0})^3\end{aligned} \tag{5.2}$$

The equations can be simplified by considering the partial parts as the coefficients of the $d-$ and $q-$axis currents.

$$\begin{aligned}\lambda_d(i_d,i_q) =& p_{d00}+p_{d10}i_d+p_{d01}i_q+p_{d20}i_d^2+p_{d11}i_di_q+p_{d02}i_q^2\\ &+p_{d30}i_d^3+p_{d21}i_d^2i_q+p_{d12}i_di_q^2+p_{d03}i_q^3\\ \lambda_q(i_d,i_q) =& p_{q00}+p_{q10}i_d+p_{q01}i_q+p_{q20}i_d^2+p_{q11}i_di_q+p_{q02}i_q^2\\ &+p_{q30}i_d^3+p_{q21}i_d^2i_q+p_{q12}i_di_q^2+p_{q03}i_q^3\end{aligned} \tag{5.3}$$

thus,

$p_{d00}=\lambda_d(i_{d0},i_{q0})+\frac{\partial\lambda_d}{\partial i_d}i_{d0}-\frac{\partial\lambda_d}{\partial i_q}i_{q0}+\frac{1}{2}\frac{\partial^2\lambda_d}{\partial i_d^2}i_{d0}^2+\frac{\partial^2\lambda_d}{\partial i_d\partial i_q}i_{d0}i_{q0}+\frac{1}{2}\frac{\partial^2\lambda_d}{\partial i_q^2}i_{q0}^2-\frac{1}{6}\frac{\partial^3\lambda_d}{\partial i_d^3}i_{d0}^3-\frac{1}{2}\frac{\partial^3\lambda_d}{\partial i_d^2\partial i_q}i_{d0}^2i_{q0}-\frac{1}{2}\frac{\partial^3\lambda_d}{\partial i_d\partial i_q^2}i_{d0}i_{q0}^2-\frac{1}{6}\frac{\partial^3\lambda_d}{\partial i_q^3}i_{q0}^3$

$p_{d10}=\frac{\partial\lambda_d}{\partial i_d}-\frac{\partial^2\lambda_d}{\partial i_d^2}i_{d0}-\frac{\partial^2\lambda_d}{\partial i_d\partial i_q}i_{q0}+\frac{1}{2}\frac{\partial^3\lambda_d}{\partial i_d^3}i_{d0}^2+\frac{\partial^3\lambda_d}{\partial i_d^2\partial i_q}i_{d0}i_{q0}+\frac{1}{2}\frac{\partial^3\lambda_d}{\partial i_d\partial i_q^2}i_q^2$

$p_{d01}=\frac{\partial\lambda_d}{\partial i_q}-\frac{\partial^2\lambda_d}{\partial i_q^2}i_{q0}-\frac{\partial^2\lambda_d}{\partial i_q\partial i_q}i_{d0}+\frac{1}{2}\frac{\partial^3\lambda_d}{\partial i_q^3}i_{q0}^2+\frac{\partial^3\lambda_d}{\partial i_d\partial i_q^2}i_{d0}i_{q0}+\frac{1}{2}\frac{\partial^3\lambda_d}{\partial i_d^2\partial i_q}i_{d0}^2$

$p_{d20}=\frac{1}{2}\frac{\partial^2\lambda_d}{\partial i_d^2}-\frac{1}{2}\frac{\partial^3\lambda_d}{\partial i_d^3}i_{d0}-\frac{1}{2}\frac{\partial^3\lambda_d}{\partial i_d^2i_q}i_{q0}$

$p_{d11}=\frac{\partial^2\lambda_d}{\partial i_di_q}-\frac{\partial^3\lambda_d}{\partial i_d^2i_q}i_{d0}-\frac{\partial^3\lambda_d}{\partial i_di_q^2}i_{q0}$

$p_{d02}=\frac{1}{2}\frac{\partial^2\lambda_d}{\partial i_q^2}-\frac{1}{2}\frac{\partial^3\lambda_d}{\partial i_q^3}i_{q0}-\frac{1}{2}\frac{\partial^3\lambda_d}{\partial i_di_q^3}i_{d0}$

$p_{d30}=\frac{1}{6}\frac{\partial^3\lambda_d}{\partial i_d^3}$

$p_{d21}=\frac{1}{2}\frac{\partial^3\lambda_d}{\partial i_d^2i_q}$

$p_{d12}=\frac{1}{2}\frac{\partial^3\lambda_d}{\partial i_di_q^2}$

$p_{d03}=\frac{1}{6}\frac{\partial^3\lambda_d}{\partial i_q^3}$

By considering that $N\times N$ data is collected from the motor the matrix can be written as below (N^2 dimension matrix is arranged for λ_d and λ_q):

$$\begin{aligned}\lambda_d &= X_dP_d\\ \lambda_q &= X_qP_q\end{aligned} \tag{5.4}$$

where X_d and X_q are matrixes of $N^2\times 10$. The parameters vector of $d-$ and $q-$ flux-linkages are presented as P_d and P_q. By using least square approach the coefficient of the parameters can be obtained.

$$\begin{aligned}P_d &= \left(X_d^TX_d\right)^{-1}X_d^T\lambda_d\\ P_q &= \left(X_q^TX_q\right)^{-1}X_q^T\lambda_q\end{aligned}$$

After obtaining the parameters, the flux-linkages should satisfy the reciprocity condition:

$$\frac{\partial \lambda_d(i_d, i_q)}{\partial i_q} = \frac{\partial \lambda_q(i_d, i_q)}{\partial i_d} \tag{5.5}$$

If the flux-linkage equation does not satisfied the reciprocity condition by using least square method, the coefficients should be modified as follow:

$$\begin{gathered} \bar{p}_{d01} + \bar{p}_{d11} i_d + 2\bar{p}_{d02} i_q + \bar{p}_{d21} i_d^2 + 2\bar{p}_{d12} i_d i_q + 3\bar{p}_{d03} i_q^2 \\ = \\ \bar{p}_{q10} + 2\bar{p}_{q20} i_d + p_{q11} i_q + 3\bar{p}_{q30} i_d^2 + 2\bar{p}_{q21} i_d i_q + \bar{p}_{q12} i_q^2 \end{gathered} \tag{5.6}$$

Thus based on the equation the coefficients of same order should be the same,then:

$$\begin{aligned} &\bar{p}_{d01} = \bar{p}_{q10}, \quad \bar{p}_{d11} = 2\bar{p}_{q20}, \quad 2\bar{p}_{d02} = \bar{p}_{q11} \\ &\bar{p}_{d21} = 3\bar{p}_{q30}, \quad \bar{p}_{d12} = \bar{p}_{q21}, \quad 3\bar{p}_{d03} = \bar{p}_{q12} \end{aligned} \tag{5.7}$$

The best feasible approach is to add and subtract a half of correction term that can be evaluated by Eq. 5.7. As a result, the flux-linkages satisfy Eq. 5.5 and the following equations can be obtained:

$$\begin{aligned} \lambda_d(i_d, i_q) =& \bar{p}_{d00} + \bar{p}_{d10} i_d + \bar{p}_{d01} i_q + \bar{p}_{d20} i_d^2 + \bar{p}_{d11} i_d i_q + \bar{p}_{d02} i_q^2 \\ &+ \bar{p}_{d30} i_d^3 + \bar{p}_{d21} i_d^2 i_q + \bar{p}_{d12} i_d i_q^2 + \bar{p}_{d03} i_q^3 \\ \lambda_q(i_d, i_q) =& \bar{p}_{q00} + \bar{p}_{q10} i_d + \bar{p}_{q01} i_q + \bar{p}_{q20} i_d^2 + \bar{p}_{q11} i_d i_q + \bar{p}_{q02} i_q^2 \\ &+ \bar{p}_{q30} i_d^3 + \bar{p}_{q21} i_d^2 i_q + \bar{p}_{q12} i_d i_q^2 + \bar{p}_{q03} i_q^3 \end{aligned} \tag{5.8}$$

If the flux saturation is considered, the Eq. 5.9 and Eq. 5.10 can be as the modified version:

$$\lambda_d(i_d, i_q) = L_d(i_d)\, i_d + L_{dq}(i_d, i_q)\, i_q \tag{5.9}$$

$$\lambda_q(i_d, i_q) = L_q(i_q)\, i_q + L_{qd}(i_d, i_q)\, i_d \tag{5.10}$$

Then by collecting the terms with same orders the inductances of the motor can be evaluated as below:

$$\begin{aligned} L_d(i_d) =& \bar{p}_{d00}/i_d + \bar{p}_{d10} + \bar{p}_{d20} i_d + \bar{p}_{d30} i_d^2 \\ L_q(i_q) =& \bar{p}_{q00}/i_q + \bar{p}_{q01} + \bar{p}_{q02} i_q + \bar{p}_{q03} i_q^2 \\ L_{dq}(i_d, i_q) =& \bar{p}_{d01} + \bar{p}_{d11} i_d + \bar{p}_{d02} i_q + \bar{p}_{d21} i_d^2 \\ &+ \bar{p}_{d12} i_d i_q + \bar{p}_{d03} i_q^2 \\ L_{qd}(i_d, i_q) =& \bar{p}_{q10} + \bar{p}_{q11} i_q + \bar{p}_{q20} i_d + \bar{p}_{q21} i_d i_q \\ &+ \bar{p}_{q12} i_q^2 + \bar{p}_{q30} i_d \end{aligned} \tag{5.11}$$

Based on the Eq. 5.11 the $d-$ and $q-$axis inductances can be approximated using polynomial approach. After finding the coefficients of the flux equations the dq maps can be plotted as

Fig. 5.2.

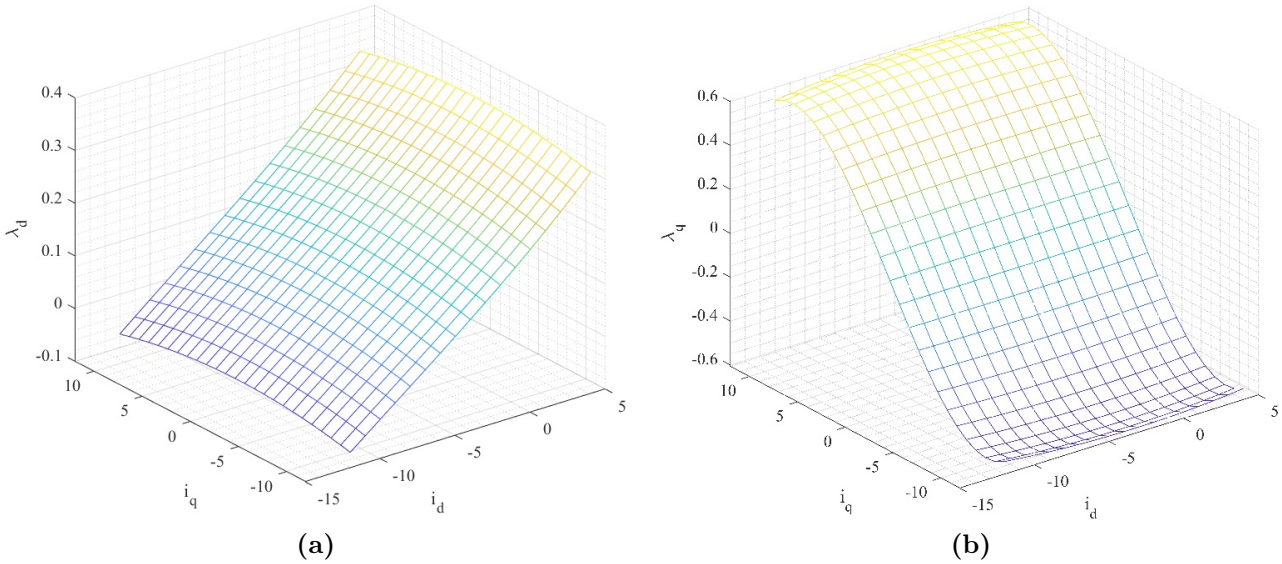

Figure 5.2: $d-$ and $q-$axis flux-linkages maps based on polynomial approximation. (a) for $d-$axis flux-linkage (b) for $q-$axis flux-linkage.

In the next section, a new method is introduced that is more accurate than polynomial method.

5.2 Group Method of Data Handling (GMDH) to Approximate the PMSM Flux-linkage Maps

To start the process in GMDH, the model should have multiple inputs and at least one output. There are partial models in the process where can be updated in each layer and the optimal models will be selected based on the minimum value of the external criterion. On the other hand, GMDH can be described as a multilayered model. It can be expressed as a mathematical model with high order terms lack of instability difficulties. The main idea of the method is detecting a relationship between input and output based on the possible inputs. The network is updated layer by layer during training and optimization. Each layer consists of neurons with two inputs where the output of each neuron is a quadratic function of the best combination of two inputs. The coefficient of these functions is calculated based on linear regression approaches. The previous layer is trained, before switching to a new layer. During training each neuron obtained by two unique combination inputs. On the other hand, input combination selection can be done by best performance. Then for the new layer all this procedure will be repeated. The relation between input and output variables is expressed by a Volterra polynomial series, known as ''Kolmogorov-Gabor" polynomial.

$$y = a_0 + \sum_{n}^{i=1} a_i x_i + \sum_{n}^{i=1} \sum_{n}^{j=1} a_{ij} x_i x_j + ... \tag{5.12}$$

where, x_i is the input of the multi-layer network, m represents the number of the inputs, a_i is the coefficient. Note that a_0 is a constant offset, which can be considered as offset "noise". In this case, the output function of each neuron can be obtained as,

$$y = (x_i, x_j) = a_0 + a_1 x_i + a_2 x_j + a_3 x_i^2 + a_4 x_j^2 + a_5 x_i x_j \tag{5.13}$$

Where, a_0, a_1, a_2, a_3, a_4 and a_6 are the weights coefficients where should be obtained by least squares method for all neurons.

$$A^T = YX^T \tag{5.14}$$

To select the best estimated coefficient and input combinations for each neuron in each layer the Mean Squared Error (MSE) and Root Mean Squared Error (RMSE) are used. Where MSE is the error of the actual and estimated difference over data set and RMSE is the root of MSE that has the same units as the quantity plotted on the vertical axis.

$$MSE = \frac{1}{n}\sum_{n}^{i=1}(\hat{y}_i - y_i)^2 \tag{5.15}$$

$$RMSE = \sqrt{\sum_{n}^{i=1}\frac{(\hat{y}_i - y_i)^2}{n}} \tag{5.16}$$

where $\hat{y}$ is the predicted value, y is the actual value and n is the number of the item. The process of GMDH algorithm implementation can be described as below,

Step1: the actual system's data is divided into training and testing sets in two parts. Training data are used to estimate the weights of GMDH neurons, while checking data are utilized to create the GMDH structure.
Step2: all possible combination of two inputs will be generated; for this motor the inputs are the combinations of i_d and i_q. Then the quadratic polynomial should be expressed by inputs combinations (these equations obtained in the next section, Eq. 5.17 to Eq. 5.24). Then by training data the coefficients of the polynomial function will be obtained by Least Square fitting method.
Step3: the output and data set of the polynomial functions are examined and tested in the third stage. In this location, the regularity criterion for each neuron will be determined. To serve as the new inputs for the next layer, the top-performing neurons are chosen. where the neurons that were not chosen are not included in the network. There are 9 neurons with 54 coefficients and 4 inputs are chosen for the dq approximating flux-linkages for the studied motor. Ignored are two inputs and one neuron.
Step4: all of the steps from steps 2 through 4 are then repeated until the GMDH network is satisfied. When the minimum regularity criterion in the current layer is not less significant than the preceding layer, the procedure will be finished. The selected neurons in each layer

can be used to create the final model of the GMDH; as was described in Step 3, unselected neurons will not be taken into account.

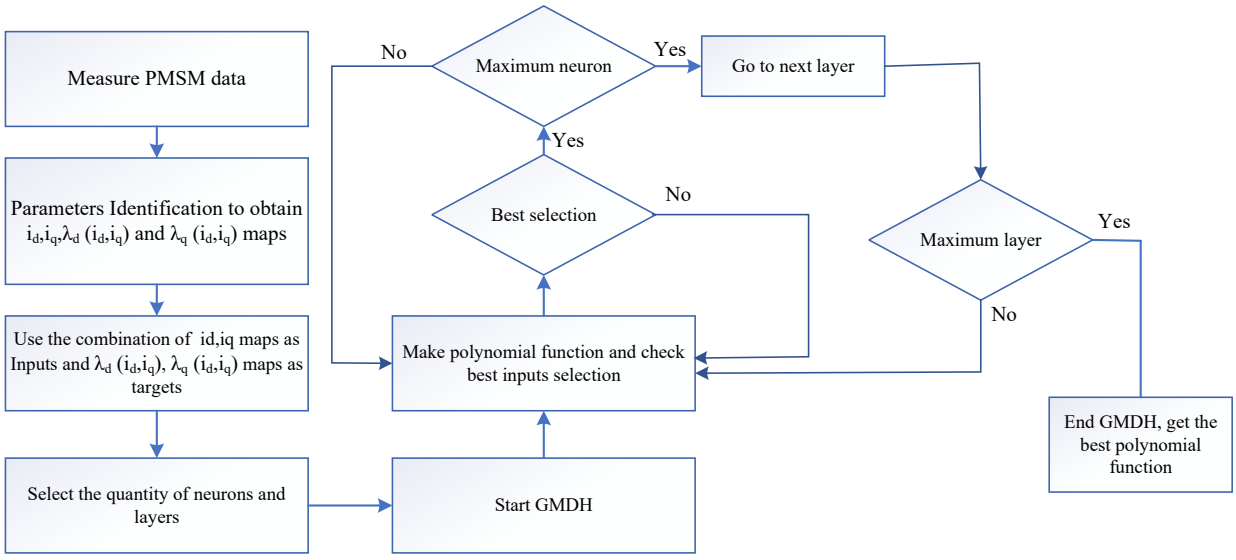

Figure 5.3: Flowchart of the GMDH approximation process.

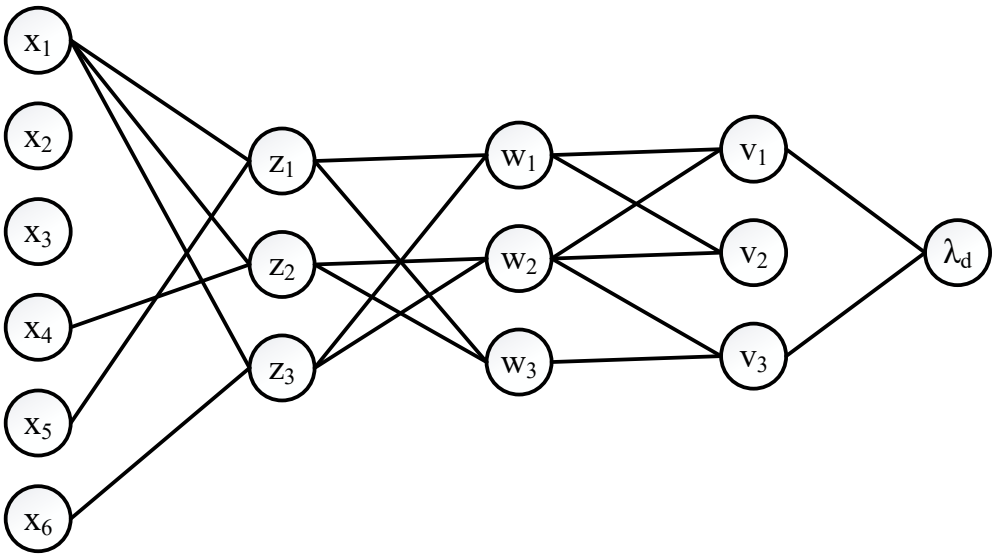

Figure 5.4: GMDH implementation for $d-$axis flux-linkage approximation.

The inputs of the GMDH are selected as $x_1 = i_d$, $x_2 = i_q$, $x_3 = \sqrt{i_d}$, $x_4 = \sqrt{i_q}$, $x_5 = \sqrt{i_d^2 + i_q^2}$ and $x_6 = \arctan i_q/i_d$. In Fig. 5.4 and Fig. 5.5, the structure of GMDH method for $d-$ and $q-$axis flux-linkages are illustrated. The inputs x_1,x_4,x_5,x_6 are selected as the best inputs. In layer 2, 3 and 4 the best selections are, z_1,z_2,z_3,w_1,w_2,w_3,v_1 and v_3 respectively. The inputs x_2 and x_3 and neuron v_2 are not used. Eq. 5.17 to Eq. 5.20 represents the polynomial

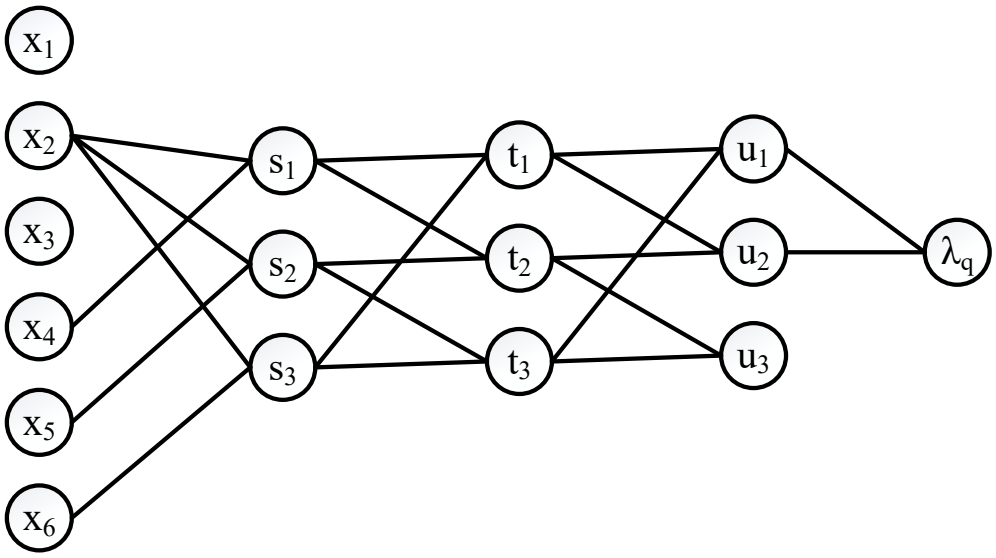

Figure 5.5: GMDH implementation for $q-$axis flux-linkage approximation.

functions of the approximated GMDH model for $d-$axis flux-linkage.

$$\begin{cases} z_1 = a_{0_{11}} + a_{1_{11}}x_1 + a_{2_{11}}x_5 + a_{3_{11}}x_1^2 + a_{4_{11}}x_5^2 + a_{5_{11}}x_1x_5 \\ z_2 = a_{0_{12}} + a_{1_{12}}x_1 + a_{2_{12}}x_4 + a_{3_{12}}x_1^2 + a_{4_{12}}x_4^2 + a_{5_{12}}x_1x_4 \\ z_3 = a_{0_{13}} + a_{1_{13}}x_1 + a_{2_{13}}x_6 + a_{3_{13}}x_1^2 + a_{4_{13}}x_6^2 + a_{5_{13}}x_1x_6 \end{cases} \tag{5.17}$$

$$\begin{cases} w_1 = a_{0_{21}} + a_{1_{21}}z_1 + a_{2_{21}}z_3 + a_{3_{21}}z_1^2 + a_{4_{21}}z_3^2 + a_{5_{21}}z_1z_3 \\ w_2 = a_{0_{22}} + a_{1_{22}}z_2 + a_{2_{22}}z_3 + a_{3_{22}}z_2^2 + a_{4_{22}}z_3^2 + a_{5_{22}}z_2z_3 \\ w_3 = a_{0_{23}} + a_{1_{23}}z_1 + a_{2_{23}}z_2 + a_{3_{23}}z_1^2 + a_{4_{23}}z_2^2 + a_{5_{23}}z_1z_2 \end{cases} \tag{5.18}$$

$$\begin{cases} v_1 = a_{0_{31}} + a_{1_{31}}w_1 + a_{2_{31}}w_2 + a_{3_{31}}w_1^2 + a_{4_{31}}w_2^2 + a_{5_{31}}w_1w_2 \\ v_2 = a_{0_{32}} + a_{1_{32}}w_1 + a_{2_{32}}w_3 + a_{3_{32}}w_1^2 + a_{4_{32}}w_3^2 + a_{5_{32}}w_1z_3 \\ v_3 = a_{0_{33}} + a_{1_{33}}w_2 + a_{2_{33}}w_3 + a_{3_{33}}w_2^2 + a_{4_{33}}w_3^2 + a_{5_{33}}w_2w_3 \end{cases} \tag{5.19}$$

$$\lambda_d = a_{0_{41}} + a_{1_{42}}v_1 + a_{2_{43}}v_3 + a_{3_{44}}v_1^2 + a_{4_{45}}v_3^2 + a_{5_{46}}v_1v_3 \tag{5.20}$$

where x_i,z_i,w_i,z_i are the polynomial functions of each layer. The coefficients shown as $a_{i_{LN}}$ where i, L, N represent number of coefficients, number of layer and number of neurons respectively. As shown in Fig. 5.5, in first layer x_2,x_4,x_5,x_6 are selected as best inputs. In layer 2, 3, 4 and 5 the best selections are s_1,s_2,s_3,t_1,t_2,t_3,u_1,u_2 respectively (inputs x_1 and x_3 and neuron u_3 are not used). The polynomial functions of the approximated GMDH model

for $q-$axis flux-linkage are reported below:

$$\begin{cases} s_1 = b_{0_{11}} + b_{1_{11}}x_2 + b_{2_{11}}x_4 + b_{3_{11}}x_2^2 + b_{4_{11}}x45^2 + b_{5_{11}}x_2x_4 \\ s_2 = b_{0_{12}} + b_{1_{12}}x_1 + b_{2_{12}}x_5 + b_{3_{12}}x_1^2 + b_{4_{12}}x_5^2 + b_{5_{12}}x_1x_5 \\ s_3 = a_{0_{13}} + b_{1_{13}}x_2 + b_{2_{13}}x_6 + b_{3_{13}}x_2^2 + b_{4_{13}}x_6^2 + b_{5_{13}}x_2x_6 \end{cases} \tag{5.21}$$

$$\begin{cases} t_1 = b_{0_{21}} + b_{1_{21}}s_1 + b_{2_{21}}s_3 + b_{3_{21}}s_1^2 + b_{4_{21}}s_3^2 + b_{5_{21}}s_1s_3 \\ t_2 = b_{0_{22}} + b_{1_{22}}s_1 + b_{2_{22}}s_2 + b_{3_{22}}s_1^2 + b_{4_{22}}s_1^2 + b_{5_{22}}s_1s_2 \\ t_3 = b_{0_{23}} + b_{1_{23}}s_2 + b_{2_{23}}s_3 + b_{3_{23}}s_2^2 + b_{4_{23}}s_3^2 + b_{5_{23}}s_2s_3 \end{cases} \tag{5.22}$$

$$\begin{cases} u_1 = b_{0_{31}} + b_{1_{31}}t_1 + b_{2_{31}}t_3 + b_{3_{31}}t_1^2 + b_{4_{31}}t_3^2 + b_{5_{31}}t_1t_3 \\ u_2 = b_{0_{32}} + b_{1_{32}}t_1 + b_{2_{32}}t_2 + b_{3_{32}}t_1^2 + b_{4_{32}}t_2^2 + b_{5_{32}}t_1t_2 \\ u_3 = b_{0_{33}} + b_{1_{33}}t_2 + b_{2_{33}}t_3 + b_{3_{33}}t_2^2 + b_{4_{33}}t_3^2 + b_{5_{33}}t_2t_3 \end{cases} \tag{5.23}$$

$$\lambda_q = b_{0_{41}} + b_{1_{42}}u_1 + b_{2_{43}}u_2 + b_{3_{44}}u_1^2 + b_{4_{45}}u_2^2 + b_{5_{46}}u_1u_2 \tag{5.24}$$

The GMDH flux-linkages maps are presented in Fig. 5.6 based on the Eq. 5.20 and Eq. 5.24.

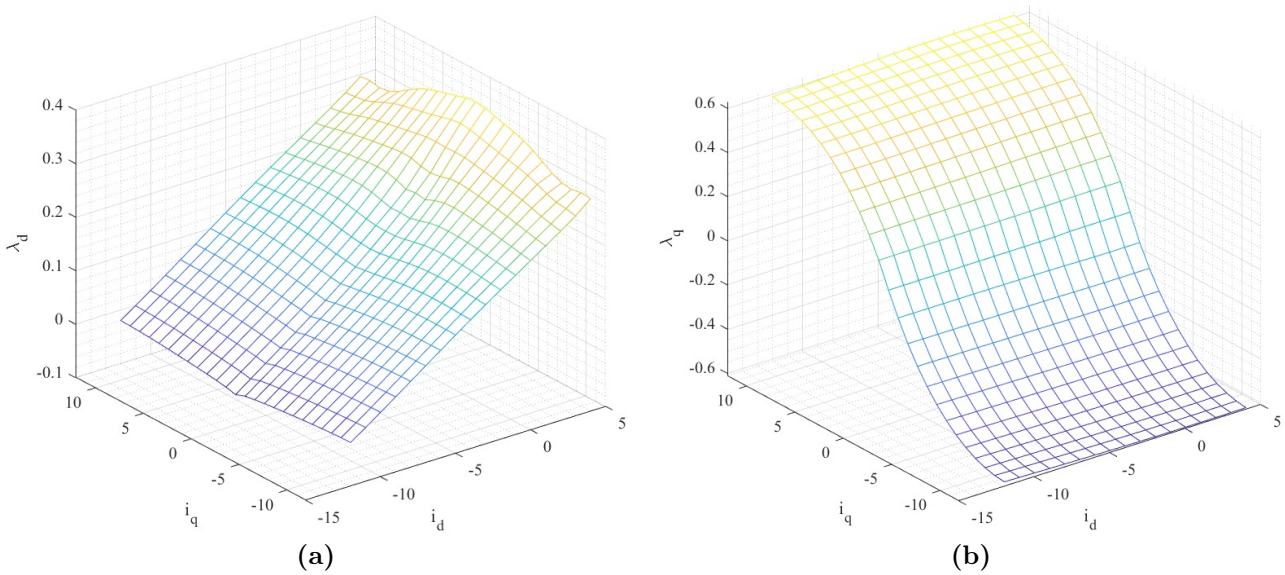

Figure 5.6: $d-$ and $q-$axis flux-linkages maps based on GMDH approximation. (a) for $d-$axis flux-linkage(b) for $q-$axis flux-linkage.

5.3 Results

To investigate the accuracy of the GMDH method, flux-linkage estimation error (difference between the actual value and the estimated value), error histogram (histogram of the errors

between target values and predicted values after training in GMDH) and linear regression scatter plot (statistical relationship between actual and approximated flux-linkage) are presented in this section. Fig. 5.7a and Fig. 5.7b illustrate the estimation error and error histogram of the $d-$axis flux-linkage, respectively.

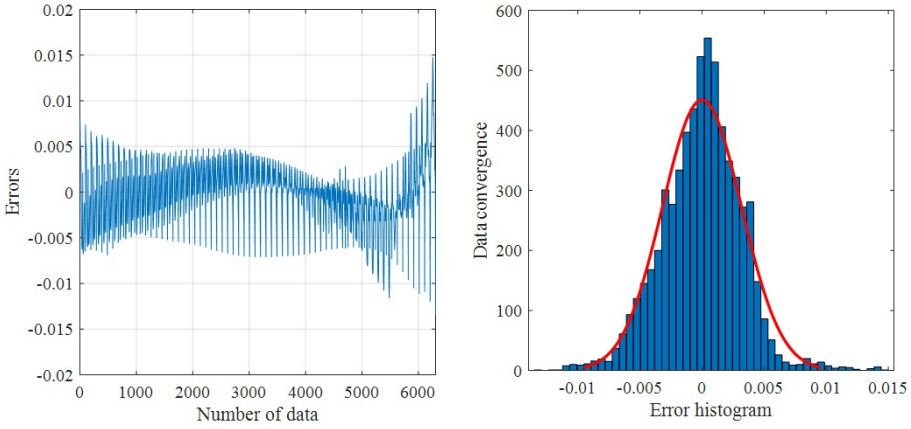

(a) **(b)**

Figure 5.7: (a) flux-linkage estimation error and (b) error histogram of GMDH learning and optimization for $d-$axis flux-linkage.

Fig. 5.8a and Fig. 5.8b illustrate the estimation error and error histogram of the $q-$axis flux-linkage, respectively. The linear regression scatter plot for $d-$ and $q-$axis flux-linkage

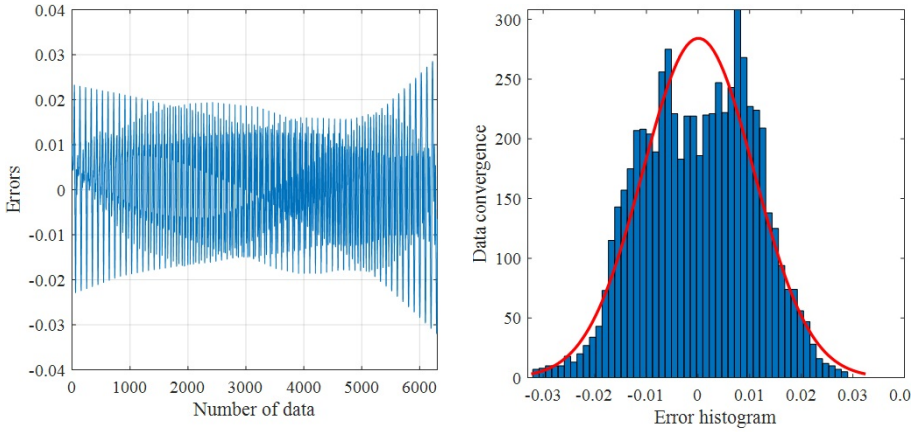

(a) **(b)**

Figure 5.8: (a) flux-linkage estimation error and (b) error histogram of GMDH learning and optimization for $q-$axis flux-linkage.

are presented in Fig. 5.9a and Fig. 5.9b. The results indicated low RMSE (defined as in Eq. 5.15), i.e. 0.02 and high linearity, $R > 0.999$ for $d-$axis flux-linkage. For $q-$axis flux-linkage, the RMSE and linearity are 0.02 and 0.999.

The approximated flux-linkage maps are presented based on the $d-$ and $q-$axis currents (Fig. 5.1, Fig. 5.2 and Fig. 5.6). Fig. 5.6a and Fig. 5.6b are obtained by GMDH and Fig. 5.2a and Fig. 5.2b are the maps based on the polynomial approximation [76]. The error

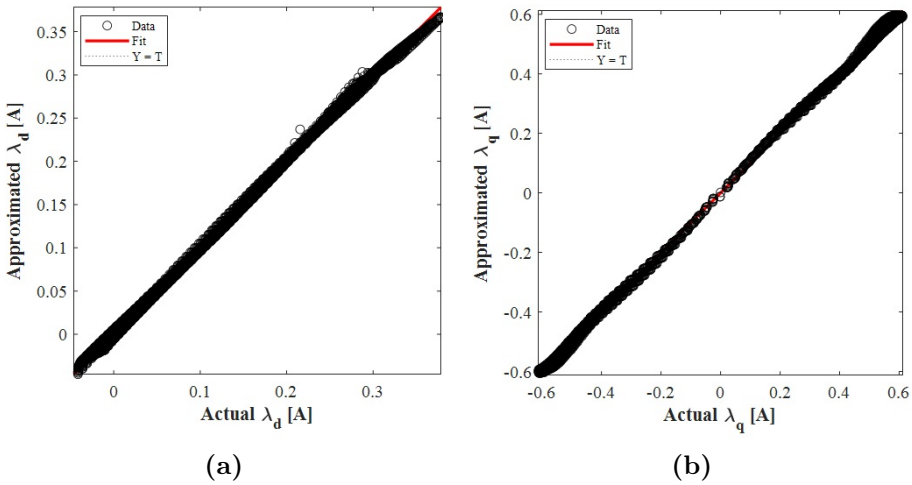

Figure 5.9: Linear regression scatter plot of GMDH method. (a) for $d-$axis flux-linkage approximation (b) for $q-$axis flux-linkage approximation.

of the whole flux-linkage map for GMDH and polynomial approximations versus LUT arre presented in Fig. 5.10 and Fig. 5.11. As a results, the $d-$axis flux-linkage error for GMDH method and polynomial one is 5.8% and 15%, respectively. And, it is 3.8% and 5.2% for the $q-$axis flux-linkages. These results show that the GMDH method achieves better accuracy with respect to the polynomial method. The GMDH memory occupation is also lower than LUT methods with similar accuracy. Moreover, the availability of an analytical expression for approximating the flux maps is useful for off-line work.

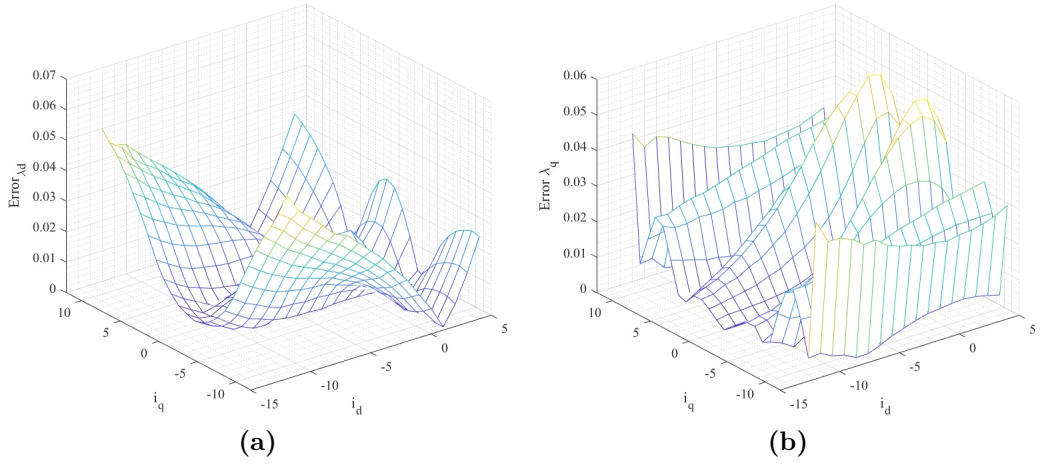

Figure 5.10: (a) λ_d actual and approximated error between LUT and polynomial Approximation (b) λ_q actual and approximated error between LUT and polynomial Approximation.

5.4 Conclusion

GMDH method is presented in this chapter to approximate the flux-linkages of the IPMSM. Using this method can be done online where the inputs are the dq axis currents. The

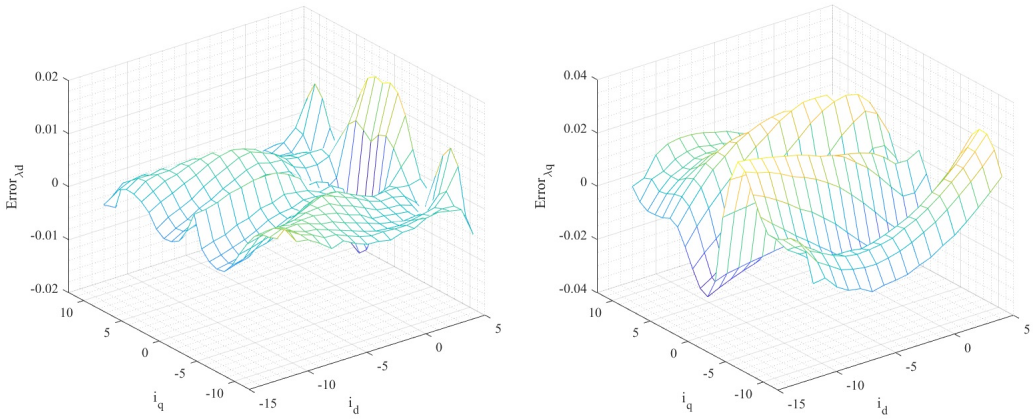

Figure 5.11: (a) λ_d actual and approximated error between LUT and GMDH approximation (b) λ_q actual and approximated error between LUT and GMDH approximation.

method is compared with a polynomial method. The simulation results confirm that the accuracy of GMDH is higher than polynomial method due to error percentage. Based on the results the error percentage for $d-$ and $q-$axis flux-linkages using GMDH is less 3 times and 2 times respectively compare to polynomial approximation method. The GMDH method approximate the flux-linkages maps of IPMSM (achieving approximately half the RMSE error, Table I), while polynomial methods are accurate only for SynRM.
As the future work, the GMDH method can be used for SynRM motor to approximate the flux maps. Furthermore, the approximated flux maps cab be applied to the controller instead of constant value of the motor parameters or LUT.

Chapter 6

Advances on Analysis, Modeling and Accurate Self Commissioning Compensation of Inverter Dead-Time Distortion Based on a Physical Model

In this chapter, a novel approach on dead-time compensation for the inverter controller, which plays an important role in enhancing the performance of the motor drive system is presented. The non-linearity effects in voltage source inverters are primarily caused by dead-times, voltage drops, and the parasitic and intrinsic capacitive effects of power devices and electric machines. Accurate compensation of these effects is crucial in many drives applications, as output voltage distortion can greatly impact the performance of the current control loop, particularly at low speeds where the operating voltage of the machine is similar to the level of distortion introduced by non-linearity components.

This is of even greater concern in sensorless systems where low-speed performance is highly dependent on accurate knowledge of the machine's feeding voltage, which is not directly measured. As a result, inverter non-linearity effects are introduced into the estimation loop, degrading the reliability and accuracy of the estimates.

Most compensation techniques in the literature employ a voltage-to-current characteristic to approximate non-linearity effects and are identified during a self-commissioning procedure. Some approaches use different correcting functions, such as linear saturation, [50], sigmoid, [51], exponential, [52], while others require external tuning to adapt the compensation function to the commercial drive. Some methods use current sensors or references to determine current direction, while others use extra hardware for zero-crossing detection.

Recently, a novel approach has been introduced where an analytical model of the physical behavior of the inverter non-linearities is considered and a proper test procedure is performed to self-identify the critical parameters of the model [57]. This approach involves autonomous selection of the threshold current of the measured voltage-to-current characteristics, which is necessary for accurate estimation and compensation of the non-linearity effects. In this

chapter, two new methods that assure minimal error estimation and demonstrate their superiority over state-of-the-art approaches is presented [77]. Additionally, for the first time the effects of inverter distortion on the accuracy of current sampling and control loops and propose an original compensation strategy is analyzed. Theoretical analysis and developments, along with simulations and experimental results based on a commercial drive, are fully reported.

6.1 Accurate Modeling of Inverter Distortion

The inverter output voltage characteristics are influenced by the non-ideal behavior of the commutation phenomena, such as dead-time effect, commutation delays, voltage drops in power devices, equivalent parasitic resistance and inductance of the current paths, charging and discharging of the equivalent (parasitic or intrinsic) output capacitance of the leg. For this reason the inverter instantaneous output voltage with respect to the DC bus reference level, i.e. V_{x0} in Fig. 6.1, will be considered in the following analysis. Averaging and extension to the phase voltage of the three-phase load will be considered as a consequence. The inductive behavior of the load allows to model the leg output current as a constant value during the switching period or, at least, during the dead-time intervals, as it will be explained shortly. A first model will be considered, which takes into account the recalled non-ideal conditions, but neglects the effects of the output capacitance. Later, those effects will be introduced and a complete model obtained. The simplified version of that model represents the base for the proposed self commissioning and compensation strategy, discussed in the next sections.

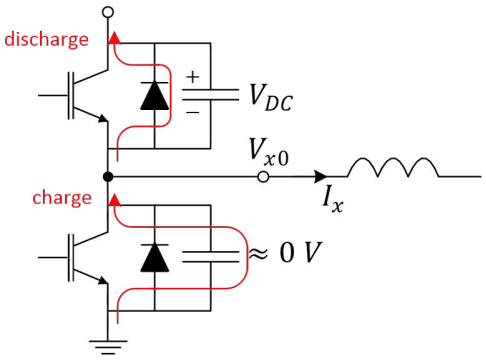

Figure 6.1: Charging and discharging switch capacitance during lower IGBT switching off.

6.1.1 Dead-time and switch voltage drops effects

The output voltage waveforms during dead time interval (T_{DT}) when considering voltage drops (V_{IGBT} and V_{diode}) and switching delays ($T_{delay,H\to L}$ and $T_{delay,L\to H}$) are sketeched in Fig. 6.2. Two different cases have been considered, as a function of the sign of the output current, which affects the conduction state of the free-wheeling diodes and thus the output

voltage.

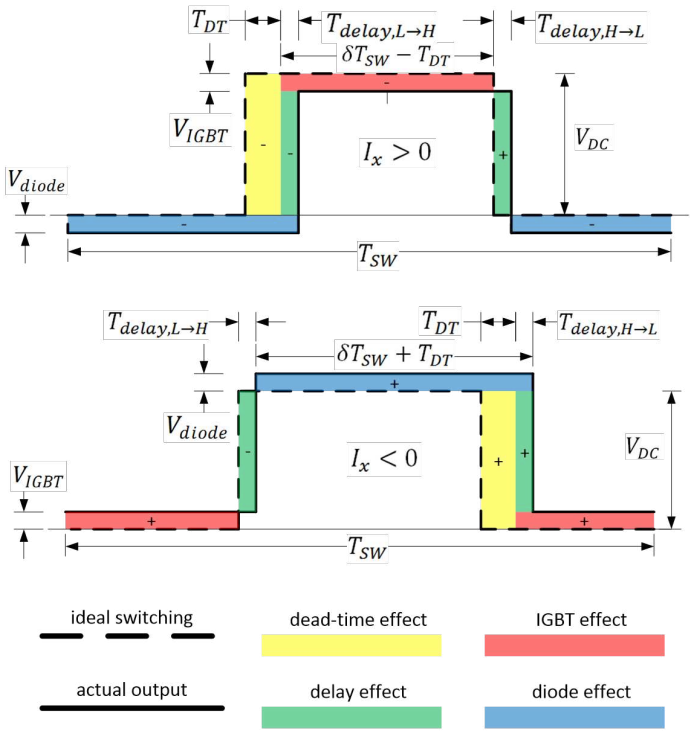

Figure 6.2: Output voltage waveforms during dead time when considering voltage drops and switching delays.

The voltage difference (increase or decrease) between ideal (dashed black lines) and actual switchings (solid black lines) are highlighted by coloured areas and identified by + and − signs, meaning that the corresponding contribution respectively increases or decreases the output voltage averaged over the switching period T_{SW}. In the following sections the term $\bar{V}_{x0_{DT}} = \bar{V}_{x0} - \bar{V}^*_{x0}$ that represents distortion of the inverter output voltage will be referred to as "distortion voltage". Symmetric commutation delays (if any) are considered with green areas, their average contribution being generally zero due to symmetry. Asymmetric commutation delays can be considered as additional dead-time components and are therefore included in that value, represented with yellow areas. Finally IGBT and diode contributions are represented with red and blue areas.
The equivalent on-time of the output voltage can be therefore related to the commanded duty cycle δ_x and the dead-time, as shown in the same figure. If the average value of the output voltage is considered within the switching period, the following equations are obtained for distortion voltage as a function of the output current sign:

$$I_x > 0 : \overline{V}_{x0_{\mathrm{DT}}} = \frac{1}{T_{SW}} \left\{ -\underbrace{V_{DC} T_{DT}}_{\cdot} - \underbrace{V_{IGBT} \left(\delta_x T_{SW} - T_{DT}\right)}_{\cdot} - \underbrace{V_{diode} \left[(1-\delta_x) T_{SW} + T_{DT}\right]}_{\cdot} \right\} \tag{6.1}$$

$$I_x<0:\overline{V}_{x0_{\mathrm{DT}}}=\frac{1}{T_{SW}}\left\{\underbrace{V_{DC}T_{DT}}_{\square}+\underbrace{V_{IGBT}\left[(1-\delta_x)\,T_{SW}-T_{DT}\right]}_{\square}-\underbrace{V_{diode}\left(\delta_x T_{SW}+T_{DT}\right)}_{\square}\right\} \tag{6.2}$$

Previous equations can be manipulated after the introduction of the following equation relating the IGBT and diode voltage drops:

$$V_{IGBT}=V_{diode}+\Delta V \tag{6.3}$$

thus obtaining this:

$$\begin{aligned} I_x>0: &\quad \overline{V}_{x0_{\mathrm{DT}}}=-V_{DC}\tfrac{T_{DT}}{T_{SW}}-V_{diode}-\Delta V\left(\delta_x-\tfrac{T_{DT}}{T_{SW}}\right)\\ I_x<0 &: \overline{V}_{x0_{DT}}=V_{DC}\tfrac{T_{DT}}{T_{SW}}+V_{diode}+\Delta V\left(1-\delta_x-\tfrac{T_{DT}}{T_{SW}}\right)\end{aligned} \tag{6.4}$$

In the case of small phase voltage (i.e. $\delta_x \cong 0.5$), a first symplified equation can be obtained

$$\overline{V}_{x0_{\mathrm{DT}}}=-\mathrm{sign}\left(I_x\right)\left[V_{DC}\frac{T_{DT}}{T_{SW}}+V_{diode}+\Delta V\left(0.5-\frac{T_{DT}}{T_{SW}}\right)\right] \tag{6.5}$$

If dead-time interval is small with respect to switching period, the very last term of Eq. 6.5 can be neglected, leading to

$$\bar{V}_{x0_{DT}}=-sign\left(I_x\right)\left(V_{DC}\frac{T_{DT}}{T_{SW}}+V_{diode}+0.5\;\Delta V\right) \tag{6.6}$$

6.1.2 Introducing the effect of capacitance

The adopted full model comprises parasitic capacitance charging effect, [78] [79] [80] [81]. During the dead-time interval the output current tends to force a commutation due to the turn on of the opposite diode. One of the possible situations is sketched in Fig. 6.1, where switching off of the low-side IGBT is considered. The output current is negative (i.e. entering the output node) and initial voltage is equal to the lower IGBT voltage drop. Due to the presence of the switch capacitance, output voltage does not rise immediately, as the upper capacitance has to be discharged and lower one charged.
Four different cases can be considered as a function of the sign and the absolute value of the output current, as depicted in Fig. 6.3.

In fact, if the time required to charge/discharge the output capacitance is higher than the dead-time interval (i.e. when the output current is quite low), the commutation is slower and a discontinuity is experienced in the output voltage as soon as the higher IGBT switches on at the end of the dead-time interval. The limit condition between the ideal ramp transition and intermediate lower slope cases can be calculated by matching the charge and discharge time and dead-time. If the IGBT and diode voltage drops are taken into account, this results in

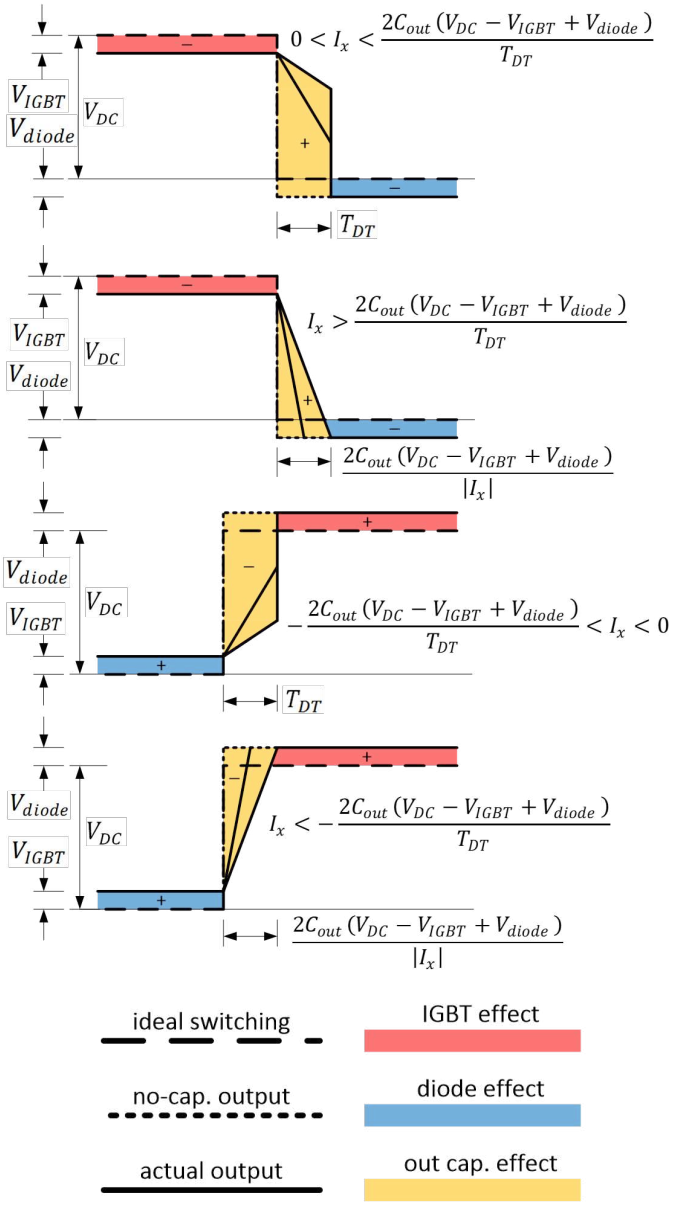

Figure 6.3: Output voltage waveforms during dead time when considering output capacitance and different values of the output current.

$$I_x = \frac{2C_{out}\left(V_{DC} - V_{IGBT} + V_{diode}\right)}{T_{DT}} \tag{6.7}$$

where C_{out} is the overall output capacitance. The difference between the areas in Fig. 6.2, i.e. null capacitance, and that of Fig. 6.3 are then considered, and four expressions are obtained as a function of the output current:

$$\begin{gathered} if \quad 0 < I_x < \frac{2C_{out}(V_{DC}-V_{IGBT}+V_{diode})}{T_{DT}} \\ \bar{V}_{x0cap} = \frac{1}{T_{SW}}\left\{\left(V_{DC} - V_{IGBT} + V_{diode}\right)T_{DT} - \frac{|I_x|}{4C_{out}}T_{DT}^2\right\} \end{gathered} \tag{6.8}$$

$$\begin{gathered} if \quad I_x > \frac{2C_{out}(V_{DC}-V_{IGBT}+V_{diode})}{T_{DT}} \\ \bar{V}_{x0cap} = \frac{1}{T_{SW}}\left\{\frac{C_{out}(V_{DC}-V_{IGBT}+V_{diode})^2}{|I_x|}\right\} \end{gathered} \tag{6.9}$$

$$\begin{gathered} if \quad -\frac{2C_{out}(V_{DC}-V_{IGBT}+V_{diode})}{T_{DT}} < I_x < 0 \\ \bar{V}_{x0cap} = \frac{1}{T_{SW}}\left\{-\left(V_{DC} - V_{IGBT} + V_{diode}\right)T_{DT} + \frac{|I_x|}{4C_{out}}T_{DT}^2\right\} \end{gathered} \tag{6.10}$$

$$\begin{gathered} if \quad I_x < -\frac{2C_{out}(V_{DC}-V_{IGBT}+V_{diode})}{T_{DT}} \\ \bar{V}_{x0cap} = \frac{1}{T_{SW}}\left\{-\frac{C_{out}(V_{DC}-V_{IGBT}+V_{diode})^2}{|I_x|}\right\} \end{gathered} \tag{6.11}$$

representing the contribution of the output capacitance to average output voltage distortion $\bar{V}_{x0}$.

Finally the two contributions, i.e. the last four equations and those calculated in Eq. 6.1, Eq. 6.2 can be joined to obtain the overall average distortion voltage in the different current conditions, as reported in the following equations:

$$\begin{gathered} if \quad 0 < I_x < \frac{2C_{out}(V_{DC}-V_{IGBT}+V_{diode})}{T_{DT}} \\ \bar{V}_{x0} = \frac{1}{T_{SW}}\left\{V_{DC}\delta_x T_{SW} - V_{DC}T_{DT} - V_{IGBT}\left(\delta_x T_{SW} - T_{DT}\right.\right. \\ \left.\left. -V_{diode}\left[\left(1-\delta_x\right)T_{SW} + T_{DT}\right] + \left(V_{DC} - V_{IGBT} + V_{diode}\right)T_{DT} - \frac{|I_x|}{4C_{out}}T_{DT}^2\right. \end{gathered} \tag{6.12}$$

$$\begin{gathered} if \quad I_x > \frac{2C_{out}(V_{DC}-V_{IGBT}+V_{diode})}{T_{DT}} \\ \bar{V}_{x0} = \frac{1}{T_{SW}}\left\{V_{DC}\delta_x T_{SW} - V_{DC}T_{DT} - V_{IGBT}\left(\delta_x T_{SW} - T_{DT}\right.\right. \\ \left.\left. -V_{diode}\left[\left(1-\delta_x\right)T_{SW} + T_{DT}\right] + \frac{C_{out}(V_{DC}-V_{IGBT}+V_{diode})^2}{|I_x|}\right. \end{gathered} \tag{6.13}$$

$$\begin{gathered} if \quad -\frac{2C_{out}(V_{DC}-V_{IGBT}+V_{diode})}{T_{DT}} < I_x < 0 \\ \bar{V}_{x0} = \frac{1}{T_{SW}}\left\{V_{DC}\delta_x T_{SW} + V_{DC}T_{DT} + V_{IGBT}\left[\left(1-\delta_x\right)T_{SW} - T_{DT}\right]\right. \\ \left. +V_{diode}\left(\delta_x T_{SW} + T_{DT}\right) - \left(V_{DC} - V_{IGBT} + V_{diode}\right)T_{DT} + \frac{|I_x|}{4C_{out}}T_{DT}^2\right. \end{gathered} \tag{6.14}$$

$$\begin{gathered} if \quad I_x < -\frac{2C_{out}(V_{DC}-V_{IGBT}+V_{diode})}{T_{DT}} \\ \bar{V}_{x0} = \frac{1}{T_{SW}}\left\{V_{DC}\delta_x T_{SW} + V_{DC}T_{DT} + V_{IGBT}\left[\left(1-\delta_x\right)T_{SW} - T_{DT}\right]\right. \\ \left. +V_{diode}\left(\delta_x T_{SW} + T_{DT}\right) - \frac{C_{out}(V_{DC}-V_{IGBT}+V_{diode})^2}{|I_x|}\right. \end{gathered} \tag{6.15}$$

6.2 Model Simplification: Calculation of Phase Voltage Distortion

The model introduced above can be greatly simplified under the following hypotheses:
•$\delta_x \approx 0.5$ (small phase voltage);
•$T_{DT} \ll \delta_x T_{SW}$ (small phase voltage and dead-time);
•$V_{IGBT} \ll V_{DC}$ (small IGBT voltage drop);
•$V_{diode} \ll V_{DC}$ (small diode voltage drop).
obtaining the following expressions for the leg output voltage:

$$\begin{gathered} if \quad |I_x| < \frac{2C_{out}V_{DC}}{T_{DT}} \\ \bar{V}_{x0} = V_{DC}\delta_x - sign\,(I_x)\ V_{SW}\ - \frac{T_{DT}^2}{4C_{out}T_{SW}} I_x \end{gathered} \tag{6.16}$$

$$\begin{gathered} if \quad |I_x| > \frac{2C_{out}V_{DC}}{T_{DT}} \\ \bar{V}_{x0} = V_{DC}\delta_x - sign\,(I_x)\ V_{DC}\frac{T_{DT}}{T_{SW}} \\ -sign\,(I_x)\ V_{SW}\ + C_{out}V_{DC}2T_{SW}\frac{1}{I_x} \end{gathered} \tag{6.17}$$

The distortion voltage curve represented by this model is shown in Fig. 6.4. It is worth to mention that the small phase voltage condition (i.e. $\delta_x \approx 0.5$) represents indeed the situation in which inverter distortion compensation is mostly needed. Distortion voltage component can be therefore expressed as a function of:
- three parameters, i.e. T_{DT}, C_{out} and the average value of the two devices voltage drops $V_{SW} = \frac{V_{IGBT}+V_{diode}}{2}$;
-two variables, i.e. I_x and V_{DC}; both are measured, the second one is slowly varying and belongs to a limited range, therefore it can be considered as a known parameter.
As it can be seen both from the above equations and in Fig. 6.4, the presence of output capacitance influences the shape (slope, in particular) of the distortion voltage vs. current characteristic, while the asymptotic value at high current is proportional to T_{DT}.
Hereafter the distortion on phase voltage will be evaluated for a particular case, i.e. considering the injection of a controlled current space vector along the phase a of the motor. As it will be shown, this situation is particularly convenient for the sake of parameters identification, and represents a significant case since standard experimental tests for dead time distortion characteristic are normally referred to it.
Due to the particular choice of the current space vector the following trivial condition holds:

$$I_b = I_c = -\frac{I_a}{2} \tag{6.18}$$

which allows to calculate all the voltage distortion components as a function of the same current I_a. Three different conditions have to be considered, i.e. the current is below (i.e. "low-current") the threshold $I_{thr} = \frac{2C_{out}V_{DC}}{T_{DT}}$, above twice the same threshold (i.e. "high-

current") or intermediate:

$$\begin{gathered} if \quad |I_a| < I_{thr} \\ \bar{V}_{a0_{DT}} = -sign\,(I_a)\ V_{SW}\ - \frac{T_{DT}^2}{4C_{out}T_{SW}} I_a \\ \bar{V}_{b0_{DT}} = \bar{V}_{c0_{DT}} = sign\,(I_a)\ V_{SW}\ + \frac{1}{2}\ \frac{T_{DT}^2}{4C_{out}T_{SW}} I_a \end{gathered} \tag{6.19}$$

$$\begin{gathered} if \quad I_{thr} < |I_a| < 2I_{thr} \\ \bar{V}_{a0_{DT}} = -sign\,(I_a)\ V_{DC}\frac{T_{DT}}{T_{SW}}\ - sign\,(I_a)\ V_{SW}\ + \frac{C_{out}{V_{DC}}^2}{T_{SW}}\frac{1}{I_a} \\ \bar{V}_{b0_{DT}} = \bar{V}_{c0_{DT}} = sign\,(I_a)\ V_{SW} + \frac{1}{2}\ \frac{T_{DT}^2}{4C_{out}T_{SW}} I_a \end{gathered} \tag{6.20}$$

$$\begin{gathered} if \quad |I_a| > 2I_{thr} \\ \bar{V}_{a0_{DT}} = -sign\,(I_a)\ V_{DC}\frac{T_{DT}}{T_{SW}}\ - sign\,(I_a)\ V_{SW}\ + \frac{C_{out}{V_{DC}}^2}{T_{SW}}\frac{1}{I_a} \\ \bar{V}_{b0_{DT}} = \bar{V}_{c0_{DT}} = sign\,(I_a)\ V_{DC}\frac{T_{DT}}{T_{SW}} + sign\,(I_a)\ V_{SW} - \frac{C_{out}{V_{DC}}^2}{T_{SW}}\frac{2}{I_a} \end{gathered} \tag{6.21}$$

Motor phase voltage can be finally calculated by considering a balanced condition and the relationship between inverter output leg voltage V_{x0} and neutral point voltage V_{n0}, i.e. $V_{xn} = V_{x0} - V_{n0}$, where $V_{n0} = \frac{V_{a0}+V_{b0}+V_{c0}}{3}$.
Both for "high" and "low" currents the dependence of distortion voltage on current is quite straightforward and is similar to that of leg voltage, but in the intermediate range both the effects are in some way superimposed, meaning that a relatively accurate knowledge of the involved parameters is needed for a proper compensation. Through experimental verification it was finally highlighted that the effect of the devices voltage drops V_{SW} can be neglected, [79], and previous equations can be further simplified. If a balanced resistive load (e.g. the motor windings in DC) is considered, phase voltage reference available at the output of the vector control algorithm is:

$$\bar{V}_{an}^* = \bar{V}_{an} - \hat{V}_{an_{DT}} = R_S I_a - \hat{V}_{an_{DT}} \tag{6.22}$$

which, according to the simplified model, becomes:

$$\begin{gathered} if \quad |I_a| < I_{thr} \\ \bar{V}_{an}^* = \quad \frac{T_{DT}^2}{4C_{out}T_{SW}} I_a + R_S I_a \end{gathered} \tag{6.23}$$

$$\begin{gathered} if \quad I_{thr} < |I_a| < 2I_{thr} \\ \bar{V}_{an}^* = \frac{2}{3} sign\,(I_a)\ V_{DC}\frac{T_{DT}}{T_{SW}} \\ -\frac{2}{3}\frac{C_{out}{V_{DC}}^2}{T_{SW}}\frac{1}{I_a} + \frac{1}{3}\frac{T_{DT}^2}{4C_{out}T_{SW}} I_a + R_S I_a \end{gathered} \tag{6.24}$$

$$\begin{gathered} if \quad |I_a| > 2I_{thr} \\ \bar{V}_{an}^* = \frac{4}{3} sign\,(I_a)\ V_{DC}\frac{T_{DT}}{T_{SW}} - 2\frac{C_{out}{V_{DC}}^2}{T_{SW}}\frac{1}{I_a} + R_S I_a \end{gathered} \tag{6.25}$$

In Fig. 6.5 a graphical representation of the phase voltage reference (solid line) and its distortion component (dashed line) as a function of the output current is shown for a typical case. It can be seen that a linear saturated model can roughly approximate the curve, since in the leftmost part of the diagram (i.e. "low" current) the dependence is linear, whilst

in the rightmost part (i.e. "high" current) a constant term prevails. This also explains the conventional approaches to dead-time compensation by piece-wise linear saturated functions.

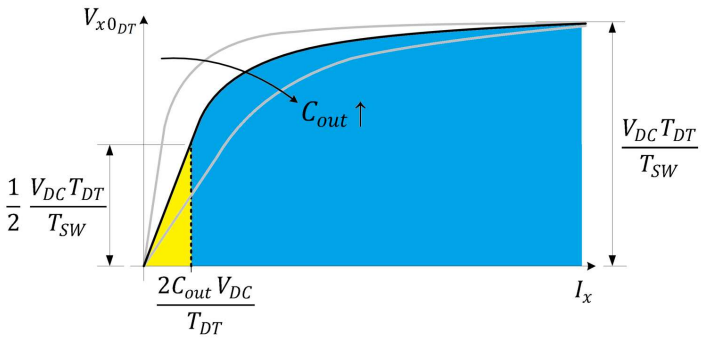

Figure 6.4: Simplified curve of phase leg distortion voltage.

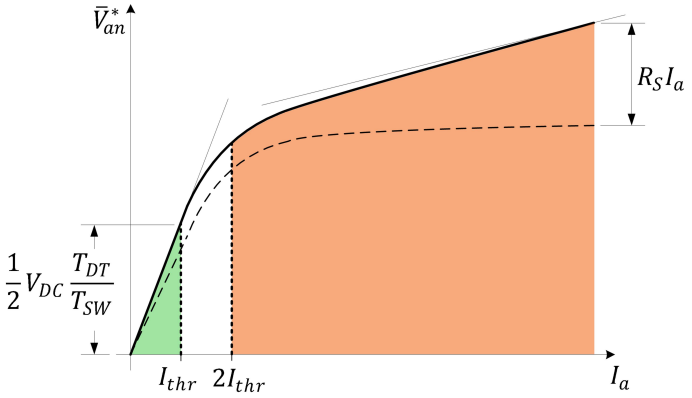

Figure 6.5: Phase voltage reference vs. current curve in the commissioning conditions.

6.3 Analytical modeling of non linearities due to dead-time

In an ideal inverter, there is a simple relationship between the duty cycle and the average leg voltage in a switching period. This means that the desired (reference) voltage produced by the current controller is perfectly actuated, by means of the chosen modulation strategy. If non-linearities due to dead-time are considered, this is no longer the case. In Fig. 6.6, the comparison between a simulation and an experimental test is shown, the experiment is performed by injecting a current space vector with a slowly increasing staircase amplitude along the -axis and measuring the corresponding reference voltage produced by the current regulation loop. When the electrical system reaches each steady state condition, the output values of the current regulators are sampled and stored together with the corresponding reference value. These last are equally distributed from zero to the rated value of the machine current. The only noticeable difference between the two curves lies in the very

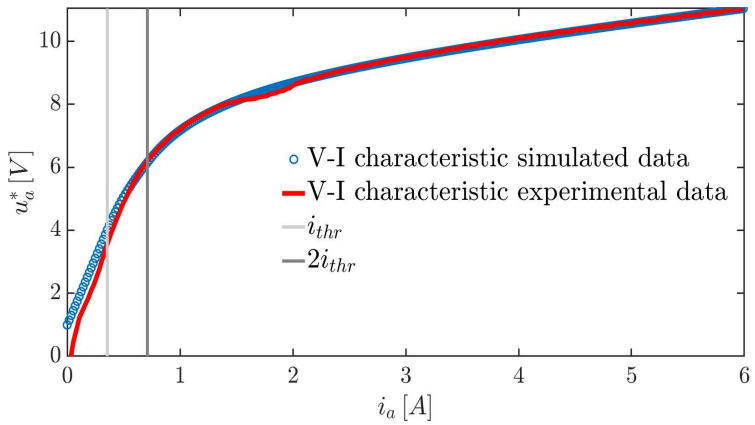

Figure 6.6: Simulated and experimental V-I inverter characteristic.

low current region. Here, the switching devices behavior and capacitance value cannot be assumed constant (being the assumption of the simulation), leading to the presence of a difference between the two results. The inverter output leg voltage depends in fact on the charging state of the parasitic capacitor (due to both the power switches and systems overall capacitive effects), which affects the voltage transition during the dead time, as shown in Fig. 6.7. From the image, the definition of threshold current can be retrieved, i.e. the value needed to fully discharge the equivalent capacitance during dead-time. Indeed, the time integral of the actual leg output current should be considered, i.e. the overall charge stored in the capacitance. A common simplifying hypothesis is to consider a constant leg output current, thus allowing to define the voltage transition behavior as a function of the current value only. Two cases are illustrated, when the current is smaller than the threshold value

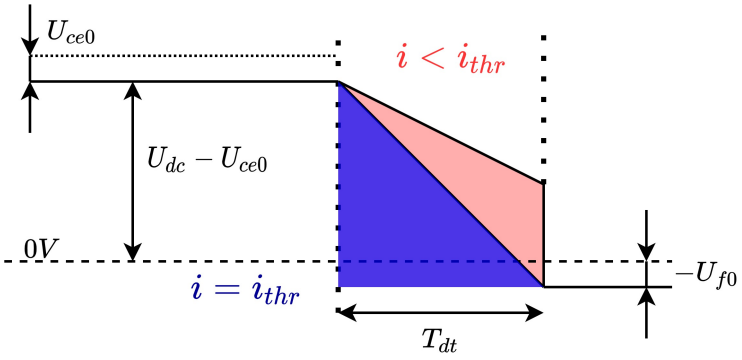

Figure 6.7: Leg output voltage during dead-time discharging (positive current).

(pink curve) and the node does not have enough time to fully discharge during dead-time, and current equal to the threshold value, when the node discharges completely (blue curve). The measured distortion function shows a voltage dip (right below 2A) that is not included in the analytical model hereby presented. A study validated by simulation results relates this phenomenon to the variability of the device capacitance. The capacitance value is almost constant in all the voltage ranges, except for low voltages, where due to a small V_{CE} (or V_{DS}) change a big difference in output capacitance is experienced, as shown in Fig. 6.8,

where the typical capacitances to voltage characteristics of a commercial power MOSFET is reported. By simulating the output capacitance change as a function of the leg voltage, e.g.

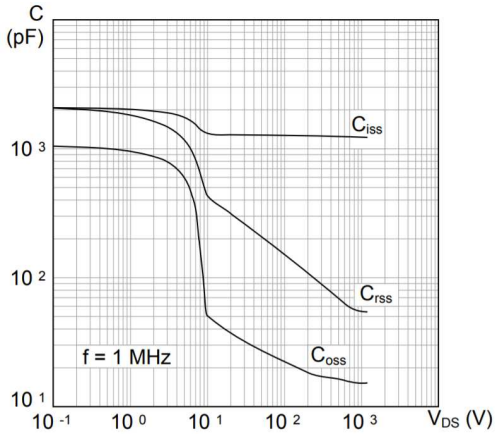

Figure 6.8: Typical MOSFET capacitances as a function of drain-source voltage.

adopting a piecewise linear (PWL) approximation of the capacitance value as a function of its applied voltage, the voltage dip effect can be obtained also in the simulation results, as demonstrated in the results of Fig. 6.9. The comparison of the blue (simulation with PWL

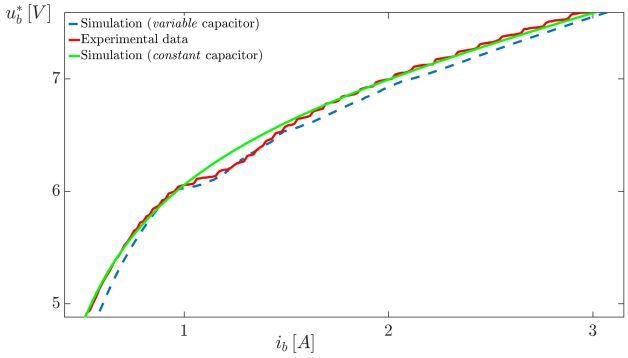

Figure 6.9: Voltage-to-current characteristics: simulation with constant and variable capacitance (green and blue, respectively), experimental (red).

capacitance model) and red (experimental) curves shows a quite good matching as far as the dip effect concerns. The green curve (simulation with constant capacitance) is on the other hand consistent with the analytical model that will be introduced hereinafter. The dip effect may, in most cases, be neglected but, if this is not the case, it can be compensated with very simple methods, such as via Look-Up Table (LUT).

6.3.1 Measurement of inverter distortion component by current injection onto active space vector

The phase voltage reference that contains the distortion term, can be represented analytically as in Eq. 6.26 and Eq. 6.27, where the last term of Eq. 6.26, named $f_d(\bullet)$, represents the distortion due to inverter non-linearities, being a function of all the three phase currents (Note: in this section notation U is used instead of V for voltage).

$$U_x^* = U_x + f_d\ (i_a, i_b, i_c) = R_s\ i_x + f_d\ (i_a, i_b, i_c) \tag{6.26}$$

$$U_x^* = \begin{cases} \frac{4}{3}U_{sw}sign(i_x) + \left(\frac{T_{dt}^2}{4C_{out}T_{sw}} + R_s\right) i_x & if \quad |i_x| < i_{thr} \\ \frac{2}{3}sign(i_x)\left(U_{dc}\frac{T_{dt}}{Tsw} + 2U_{sw}\right) + \left(\frac{1}{3}\frac{T_{dt}^2}{4C_{out}T_{sw}} + R_s\right) i_x - \frac{2}{3}\frac{C_{out}U_{dc}^2}{T_{sw}}\frac{1}{i_x} & if \quad i_{thr} < |i_x| < 2i_{thr} \\ \frac{4}{3}sign(i_x)\left(U_{dc}\frac{T_{dt}}{T_{sw}} + U_{sw}\right) + R_s i_x - 2\frac{C_{out}U_{dc}^2}{T_s w}\frac{1}{i_x} & if \quad |i_x| > 2i_{thr} \end{cases} \tag{6.27}$$

The terms U_{dc}, U_x^*, U_x, i_x, $f_d\,(\bullet)$, R_s, U_{sw}, T_{dt}, C_{out}, T_{sw} represent the dc link bus voltage, average phase reference voltage (output of current controller), average phase actual voltage (as measured on the machine), average phase actual current, distortion term on inverter phase voltage, phase resistance, average switching devices voltage drop $(U_{IGBT} + U_d)2$, dead time, output capacitance and switching period, respectively. All the voltages and currents are intended as averaged in one switching cycle. After measuring the non-linear V-I characteristic of the inverter as explained in the previous section (an example of the sampled one is shown in Fig. 6.6), the load resistive term and the dead time distortion voltage can be achieved as reported in [57], i.e. by means of a Multi Linear Regression approach considering the measurement range $|i_a| > 2i_{thr}$. Main equations are reported in Eq. 6.28, the system unknown parameters C_{out}, R_s and U_{sw} can be estimated. The last term is often neglected in literature approaches, but in many applications this overlook causes errors in the identification of the correct voltage compensation function. The term x is a $N \times 3$ matrix, whilst y is a $N \times 1$ column vector, assuming N as the number of points used for the identification.

$$\begin{aligned} U_{regr}^* &= \chi_0\ sign(i_a\ ) + \chi_1\ i_a + \chi_2/i_a \\ X &= \begin{bmatrix} X_0 \\ X_1 \\ X_2 \end{bmatrix} = (x^T x)^{-1} x^T y \end{aligned} \tag{6.28}$$

$$\begin{aligned} \chi_0 &= \tfrac{4}{3}(\tfrac{U_{dc}T_{dt}}{T_{sw}} + U_{sw}) \\ \chi_1 &= R_s \\ \chi_2 &= -\tfrac{C_{out}U_{dc}^2}{T_{sw}} \end{aligned} \tag{6.29}$$

$$\begin{aligned} x(i,1) &= sign(i_a(i)) \\ x(i,2) &= i_a(i) \\ x(i,3) &= \tfrac{1}{i_a(i)} \end{aligned} \tag{6.30}$$

$$y(i) = u_a^*(i) \tag{6.31}$$

The process for estimating these parameters (which will lately be used to build the compensation function) is strongly dependent on the knowledge of the threshold current value i_{thr}, whose value cannot be known a-priori since it depends on the output capacitance Eq. 6.32,

preventing a straightforward self commissioning procedure. Two new methods that assure minimal error estimation are proposed and validated in the next sections, demonstrating the superiority of the results over state of the art approaches.

$$i_{thr} = 2C_{out}U_{dc}/T_{dt} \tag{6.32}$$

6.3.2 Measurement of inverter distortion component by current injection orthogonal to one of the three axes

Measurement of the non-linear V-I characteristic can be done as explained in the previous section, i.e. by performing the current injection onto the $\alpha-$axis. The obtained measurements are certainly correlated to the compensation function, but the data cannot be used directly to compensate for the voltage distortion, as measurement of the actual leg distortion voltage caused by dead-time is needed to this purpose. If known, this function shall be added to the reference voltage produced by the current controller as a feed forward term, in order to compensate for the non-linearities. Indeed, also in the case a direct compensation is adopted, e.g. by using a look-up-table (without any analytical model), this function would be necessary and it cannot be derived directly from the measured data. As already reported in Eq. 6.26, the contribution of all leg currents is in fact present in the measured distortion function in the case of $\alpha-$axis injection. A different strategy is proposed here, i.e. the direction of the injection is changed to a direction being orthogonal to one of the three axes, i.e.

$$\theta_{inj} = \frac{2k\pi}{3} \pm \frac{\pi}{2}, k \in 1, 2, 3 \tag{6.33}$$

In this way, the current in one phase (i.e. the one being orthogonal to the direction of the injection) is always zero. The difference with respect to previous procedure is that, in this case, the measurement can be directly used for the compensation, as phase voltage distortion term can be obtained directly after the measurements, as will be demonstrated hereinafter. In Fig. 6.10, experimental measurement and simulation of the inverter characteristic obtained by $\beta-$axis injection are shown.

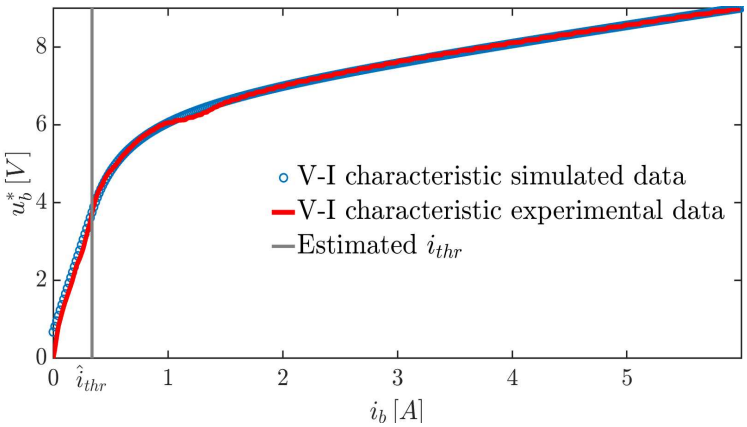

Figure 6.10: Non-linear V-I characteristic identified by $\beta-$axis injection.

The reference leg voltage of phase x (i.e. U^*_{x0}) is the sum of the phase reference voltage U^*_x (output of the current regulators) and an injected common mode voltage U^*_{0N} (e.g. a 3^{rd} harmonic), as reported in Eq. 6.34 (the symbol 0 is addressing for the inverter reference terminal, whilst N for the machine neutral). The difference between the reference and the actual inverter leg voltage Eq. 6.35 is defined as the distortion term $f_d\,(i_x)$, which is a non-linear function of the phase current of that phase. Note that this term is only a function of the considered leg current, as leg voltage is considered.

$$U^*_{x0} = U^*_x - U^*_{0N} \tag{6.34}$$

$$U^*_{x0} - U_{x0} = f_d(i_x) \tag{6.35}$$

On the hypothesis of balanced load, the sum of the actual three-phase voltages Eq. 6.36 lead to Eq. 6.37, i.e. the voltage difference between the inverter reference terminal and the machine neutral can be calculated as a function of each leg voltage.

$$U_x = U_{x0} + U_{0N} \tag{6.36}$$

$$U_{0N} = -\frac{1}{3}(U_{a0} + U_{b0} + U_{c0}) \tag{6.37}$$

Substituting Eq. 6.34 into Eq. 6.35, expression Eq. 6.37 can be rewritten as Eq. 6.38.

$$U_{0N} = -\frac{1}{3}[U^*_a + U^*_c - 3U^*_{0N} - f_d(i_a) - f_d(i_b) - f_d(i_c)] \tag{6.38}$$

Since the sum of the reference phase voltages is zero, Eq. 6.38 can be simplified and by substituting into Eq. 6.36, the generic reference voltage expression Eq. 6.40 is achieved.

$$U_{0N} = \frac{1}{3}U^*_{0N}[f_d(i_a) + f_d(i_b) + f_d(i_c)] \tag{6.39}$$

$$U^*_x = U_x + f_d(i_x) - \frac{1}{3}[f_d(i_a) + f_d(i_b) + f_d(i_c)] \tag{6.40}$$

By injecting a current into the $\beta-$axis ($i_a = 0$, $i_b = -i_c$) and using Eq. 6.40, the reference voltage U^*_b can be obtained, as reported in Eq. 6.41. Since the distortion function $f_d(i_x)$ is odd, and actual phase voltage U_b is indeed taking only the actual voltage drop due to the phase resistance, the expression can be rewritten as Eq. 6.42. The last equation shows that by knowing the reference phase voltage in the $b-$axis and its phase current, the distortion function can be estimated if given R_s and vice-versa. This is true only if the injection is applied on an orthogonal axis, such as β.

$$U^*_b = U_b + \frac{1}{3}[2f_d(i_b) - f_d(-i_b)] \tag{6.41}$$

$$U_b^* = R_s i_b + f_d(i_b) \tag{6.42}$$

Once the acquisition of the V-I points is completed, application of Multi-Linear Regression allows to estimate $\hat{C}_{out}$, $\hat{U}_{sw}$ and $\hat{R}_s$ and, finally, build a compensating function for dead-time effects. The new expressions based on the considered analysis are reported in Eq. 6.43, that holds the same information as in Eq. 6.27. The main difference is that the new equation is defined in only 2 intervals ($\Lambda 0$ and $\Lambda 1$, for $|i_x|$ bigger or smaller then i_{thr} respectively, i.e. low and high current regions) instead of 3, and that the $f_d(i_x)$ can be directly used as a compensation function (even by using a LUT).

$$\begin{cases} f_d(i_x)^{\Lambda 0} = sign(i_x)U_{sw} + \frac{T_{dt}^2}{4C_{out}T_{sw}} i_x & if \quad |i_x| < i_{thr} \\ f_d(i_x)^{\Lambda 1} = sign(i_x)(U_{sw} + U_{dc}\frac{T_{dt}}{T_{sw}}) - \frac{C_{out}U_{dc}^2}{T_{sw}}\frac{1}{i_x} & if \quad |i_x| > i_{thr} \end{cases} \tag{6.43}$$

The estimated parameters obtained by using both measurement identification procedures are reported in Table. 6.1, proving that both the injection methods provide roughly the same results. Once the three parameters have been identified, compensation is quite straightforward, as shown in the block diagram of Fig. 6. It is worth to mention that the compensating components are calculated from Eq. 6.43 starting from the current references, in order to reduce noise issues, and are added to the outputs of the current controllers.

Table 6.1: Estimated Parameters for $\alpha-$ and $\beta-$ Injection.

Estimated parameters	α injection	β injection
$\hat{C}_{out}$	1.24 $[nf]$	1.1 $[nf]$
$\hat{U}_{sw}$	0.75 $[V]$	0.68 $[V]$
$\hat{R}_s$	0.40 $[\Omega]$	0.42 $[\Omega]$

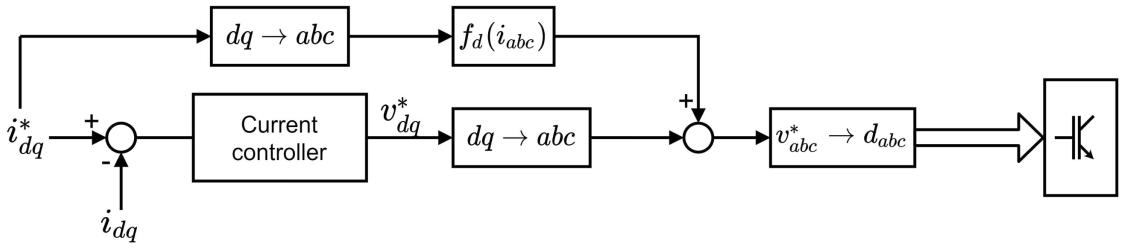

Figure 6.11: dead-time compensation control scheme.

6.3.3 Additional remarks on current or voltage injection

The measurement accuracy during the identification procedure must be as high as possible, especially in the lower current region (i.e. around i_{thr}) where the capacitive effects provide the most important contribution to the transition of the leg output voltage during the dead

time. Unfortunately, the capacitive effect introduces a phase lag on the current waveform with respect to the symmetry point of the PWM waveforms, thus requiring the sampling point to be shifted ahead in order to guarantee a proper measurement of the actual average value of the current within the PWM period. This situation is roughly sketched in Fig. 6.12. If a current feedback control loop is used for the injection during the identification phase, the asymmetry which is introduced causes a misbehavior of the current regulation, which would try to control an average current which differs from the reference one by the quantity i_{err} in the figure. An open-loop voltage injection could be employed instead, where the reference is a slowly increasing staircase amplitude voltage, and the current is sampled. This does not fully solve the problem of the current sampling inaccuracy, but having an open-loop system for the injection procedure might, in some applications, be the best solution. This topic is however beyond the scope of this chapter, but some additional remarks will be provided in a later section, where a compensation solution for the sampling point shift will be proposed an discussed.

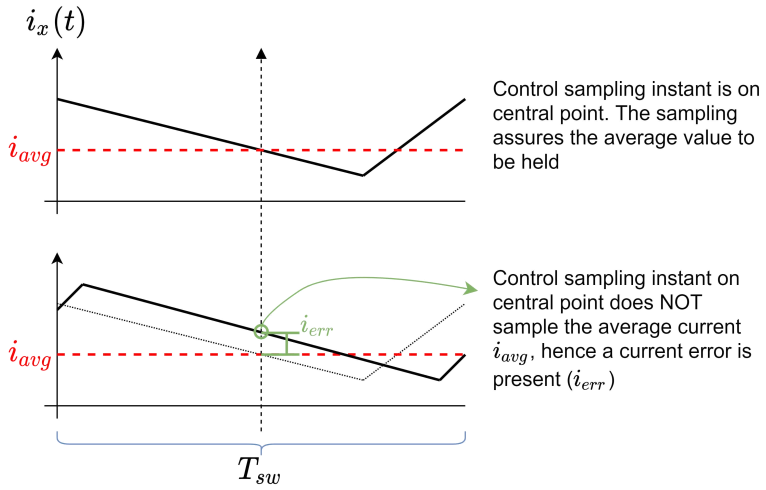

Figure 6.12: Effects of the capacitive lag on average current sampling.

6.4 Current Threshold Identification Techniques

The quality of the parameters needed for the dead-time compensation is strongly related to the correct knowledge of the threshold current, a value that cannot be known a-priori. Previous literature addressed the importance of this issue, [57], but only the simplest solution was adopted, i.e. that value is roughly guessed based on nominal parameters of the system and approximated analytical expression Eq. 6.44. Unfortunately, this expression is a function of the same parameter to be identified, namely the overall equivalent capacitance.
Two methods for high-accuracy automatic identification the current threshold value are proposed and validated hereinafter, the first one based on an iterative process while the second one based on seeking the minimum of a proper cost function. Both algorithms converge to same values for the estimated parameters $\hat{i}_{thr}$ and $\hat{C}_{out}$, $\hat{U}_{sw}$ and $\hat{R}_s$, even though

the latter is more computationally expensive compared to the iterative one.

$$i_{thr} = \frac{2C_{out}(U_{dc} - U_{ce0} + U_{f0})}{T_{dt}} \approx \frac{2C_{out}U_{dc}}{T_{dt}} \tag{6.44}$$

6.4.1 Iterative method

The threshold current i_{thr} can be computed analytically as reported in Eq. 6.44, but since the capacitance value is not known at first, the regression is iterated in order to find a new value of capacitance and to update the threshold current until convergence is reached. The method is explained in detail hereinafter, its flow chart being reported in Fig. 6.13.

An initial current threshold guess $\hat{i}_{thr}(0)$ is chosen in order to allow the startup of the algo-

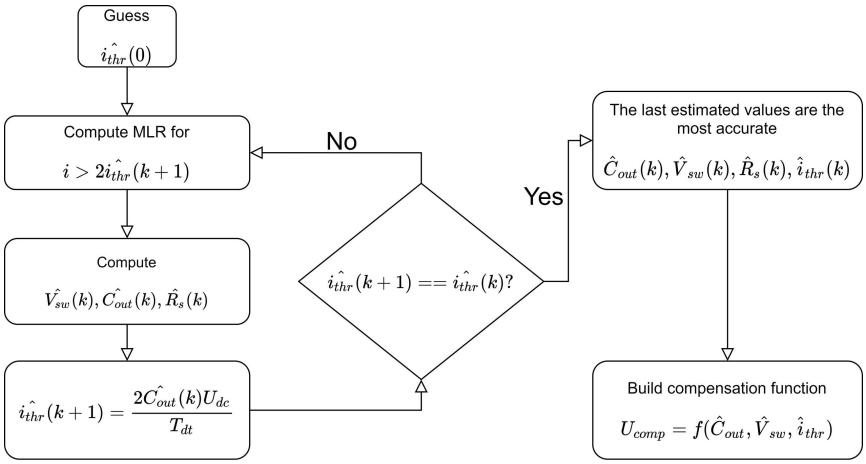

Figure 6.13: Flow-chart of the iterative method for threshold current identification.

rithm. The required accuracy in the knowledge of this term is not critical for the convergence of the algorithm, and its order of magnitude is easily predictable by assuming that the overall output capacitance as seen from the output terminal of the leg is roughly corresponding to that of power switches. The dc link voltage is usually measured, and the dead-time is a system defined parameter.

Given the first guess, a regression is computed for the current samples such that $i_x > 2i_{thr}$, finding in this way the estimates $\hat{C}_{out}(k)$, $\hat{U}_{sw}(k)$ and $\hat{R}_s(k)$. The newly computed value of $\hat{C}_{out}(k)$ is used as a guess to compute the next current threshold Eq. 6.45 and iterate the process:

$$\hat{i}_{thr}(K+1) = \frac{2C_{out}(k)U_{dc}}{T_{dt}} \tag{6.45}$$

The exit condition is based on the difference between two estimates of the threshold current being below a certain tolerance, Eq. 6.46. Convergence assures $\hat{C}_{out}(k)$, $\hat{U}_{sw}(k)$ and $\hat{R}_s(k)$ estimates to be enough accurate for compensation.

$$|\hat{i}_{thr}(K+1) - \hat{i}_{thr}(K)| < \varepsilon_{thr} \tag{6.46}$$

A convergence diagram of the proposed iterative algorithm in an actual experimental case is reported Fig. 6.14, showing the estimated threshold current at different iterations (blue curve), together with the actual value (red curve). Only 4 iterations are needed in order to reach the actual current threshold value of 0.34A, starting from the initial guess of 0.5A, as calculated by system parameters and capacitance guess value.

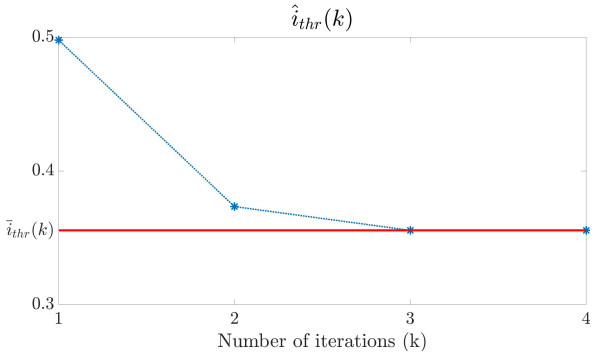

Figure 6.14: Dynamics of the iterative algorithm for the identification of i_{thr}.

6.4.2 Minimum error seeking by dual-regression

A second algorithm is proposed for the identification of the current threshold value, based on the minimization of a proper cost function. The main idea is explained hereinafter.
Given the distortion function measured using the orthogonal axis injection as seen in subsection. 6.3.2, it is possible to build a proper cost function whose minimization gives information on the actual threshold current. Since the distortion $f_d(i_x)$ can be written in the two intervals $\Lambda 0$ (low current region) and $\Lambda 1$ (high current region), as already reported in Eq. 6.43, it is possible to introduce two different MLRs. The idea is to compute the two regressions moving the threshold value at each iteration and finding the value that provides the minimum error between the regression functions and measured data, as sketched in flow chart of Fig. 6.15. Obviously, the absolute values of the error are considered. In order to gain additional insight of the method, some experimental results in two different situations are depicted in Fig. 6.16, namely the choice of the estimated threshold ($\hat{i}_{thr}$) is greater (top diagram) and smaller (bottom diagram) than the actual one ($\bar{i}_{thr}$). The actual (measured) V-I characteristic is drawn (solid lines) together with the results of the two MLRs in the low and high current regions (dotted lines). The absolute values of the difference between measured characteristic and regressions are calculated and reported in red. Please note that its value is not exactly zero when the measured characteristic and regressions are intersecting, as it should be. This is due to the discretization of the measured data in the horizontal axis (the point corresponding to the measurement is not available in general in any point of the regression). Nevertheless, this is not significantly affecting the accuracy of the threshold estimation and can be further reduced by reducing the quantization of the current axis. By adopting the voltage expressions Eq. 6.47, where the terms $U_x^{\Lambda 0}$ and $U_x^{\Lambda 1}$ are the leg voltages measured in low and high current regions respectively, the terms $\lambda_i^{\Lambda \mathrm{j}}$ can be used to

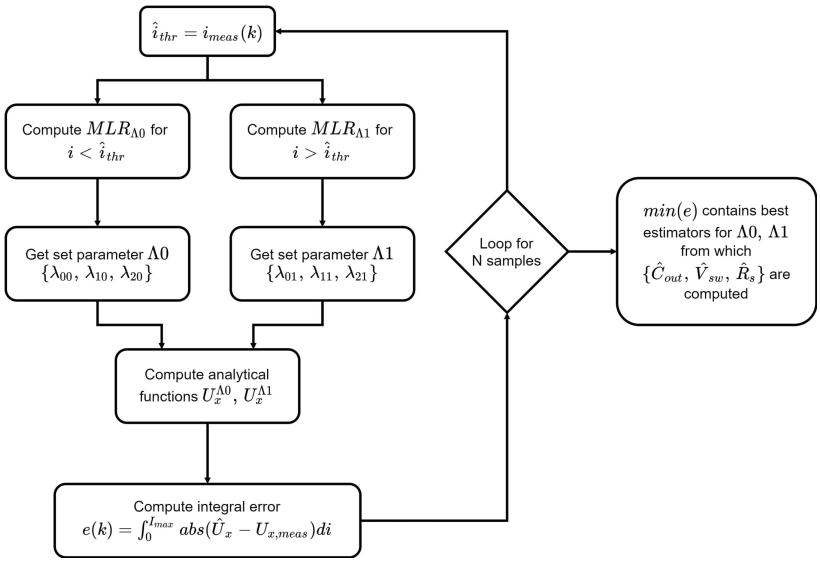

Figure 6.15: Flow chart illustrating the minimization of the cost function for current threshold estimation.

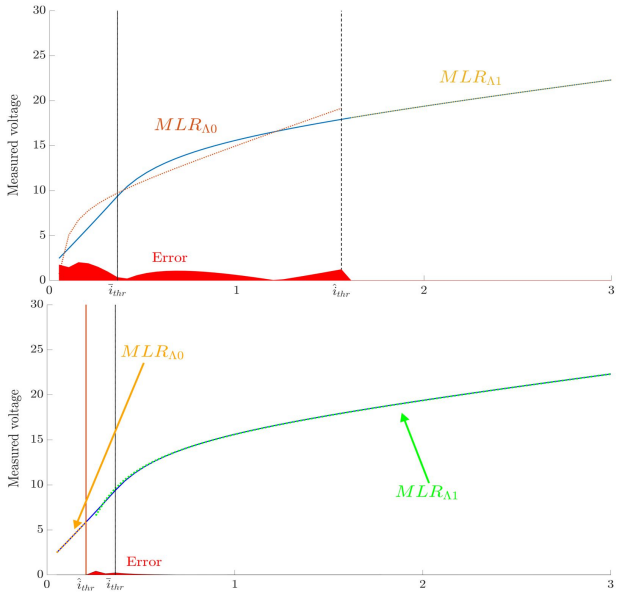

Figure 6.16: Experimental results of the minimum seeking of the threshold current: measured V-I characteristic (solid curve) and results of MLRs (dotted curve) for the estimated threshold ($\hat{i}_{thr}$) greater (top diagram) and smaller (bottom diagram) than the actual one ($\bar{i}_{thr}$).

estimate the parameters in Eq. 6.43, as reported in Eq. 6.48 and Eq. 6.49, where notation $\hat{\square}$ is intended for estimated parameters.

$$\hat{U}_x = \begin{cases} U_x^{\Lambda 0} = \lambda_0^{\Lambda 0} sign(i_x) + \lambda_1^{\Lambda 0} i_x + \frac{\lambda_2^{\Lambda 0}}{i_x} & if \quad |i_x| < i_{thr} \\ U_x^{\Lambda 1} = \lambda_0^{\Lambda 1} sign(i_x) + \lambda_1^{\Lambda 1} i_x + \frac{\lambda_2^{\Lambda 1}}{i_x} & if \quad |i_x| > i_{thr} \end{cases} \tag{6.47}$$

$$\begin{aligned} \lambda_0^{\Lambda 0} &= \hat{U}_{sw} \\ \lambda_1^{\Lambda 0} &= \hat{R}_s + \frac{T_{dt}^2}{4\hat{C}_{out} T_{sw}} \\ \lambda_2^{\Lambda 0} &= 0 \end{aligned} \tag{6.48}$$

$$\begin{aligned} \lambda_0^{\Lambda 1} &= \hat{U}_{sw} + U_{dc} \frac{T_{dt}}{T_{sw}} \\ \lambda_1^{\Lambda 1} &= \hat{R}_s \\ \lambda_2^{\Lambda 1} &= -\frac{\hat{C}_{out} U_{dc}^2}{T_{sw}} \end{aligned} \tag{6.49}$$

Finally, the calculation of the cost function is reported in Fig. 6.17 by sweeping the estimated threshold value adopted for the MLRs in the two regions up to the rated value of the machine current. One can notice that the minimum value is corresponding to the actual threshold value $\bar{i}_{thr}$, proving a complete agreement with the iterative method and the effectiveness of the solution. It is worth noticing that this method is however more computationally intensive than the iterative one.

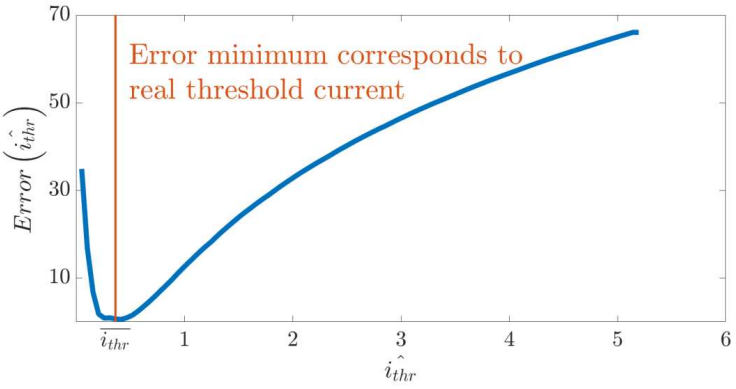

Figure 6.17: Experimental results of the minimum seeking of the threshold current: cost function plot as a function of the threshold current value (sweep up to the rated current of the machine).

6.5 Leg Voltage Lag due to Capacitive Effects: Current Sampling Compensation Strategy

Accurate compensation of leg voltage distortion allows to match the average voltage within a switching period to the reference one (output of the current controller). However, the capacitive behavior of the leg switching node (mainly due to the switching devices), introduces a phase lag on the actual instantaneous leg voltage. This, in turn, shifts ahead the current waveform (fundamental and ripple) with respect to the ideal symmetry point of the PWM

carrier, normally considered as the optimal sampling point for the average phase current. The obtained current samples are no more corresponding to the average values within the switching period. Indeed, a similar issue can be experienced during machine operation at high fundamental to switching frequency due to the back EMF, as reported in [78]. However, only the first effect has been considered in this chapter, being closely related to the dead time, and a proper compensation strategy is proposed. Either the sampling instant or the PWM waveforms can be shifted in a controlled way, based on a proper analytical model, thus allowing to recover a correct measurement of the average value of the phase current.

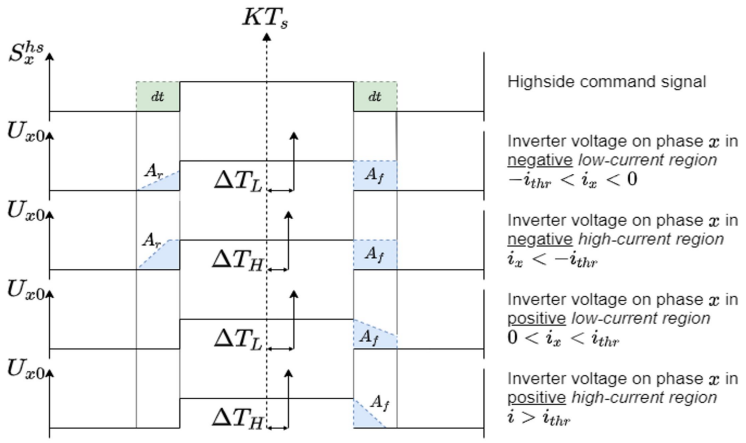

Figure 6.18: Leg voltage shapes for any combination of output current sign and amplitude during the dead time.

The high side PWM signal and the corresponding shape of the leg voltage in a switching period are depicted in Fig. 6.18, for a certain value of the leg node capacitance and four different current values, namely positive and negative, higher or lower than the threshold value. The dead time on both semi periods are shown with green areas, whilst the light blue ones highlight the behavior of the leg voltage due to the capacitive effect, resulting in a modification of both the average leg output voltage and the symmetry point of the waveform. One can notice that, based on the choice of dead time insertion strategy (e.g. delaying the rising edges, as in this example, or introducing a symmetrical dead-time), the resulting leg voltage is modified (e.g. shifted ahead in this example) and the correct average current value can be obtained by either delaying the sampling point (as shown in the figure) or advancing the PWM signals. If this second case is considered (that provides some additional benefits as briefly discussed hereinafter), the advance time can be analytically calculated by imposing the symmetry condition of the average leg voltage within each PWM switching period, Eq. 6.50.

$$\int_0^{T_{s/2}} U_{x0}(t)dt = \int_{T_{s/2}}^{T_s} U_{x0}(t)dt \tag{6.50}$$

The contribution of the light blue areas A_r and A_f can be analytically calculated, leading to Eq. 6.51 and Eq. 6.52. The switch voltage U_{sw} has been neglected to simplify the calculations (this assumption does not introduce a substantial error). By forcing the symmetry

condition Eq. 6.50, the time advance (t_{adv}) for each current region can be computed, as reported in Eq. 6.53.

$$A_r = \begin{cases} 0 & if \quad i_x \geq 0 \\ -\frac{T_{dt}^2 i_x}{4C_{out}} & if \quad -i_{thr} \leq i_x < 0 \\ T_{dt}U_{dc} + \frac{U_{dc}^2 C_{out}}{i_x} & if \quad i_x < -i_{thr} \end{cases} \tag{6.51}$$

$$A_f = \begin{cases} \frac{U_{dc}^2 C_{out}}{i_x} & if \quad i_x \geq i_{thr} \\ T_{dt}U_{dc} - \frac{T_{dt}^2 i_x}{4C_{out}} & if \quad 0 \leq i_x < i_{thr} \\ T_{dt}U_{dc} & if \quad i_x < 0 \end{cases} \tag{6.52}$$

$$t_{adv} = \begin{cases} t_{adv}^{\Lambda 0} = \frac{T_{dt}}{2} - \frac{T_{dt} - |i_x|}{4i_{thr}} & if \quad |i_x| < i_{thr} \\ t_{adv}^{\Lambda 1} = \frac{U_{dc}C_{out}}{2|i_x|} & if \quad |i_x| > i_{thr} \end{cases} \tag{6.53}$$

It is worth noticing that delaying or advancing must be applied to each leg current sampling or PWM waveform respectively, as a function of system parameters and the actual current value of each leg, based on model Eq. 6.53. It is also important to notice that the latter solution (i.e. advancing of PWM signals) allows to regain symmetrical leg voltages, with additional advantages in terms of current ripple minimization, and it is therefore preferable with respect to the former solution. This compensation becomes particularly important close to the zero-crossings of the currents and with low inductance loads, since ripple current is high and an incorrect current sample is obtained with respect to the actual average value if no compensation is adopted. Reduction of the current ripple by PWM advancing (especially near zero crossings, as said), definitively allows to improve the quality of the controlled currents.

Simulation results are reported in Fig. 6.19. to provide a validation of the proposed current sampling compensation strategy in case of PWM advancing based on Eq. 6.53 and a constant capacitance model for the power switches. Triangular carrier and ideal sampling instant (i.e. the peaks of the carrier signal), instantaneous leg voltages, their average values within each half switching period and one phase current are reported without (left diagram) and with (right diagram) proper advancing on the PWM signals on each leg. The actual average values of the a leg output current is also drawn. One can notice how the value of the instantaneous current in the ideal sampling point is quite far from the average values without the PWM advancing strategy. When the advancing is active, a perfect match is obtained, as clearly visible in the right diagram, thus proving that the compensation is effective. Also, the average voltage values are identical within each half switching period, demonstrating that PWM advancing allows to recover the symmetry of the leg voltages, in turn minimizing the current ripple as shown in the bottom subplots.

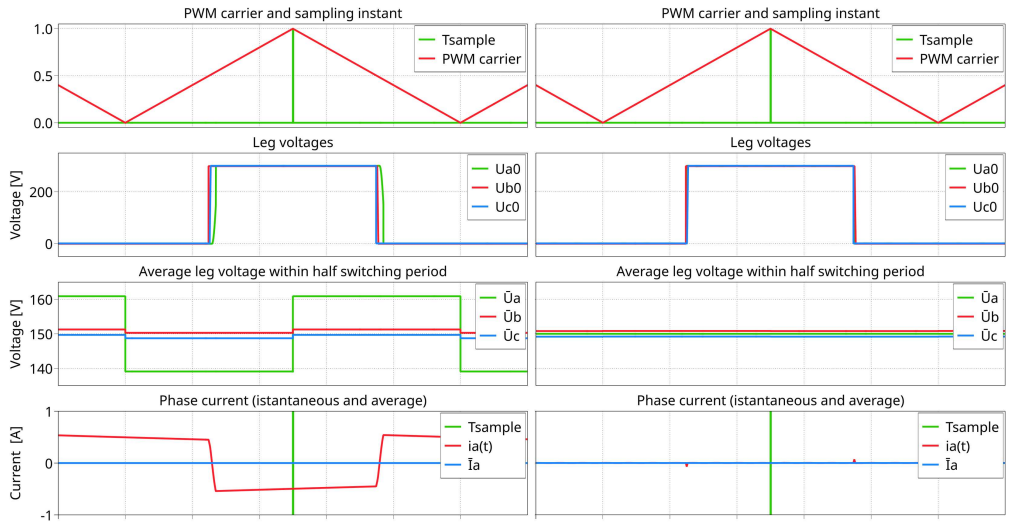

Figure 6.19: Current sampling compensation strategy: without (left) and with (right) PWM advancing.

6.6 Experimental Results

Experimental validation of the dead time compensation strategy was done by a commercial drive feeding both an induction and a permanent magnet synchronous machine.
A first set of tests have been performed with the induction machine, fed by a rotating voltage space vector (whose amplitude is comparable to the level of voltage distortion introduced by the dead time) and a controlled rotating current space vector. The results of the voltage injection are reported in Fig. 6.20, where the comparison between the resulting phase currents is shown without and with the compensation, respectively, leading to a reduction of the total harmonic distortion (THD) from 9.4 percent to 3.6 percent. The amplitude of the current in the second case is obviously higher due to a reduced (negligible) effect of dead time on the actual phase voltages with the compensation active. The results of the controlled rotating current space vector are reported in Fig. 6.21, where the comparison between the resulting reference voltages is shown without and with the compensation, respectively, leading to a reduction of the total harmonic distortion (THD) from 8.2 percent to 4.2 percent. The current is closed loop controlled, therefore its shape is almost sinusoidal in both cases. The amplitude of current and voltage is also very different between with and without compensation.

The last test conditions have also been adopted to analyze the effects of the estimated capacitance value on the effectiveness of the compensation. In the test results of Fig. 6.22 two detuned values are adopted with respect to the nominal (i.e. the value estimated by the regression algorithm), namely -50 percent and +100 percent. It is relatively clear that the quality of the compensation decreases in both the situation, as expected, leading to a THD level of 5.8 percent and 6.9 percent respectively.

Indeed, compensation of inverter non-linearities has also a beneficial effect on the response

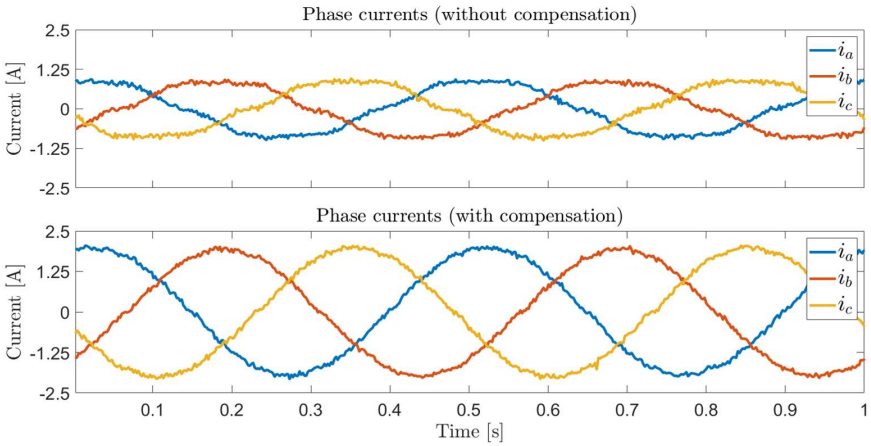

Figure 6.20: Phase currents for open loop rotating voltage space vector injection (induction machine, $f_s = 2Hz$, $U_s = 35V$, $T_{dt} = 4\mu s$, $T_{sw} = 100\mu s$).

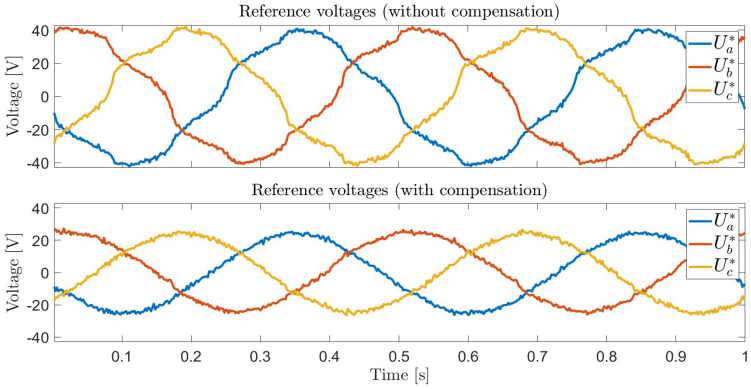

Figure 6.21: Reference voltages for closed loop rotating current space vector control (induction machine, $f_s = 2Hz$, $|i| = 2A$, $T_{dt} = 4\mu s$, $T_{sw} = 100\mu s$).

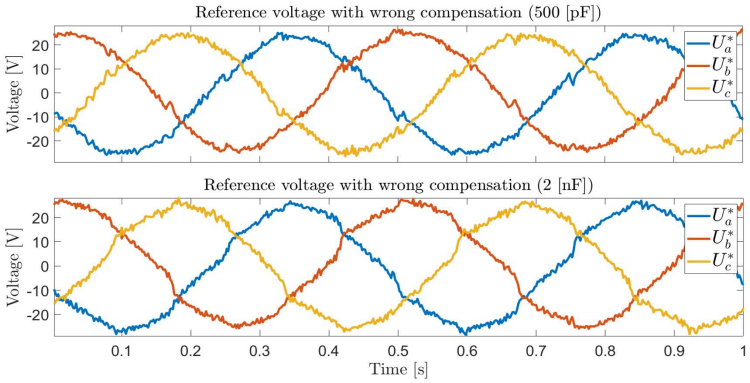

Figure 6.22: Reference voltages for closed loop rotating current space vector control in case of detuned capacitance value in the compensation model.

of the current control loop, as demonstrated hereinafter in a second set of tests done with the permanent magnet machine at $20Hz$ electrical frequency. A standard cascaded speed and current control is considered, with two different values for the load torque, namely 0.9 and $3.7Nm$. The current regulators have been intentionally tuned for a lower bandwidth, in order to emphasize the effects of the dead time on the current control performance for the sake of a better evaluation of the effectiveness of the compensation strategy. The results are reported in Fig. 6.23. The current is relatively distorted when compensation is not applied, since the rejection of the (voltage) non linearity effects on the current control loop is poor due to the the chosen bandwidth. Injection of the compensation voltages allows to improve the shape of the current in both the load conditions. Quantitative comparison is reported in Table. 6.2, where the THD and the relative amplitude of 5^{th} and 7^{th} harmonic is reported in dBc (i.e. with respect to the fundamental value), showing almost 3 times lower THD with compensation.

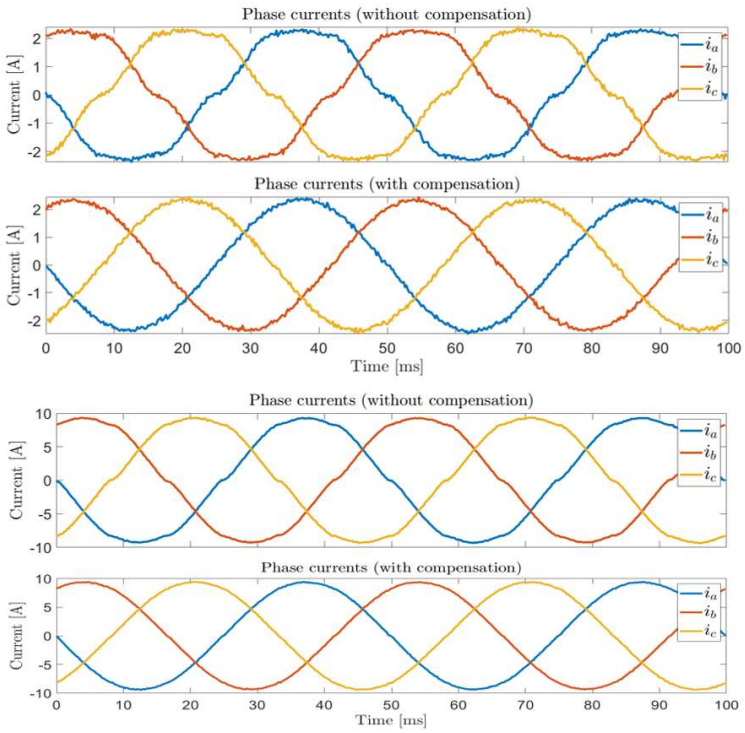

Figure 6.23: Phase currents without and with dead time compensation under two different load torque ($0.9Nm$ top diagrams, $3.7Nm$ bottom diagrams.

Table 6.2: Performance Comparison.

Load Torque	Compensation	THD	5^{th} harm	7^{th} harm
0.9 $[Nm]$	With	7.5 percent	-23 dBc	-50 dBc
0.9 $[Nm]$	Without	2.5 percent	-51 dBc	-48 dBc
3.7 $[Nm]$	With	3.8 percent	-30 dBc	-36 dBc
3.7 $[Nm]$	Without	1.3 percent	-43 dBc	-53 dBc

6.7 Conclusion

A recent approach for dead-time compensation adopting an analytical model of the physical behavior of the inverter non-linearities has been considered. Model parameters are derived from a self commissioning procedure, based on proper voltage injection and processing, both affecting the accuracy of achievable compensation. One of the crucial aspects of this approach is the autonomous selection of the threshold current of the measured voltage to current characteristics, a value whose reliable knowledge is mandatory for the accurate identification of the non-linearity model. Two new methods that assure minimal error estimation have been proposed and validated in this chapter, allowing the full self commissioning of the compensation algorithm. Also, a different type of voltage injection has been proposed, allowing a more effective estimation of the voltage to current characteristic and direct compensation of each leg voltage as a function of the corresponding current. Finally, the effects of the non-linearities on the accuracy of current sampling and control loops have been analyzed, and an original compensation strategy was proposed and validated. Theoretical analysis and developments have been reported, together with accurate simulations and experimental results based on a commercial drive.

Chapter 7

Conclusion

In this thesis, the advanced control of Interior Permanent Magnet Synchronous Motor and Synchronous Reluctance Motor is studied.
The thesis is started by an introduction in Chapter. 1. In this chapter a literature review is presented for IPM and SynR machines, their main features, advantages, main applications. The magnetic structure of IPM and SynR motors are examined in Chapter. 2. Based on advantages and disadvantages of these motors they have been compared. Following this evaluation of the PMSM analytical model, mechanical and electrical equations are obtained. Furthermore,the behaviour of the motor in MTPA and flux-weakening regions is presented in this chapter.
In Chapter. 3, A fair evaluation of the accuracy and performance of RSI and VSI and a direct comparison between them is proposed. Simulations have been carried out for two types of motors. To avoid possible errors due to interpolation of flux maps and measures inaccuracy, an analytical model of SynRM is developed and used to test the accuracy of the two algorithms. As can be seen from the results, if no compensation for tracking error is applied to VSI algorithm, RSI has better accuracy.
VSI accuracy for estimating the MTPA is affected by the knowledge of some machine parameters and should be considered indeed an estimation method based on the model knowledge, while RSI entirely relies on extremum seeking approach. In the VSI method, the steady-state MTPA error is mainly due to variation of magnetic parameters, which were supposed constant. In order to address this issue, a compensation strategy for the tracking error is introduced, resulting in a substantial improvement of accuracy, allowing to increase the accuracy of this method even in the case the machine flux maps are known with poor resolution. A further improvement is proposed, which allows analytical tuning and adaptation of the tracking loop gains, assuring both stability and the same dynamical performance in the whole machine operating range.
From the dynamical point of view, the model of an IPMSM is used to test the dynamical behavior of the two algorithms. Another test is carried out on a real SynRM to investigate the accuracy of the two algorithms even when quantization of flux maps is low. Experimental tests have been carried out on the real IPMSM in order to prove simulation results. As can

be seen from the results, accuracy of the VSI algorithm is worse with respect to that of RSI, when no L_d LUT contribution is applied. However, since the saliency of the IPMSM is lower with respect to SynRM, the error is relatively small.
As a future works, the RSI and improved VSI can be tested on the Permanent Magnet assisted Synchronous Reluctance Motors (PMa-SyRMs).
In Chapter. 4, a new analytical solution is presented to control the motor torque in the maximum-torque-per-ampere and flux-weakening region with a torque constraint. The controller is designed to operate in wide speed range; MTPA, flux weakening and MTPV regions. Based on the proposed solution the complexity of the quartic equation of dq axis current is decreased significantly. The method is compared with another analytical solution, experimentally to investigate them based on the computation time. By using the proposed method, the computation time is decreased 56% versus Ferrari's method for MTPA region. In flux weakening region the difference of computation time for the proposed method and Ferrari's solution is 51%. Furthermore, the novel solution is applied to an IPMSM in MTPA region experimentally considering constant and adaptive q-axis inductance. As a results, the proposed method track the MTPA trajectory with a high accuracy.
As the future works, the novel method is going to be tested experimentally in flux-weakening region. In addition, the minimum vector solution can be studied analytically in MTPV region.
In Chapter. 5, GMDH method is presented to approximate the flux-linkages of the IPMSM. Using this method can be done online where the inputs are the dq axis currents. The method is compared with a polynomial method. The simulation results confirm that the accuracy of GMDH is higher than polynomial method due to error percentage. Based on the results the error percentage for $d-$ and $q-$axis flux-linkages using GMDH is less 3 times and 2 times respectively compare to polynomial approximation method. The GMDH method approximate the flux-linkages maps of IPMSM (achieving approximately half the RMSE error, Table I), while polynomial methods are accurate only for SynRM.
As the future work, the GMDH method can be used for SynRM motor to approximate the flux maps. Furthermore, the approximated flux maps can be applied to the controller instead of constant value of the motor parameters or LUT.
In Chapter. 6, a recent approach for dead-time compensation adopting an analytical model of the physical behavior of the inverter non-linearities has been considered. Model parameters are derived from a self commissioning procedure, based on proper voltage injection and processing, both affecting the accuracy of achievable compensation. One of the crucial aspects of this approach is the autonomous selection of the threshold current of the measured voltage to current characteristics, a value whose reliable knowledge is mandatory for the accurate identification of the non-linearity model. Two new methods that assure minimal error estimation have been proposed and validated in this chapter, allowing the full self commissioning of the compensation algorithm. Also, a different type of voltage injection has been proposed, allowing a more effective estimation of the voltage to current characteristic and direct compensation of each leg voltage as a function of the corresponding current. Finally,

the effects of the non-linearities on the accuracy of current sampling and control loops have been analyzed, and an original compensation strategy was proposed and validated. Theoretical analysis and developments have been reported, together with accurate simulations and experimental results based on a commercial drive.

Bibliography

[1] Waide Paul and Brunner Conrad U. Energy-efficiency policy opportunities for electric motor-driven systems – analysis - iea, 2011.

[2] Shuhua Fang, Huan Liu, Haitao Wang, Hui Yang, and Heyun Lin. High power density pmsm with lightweight structure and high-performance soft magnetic alloy core. *IEEE Transactions on Applied Superconductivity*, 29(2):1–5, 2019.

[3] Enrico Carraro, Mattia Morandin, and Nicola Bianchi. Traction pmasr motor optimization according to a given driving cycle. *IEEE Transactions on Industry Applications*, 52(1):209–216, 2016.

[4] Seyed Morteza Taghavi and Pragasen Pillay. A mechanically robust rotor with transverse laminations for a wide-speed-range synchronous reluctance traction motor. *IEEE Transactions on Industry Applications*, 51(6):4404–4414, 2015.

[5] Aníbal T. de Almeida, Fernando J. T. E. Ferreira, and Ge Baoming. Beyond induction motors — technology trends to move up efficiency. In *49th IEEE/IAS Industrial Commercial Power Systems Technical Conference*, pages 1–13, 2013.

[6] Mansour Ojaghi, Mahdi Sabouri, and Jawad Faiz. Performance analysis of squirrel-cage induction motors under broken rotor bar and stator inter-turn fault conditions using analytical modeling. *IEEE Transactions on Magnetics*, 54(11):1–5, 2018.

[7] Bilal Asad, Toomas Vaimann, Anton Rassõlkin, Ants Kallaste, and Anouar Belahcen. A survey of broken rotor bar fault diagnostic methods of induction motor. *Electrical, Control and Communication Engineering*, 14:117 – 124, 2018.

[8] Nicola Bianchi and Thomas M. Jahns. The rediscovery of synchronous reluctance and ferrite permanent magnet motors: Tutorial course notes. 2016.

[9] S. Morimoto, Y. Tong, Y. Takeda, and T. Hirasa. Loss minimization control of permanent magnet synchronous motor drives. *IEEE Transactions on Industrial Electronics*, 41(5):511–517, 1994.

[10] Gubae Rang, Jaesang Lim, Kwanghee Nam, Hyung-Bin Ihm, and Ho-Gi Kim. A mtpa control scheme for an ipm synchronous motor considering magnet flux variation caused

by temperature. In *Nineteenth Annual IEEE Applied Power Electronics Conference and Exposition, 2004. APEC '04.*, volume 3, pages 1617–1621 Vol.3, 2004.

[11] M.N. Uddin, T.S. Radwan, and M.A. Rahman. Performance of interior permanent magnet motor drive over wide speed range. *IEEE Transactions on Energy Conversion*, 17(1):79–84, 2002.

[12] Ching-Tsai Pan and S.-M. Sue. A linear maximum torque per ampere control for ipmsm drives over full-speed range. *IEEE Transactions on Energy Conversion*, 20(2):359–366, 2005.

[13] A.H. Wijenayake and P.B. Schmidt. Modeling and analysis of permanent magnet synchronous motor by taking saturation and core loss into account. In *Proceedings of Second International Conference on Power Electronics and Drive Systems*, volume 2, pages 530–534 vol.2, 1997.

[14] A. Consoli, G. Scarcella, G. Scelba, and S. Sindoni. Modeling control of ipm synchronous motors. In *2008 IEEE Power and Energy Society General Meeting - Conversion and Delivery of Electrical Energy in the 21st Century*, pages 1–6, 2008.

[15] Sung-Yoon Jung, Jinseok Hong, and Kwanghee Nam. Current minimizing torque control of the ipmsm using ferrari's method. *IEEE Transactions on Power Electronics*, 28(12):5603–5617, 2013.

[16] Alfio Consoli, Giuseppe Scarcella, Giacomo Scelba, and Antonio Testa. Steady-state and transient operation of ipmsms under maximum-torque-per-ampere control. *IEEE Transactions on Industry Applications*, 46(1):121–129, 2010.

[17] Anton Dianov, Fabio Tinazzi, Sandro Calligaro, and Silverio Bolognani. Review and classification of mtpa control algorithms for synchronous motors. *IEEE Transactions on Power Electronics*, 37(4):3990–4007, 2022.

[18] Anton Dianov, Kim Young-Kwan, Lee Sang-Joon, and Lee Sang-Taek. Robust self-tuning mtpa algorithm for ipmsm drives. In *2008 34th Annual Conference of IEEE Industrial Electronics*, pages 1355–1360, 2008.

[19] Adeeb Ahmed, Yilmaz Sozer, and Marv Hamdan. Maximum torque per ampere control for interior permanent magnet motors using dc link power measurement. In *2014 IEEE Applied Power Electronics Conference and Exposition - APEC 2014*, pages 826–832, 2014.

[20] Y. Tan, W.H. Moase, C. Manzie, D. Nešić, and I.M.Y. Mareels. Extremum seeking from 1922 to 2010. In *Proceedings of the 29th Chinese Control Conference*, pages 14–26, 2010.

[21] Silverio Bolognani, Roberto Petrella, Antonio Prearo, and Luca Sgarbossa. Automatic tracking of mtpa trajectory in ipm motor drives based on ac current injection. *IEEE Transactions on Industry Applications*, 47(1):105–114, 2011.

[22] Sungmin Kim, Young-Doo Yoon, Seung-Ki Sul, and Kozo Ide. Maximum torque per ampere (mtpa) control of an ipm machine based on signal injection considering inductance saturation. *IEEE Transactions on Power Electronics*, 28(1):488–497, 2013.

[23] Silverio Bolognani, Roberto Petrella, Antonio Prearo, and Luca Sgarbossa. On-line tracking of the mtpa trajectory in ipm motors via active power measurement. In *The XIX International Conference on Electrical Machines - ICEM 2010*, pages 1–7, 2010.

[24] Riccardo Antonello, Matteo Carraro, and Mauro Zigliotto. Theory and implementation of a mtpa tracking controller for anisotropic pm motor drives. In *IECON 2012 - 38th Annual Conference on IEEE Industrial Electronics Society*, pages 2061–2066, 2012.

[25] Riccardo Antonello, Matteo Carraro, and Mauro Zigliotto. Maximum-torque-per-ampere operation of anisotropic synchronous permanent-magnet motors based on extremum seeking control. *IEEE Transactions on Industrial Electronics*, 61(9):5086–5093, 2014.

[26] Silverio Bolognani, Luca Peretti, and Mauro Zigliotto. Online mtpa control strategy for dtc synchronous-reluctance-motor drives. *IEEE Transactions on Power Electronics*, 26(1):20–28, 2011.

[27] Nicola Bedetti, Sandro Calligaro, Christian Olsen, and Roberto Petrella. Automatic mtpa tracking in ipmsm drives: Loop dynamics, design, and auto-tuning. *IEEE Transactions on Industry Applications*, 53(5):4547–4558, 2017.

[28] Tianfu Sun, Jiabin Wang, and Xiao Chen. Maximum torque per ampere (mtpa) control for interior permanent magnet synchronous machine drives based on virtual signal injection. *IEEE Transactions on Power Electronics*, 30(9):5036–5045, 2015.

[29] Tianfu Sun, Jiabin Wang, and Mikail Koc. On accuracy of virtual signal injection based mtpa operation of interior permanent magnet synchronous machine drives. *IEEE Transactions on Power Electronics*, 32(9):7405–7408, 2017.

[30] Yue Zhao. Virtual square-wave current injection based maximum torque per ampere control for interior permanent-magnet synchronous machines. In *2016 IEEE Transportation Electrification Conference and Expo (ITEC)*, pages 1–6, 2016.

[31] R.F. Schiferl and T.A. Lipo. Power capability of salient pole permanent magnet synchronous motors in variable speed drive applications. *IEEE Transactions on Industry Applications*, 26(1):115–123, 1990.

[32] W.L. Soong and T.J.E. Miller. Practical field-weakening performance of the five classes of brushless synchronous ac motor drive. In *1993 Fifth European Conference on Power Electronics and Applications*, pages 303–310 vol.5, 1993.

[33] K. D. Hoang, J. Wang, M. Cyriacks, A. Melkonyan, and K. Kriegel. Feed-forward torque control of interior permanent magnet brushless ac drive for traction applications. In *2013 International Electric Machines Drives Conference*, pages 152–159, 2013.

[34] Bing Cheng and Tod R. Tesch. Torque feedforward control technique for permanent magnet synchronous motors. In *IECON 2007 - 33rd Annual Conference of the IEEE Industrial Electronics Society*, pages 1055–1060, 2007.

[35] Tae-Suk Kwon, Gi-Young Choi, Mu-Shin Kwak, and Seung-Ki Sul. Novel flux-weakening control of an ipmsm for quasi-six-step operation. *IEEE Transactions on Industry Applications*, 44(6):1722–1731, 2008.

[36] S. Morimoto, Y. Takeda, and T. Hirasa. Current phase control methods for permanent magnet synchronous motors. *IEEE Transactions on Power Electronics*, 5(2):133–139, 1990.

[37] A.K. Adnanes and T.M. Undeland. Optimum torque performance in pmsm drives above rated speed. In *Conference Record of the 1991 IEEE Industry Applications Society Annual Meeting*, pages 169–175 vol.1, 1991.

[38] Marco Tursini, Enzo Chiricozzi, and Roberto Petrella. Feedforward flux-weakening control of surface-mounted permanent-magnet synchronous motors accounting for resistive voltage drop. *IEEE Transactions on Industrial Electronics*, 57(1):440–448, 2010.

[39] Y.S. Chen, Z.Q. Zhu, and D. Howe. Influence of inaccuracies in machine parameters on field-weakening performance of pm brushless ac drives. In *IEEE International Electric Machines and Drives Conference. IEMDC'99. Proceedings (Cat. No.99EX272)*, pages 691–693, 1999.

[40] Wenqing Huang, Youtong Zhang, Xingchun Zhang, and Guan Sun. Accurate torque control of interior permanent magnet synchronous machine. *IEEE Transactions on Energy Conversion*, 29(1):29–37, 2014.

[41] Junggi Lee, Kwanghee Nam, Seoho Choi, and Soonwoo Kwon. Loss minimizing control of pmsm with the use of polynomial approximations. In *2008 IEEE Industry Applications Society Annual Meeting*, pages 1–9, 2008.

[42] Hisham Eldeeb, Christoph M. Hackl, Lorenz Horlbeck, and Julian Kullick. A unified theory for optimal feedforward torque control of anisotropic synchronous machines. *International Journal of Control*, 91(10):2273–2302, 2018.

[43] Y. Jeong, S. Sul, S. Hiti, and K.M. Rahman. Online minimum-copper-loss control of an interior permanent-magnet synchronous machine for automotive applications. *IEEE Transactions on Industry Applications*, 42(5):1222–1229, 2006.

[44] Hyeon-Sik Kim, Younggi Lee, Seung-Ki Sul, Jayeong Yu, and Jaeyoon Oh. Online mtpa control of ipmsm based on robust numerical optimization technique. *IEEE Transactions on Industry Applications*, 55(4):3736–3746, 2019.

[45] Faa-Jeng Lin, Ying-Chih Hung, Jia-Ming Chen, and Chao-Ming Yeh. Sensorless ipmsm drive system using saliency back-emf-based intelligent torque observer with mtpa control. *IEEE Transactions on Industrial Informatics*, 10(2):1226–1241, 2014.

[46] Ludovico Ortombina, Fabio Tinazzi, and Mauro Zigliotto. Magnetic modeling of synchronous reluctance and internal permanent magnet motors using radial basis function networks. *IEEE Transactions on Industrial Electronics*, 65(2):1140–1148, 2018.

[47] Bing Cheng and Tod R. Tesch. Torque feedforward control technique for permanent-magnet synchronous motors. *IEEE Transactions on Industrial Electronics*, 57(3):969–974, 2010.

[48] Gwangmin Park, Gyeongil Kim, and Bon-Gwan Gu. Sensorless pmsm drive inductance estimation based on a data-driven approach. *Electronics*, 10(7), 2021.

[49] A.R. Munoz and T.A. Lipo. On-line dead-time compensation technique for open-loop pwm-vsi drives. *IEEE Transactions on Power Electronics*, 14(4):683–689, 1999.

[50] I.R. Bojoi, E. Armando, G. Pellegrino, and S.G. Rosu. Self-commissioning of inverter nonlinear effects in ac drives. In *2012 IEEE International Energy Conference and Exhibition (ENERGYCON)*, pages 213–218, 2012.

[51] Yongsoon Park and Seung-Ki Sul. A novel method utilizing trapezoidal voltage to compensate for inverter nonlinearity. *IEEE Transactions on Power Electronics*, 27(12):4837–4846, 2012.

[52] Joon-Hee Lee and Seung-Ki Sul. Inverter nonlinearity compensation of discontinuous pwm considering voltage drop of power semiconductor and dead time effect. In *2020 IEEE Energy Conversion Congress and Exposition (ECCE)*, pages 5677–5682, 2020.

[53] Chan-Hee Choi, Kyung-Rae Cho, and Jul-Ki Seok. Inverter nonlinearity compensation in the presence of current measurement errors and switching device parameter uncertainties. *IEEE Transactions on Power Electronics*, 22(2):576–583, 2007.

[54] Gianmario Pellegrino, Radu Iustin Bojoi, Paolo Guglielmi, and Francesco Cupertino. Accurate inverter error compensation and related self-commissioning scheme in sensorless induction motor drives. *IEEE Transactions on Industry Applications*, 46(5):1970–1978, 2010.

[55] Yaodong Yang, Yu Tang, and Yongjian Li. Dead-time elimination method of high frequency inverter with shepwm. In *2019 14th IEEE Conference on Industrial Electronics and Applications (ICIEA)*, pages 457–461, 2019.

[56] H. Alawieh, K. Arab Tehrani, Y. Azzouz, and B. Dakyo. A novel dead time elimination strategy with zero crossing enhancement for voltage inverters. In *7th IET International Conference on Power Electronics, Machines and Drives (PEMD 2014)*, pages 1–5, 2014.

[57] Nicola Bedetti, Sandro Calligaro, and Roberto Petrella. Self-commissioning of inverter dead-time compensation by multiple linear regression based on a physical model. In *2014 IEEE Energy Conversion Congress and Exposition (ECCE)*, pages 242–249, 2014.

[58] Xiao Chen, Jiabin Wang, Bhaskar Sen, Panagiotis Lazari, and Tianfu Sun. A high-fidelity and computationally efficient model for interior permanent-magnet machines considering the magnetic saturation, spatial harmonics, and iron loss effect. *IEEE Transactions on Industrial Electronics*, 62(7):4044–4055, 2015.

[59] A. Vagati, G. Pellegrino, and P. Guglielmi. Comparison between spm and ipm motor drives for ev application. *The XIX International Conference on Electrical Machines - ICEM 2010*, pages 1–6, 2010.

[60] L. Tang, L. Zhong, M.F. Rahman, and Y. Hu. A novel direct torque control scheme for interior permanent magnet synchronous machine drive system with low ripple in torque and flux, and fixed switching frequency. In *2002 IEEE 33rd Annual IEEE Power Electronics Specialists Conference. Proceedings (Cat. No.02CH37289)*, volume 2, pages 529–534 vol.2, 2002.

[61] Yuan Ren, Z.Q. Zhu, James E. Green, Yun Li, Shiwu Zhu, and Zijian Li. Duty-ratio-based direct torque control for dual three-phase permanent magnet synchronous machine drives. In *2018 IEEE Energy Conversion Congress and Exposition (ECCE)*, pages 3367–3374, 2018.

[62] Zhuang Xu and M. F. Rahman. Comparison of a sliding observer and a kalman filter for direct-torque-controlled ipm synchronous motor drives. *IEEE Transactions on Industrial Electronics*, 59(11):4179–4188, 2012.

[63] Yuan Ren and Z. Q. Zhu. Enhancement of steady-state performance in direct-torque-controlled dual three-phase permanent-magnet synchronous machine drives with modified switching table. *IEEE Transactions on Industrial Electronics*, 62(6):3338–3350, 2015.

[64] Changliang Xia, Jiaxin Zhao, Yan Yan, and Tingna Shi. A novel direct torque control of matrix converter-fed pmsm drives using duty cycle control for torque ripple reduction. *IEEE Transactions on Industrial Electronics*, 61(6):2700–2713, 2014.

[65] Gianmario Pellegrino, Eric Armando, and Paolo Guglielmi. Direct flux field-oriented control of ipm drives with variable dc link in the field-weakening region. *IEEE Transactions on Industry Applications*, 45(5):1619–1627, 2009.

[66] Gianmario Pellegrino, Eric Armando, and Paolo Guglielmi. Direct-flux vector control of ipm motor drives in the maximum torque per voltage speed range. *IEEE Transactions on Industrial Electronics*, 59(10):3780–3788, 2012.

[67] Gianmario Pellegrino, Radu Iustin Bojoi, and Paolo Guglielmi. Unified direct-flux vector control for ac motor drives. *IEEE Transactions on Industry Applications*, 47(5):2093–2102, 2011.

[68] C. Cavallaro, A.O. Di Tommaso, R. Miceli, A. Raciti, G.R. Galluzzo, and M. Trapanese. Efficiency enhancement of permanent-magnet synchronous motor drives by online loss minimization approaches. *IEEE Transactions on Industrial Electronics*, 52(4):1153–1160, 2005.

[69] Mohammad Nasir Uddin, Md. Mizanur Rahman, Bhavinkumar Patel, and Bala Venkatesh. Performance of a loss model based nonlinear controller for ipmsm drive incorporating parameter uncertainties. *IEEE Transactions on Power Electronics*, 34(6):5684–5696, 2019.

[70] N. Bianchi and S. Bolognani. Magnetic models of saturated interior permanent magnet motors based on finite element analysis. In *Conference Record of 1998 IEEE Industry Applications Conference. Thirty-Third IAS Annual Meeting (Cat. No.98CH36242)*, volume 1, pages 27–34 vol.1, 1998.

[71] Sven Ludwig Kellner and Bernhard Piepenbreier. General pmsm d,q-model using optimized interpolated absolute and differential inductance surfaces. In *2011 IEEE International Electric Machines and Drives Conference (IEMDC)*, pages 212–217, 2011.

[72] Jinhai Liu and Wei Chen. Generalized dq model of the permanent magnet synchronous motor based on extended park transformation. In *2013 1st International Future Energy Electronics Conference (IFEEC)*, pages 885–890, 2013.

[73] S. A. Odhano, R. Bojoi, M. Popescu, and A. Tenconi. Parameter identification and self-commissioning of ac permanent magnet machines - a review. In *2015 IEEE Workshop on Electrical Machines Design, Control and Diagnosis (WEMDCD)*, pages 195–203, 2015.

[74] D. W. Novotny and T. A. Lipo. *Vector Control and Dynamics of AC Drives*. Oxford, Clarendon Press, 1996.

[75] Sandro CALLIGARO, Davide MARZONA, Roberto PETRELLA, and Amir SHAHDADI. Mtpa tracking algorithms for ipmsms and synrms: Accurate evaluation and

adaptive tuning of real signal injection and virtual signal injection. In *2020 IEEE Energy Conversion Congress and Exposition (ECCE)*, pages 6079–6086, 2020.

[76] Kwang-Woon Lee and Sang Bin Lee. Mtpa operating point tracking control scheme for vector controlled pmsm drives. In *SPEEDAM 2010*, pages 24–28, 2010.

[77] Massimiliano Biason, Sandro Calligaro, Mattia Iurich, Roberto Petrella, and Amir Shahdadi. Advances on analysis, modeling and accurate self-commissioning compensation of inverter dead-time distortion based on a physical model. In *2021 IEEE Energy Conversion Congress and Exposition (ECCE)*, pages 4788–4795, 2021.

[78] Krzysztof Jakub Szwarc, Artur Cichowski, Janusz Nieznanski, and Pawel Szczepankowski. Modeling the effect of parasitic capacitances on the dead-time distortion in multilevel npc inverters. In *2011 IEEE International Symposium on Industrial Electronics*, pages 1869–1874, 2011.

[79] N. Urasaki, T. Senjyu, T. Funabashi, and H. Sekine. Adaptive dead-time compensation strategy taking parasitic capacitance effects into account. In *2005 IEEE International Conference on Industrial Technology*, pages 1109–1114, 2005.

[80] Zhendong Zhang and Longya Xu. Dead-time compensation of inverters considering snubber and parasitic capacitance. *IEEE Transactions on Power Electronics*, 29(6):3179–3187, 2014.

[81] J.M. Guerrero, M. Leetmaa, F. Briz, A. Zamarron, and R.D. Lorenz. Inverter nonlinearity effects in high-frequency signal-injection-based sensorless control methods. *IEEE Transactions on Industry Applications*, 41(2):618–626, 2005.

Acknowledgements

Countless people supported my effort on this thesis, but I would like to express my deepest gratitude to my advisor, Prof. Roberto Petrella whose support and encouragement I will never forget. I am proud of, and grateful for, my time working with Prof. Petrella. Also this thesis would not have been possible without Prof. Sandro Calligaro, whose guidance from the very outset enabled me to develop an understanding of the subject. I especially want to thank Prof. Michele Degano for his compassionate support and encouragement in the development of newly designed motors in Nottingham University.

I want to thank my colleagues at the University of Udine, especially Dr. Riccardo Breda, Dr. Mattia Iurich, Dr. Massimiliano Biason and Dr. Giacomo Andrioli, who supported me in both my personal and professional life. I am grateful for my family whose constant love and support keep me motivated and confident, especially my father Dad-Rahman Shahdadi, Dr. Abdulvahed, Mir Muhammad, Molana Abdulhamid, Muhammad-Yaqub and Muhammad-seddiq, Maryam, Shah bibi, Iran-malek and Zahra. My accomplishments and success are because they believed in me. Deepest thanks to my mom, Fereshteh, Zia, Mirsaeed, Shahin and Nazanin, who keep me grounded, remind me of what is important in life, and are always supportive of my adventures. Thank you all for the strength you gave me.

Amir Shahdadi, Udine, October 2022